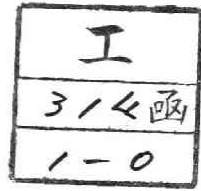


Title	Transport Phenomena in Pulsating Pipe Flow(Dissertation_全文)
Author(s)	Maruyama, Toshiro
Citation	Kyoto University (京都大学)
Issue Date	1975-05-23
URL	http://dx.doi.org/10.14989/doctor.r2795
Right	
Type	Thesis or Dissertation
Textversion	author

TRANSPORT PHENOMENA IN
PULSATING PIPE FLOW

T. MARUYAMA



TRANSPORT PHENOMENA IN PULSATING PIPE FLOW

TOSHIRO MARUYAMA

*Department of Chemical Engineering
Kyoto University*

November 1974

CONTENTS

Chapter 1	INTRODUCTION	<i>page</i>	1
1.1	Pulsating Pipe Flow		1
1.2	Heat or Mass Transfer in Pulsating Flow		2
1.3	Dynamic Process of Bursting.		3
1.4	Purpose and Outline of This Study.		5
1.5	Fluid Mechanical Apparatus		6
Chapter 2	FREQUENCY RESPONSE OF MOMENTUM TRANSFER		9
2.1	Introduction		9
2.2	Test Section and Measuring Equipment		9
2.3	Results and Discussion		10
2.3.1	Experimental curve in pulsating flow		12
2.3.2	Frequency response for laminar flow		12
2.3.3	Frequency response for turbulent flow		12
2.4	Conclusion		20
Chapter 3	FREQUENCY RESPONSE OF HEAT OR MASS TRANSFER.		22
3.1	Introduction		22
3.2	Analysis		22
3.2.1	Solution for steady flow		24
3.2.2	Solution for pulsating flow.		25
3.3	Test Section and Measuring Equipment		29

3.4	Results and Discussion	page 33
3.4.1	Transfer coefficient in steady flow	33
3.4.2	Experimental curve of transfer coefficient in pulsating flow . .	33
3.4.3	Frequency response of local Nusselt number	35
3.4.4	Frequency response of space-averaged Sherwood number.	40
3.4.5	Resonance point.	40
3.4.6	Effect of flow pulsation on time- averaged transfer rate.	43
3.5	Conclusion	46
Chapter 4	DYNAMIC BEHAVIOUR OF PULSATING TURBULENT FLOW.	47
4.1	Introduction	47
4.2	Test Section and Measuring Equipment .	48
4.3	Results and Discussion	50
4.3.1	Profiles in steady flow.	50
4.3.2	Velocities in pulsating flow . . .	53
4.3.3	Profiles I ($T > T_c$).	55
4.3.4	Profiles II ($T < T_c$)	62
4.3.5	Time between bursts in steady flow T_B	68
4.3.6	Time between bursts in pulsating flow $\overline{T_{Bp}}$	74
4.3.7	Classification of pulsating turbulent flow	78
4.4	Conclusion	83

Chapter 5	DYNAMIC PROCESS OF BURSTING IN PULSATING TURBULENT FLOW	<i>page</i> 84
5.1	Introduction	84
5.2	Test Section and Measuring Equipment .	85
5.3	Results and Discussion	85
5.3.1	Region of burst period in steady flow	85
5.3.2	Resonant pulsating flow.	86
5.3.3	Phase-averaged correlation coefficient.	93
5.3.4	Propagation of generated turbulence	94
5.3.5	Mean propagation time.	103
5.3.6	Mean burst period.	106
5.4	Conclusion	108
Chapter 6	CONCLUSION	109
6.1	Frequency Response of Momentum, Heat and Mass Transfer.	109
6.2	Resonance Phenomena in Pulsating Flow	109
6.3	Dynamic Process of Bursting.	110
6.4	Recommendation of Future Work.	111
NOMENCLATURE.		112
REFERENCES.		116

ERRATA

(B) : from bottom, (T) : from top

Page	Line	erroneous	should read
1	3(T)	Pusating	Pulsating
3	3(T)	problen	problem
3	11(B)	artificially	artificially
4	2(B)	respect -ively	respec- tively
12	15(B)	thses	these
22	10(B)	reponses	responses
22	8(B)	charified	clarified
25	7(T)	conditons	conditions
31	12(T)	100-V.	110-V.
40	10(B)	multiple	multiple
43	11(T)	postion	position
44	9(T)	fo	of
48	12(T)	appart	apart
53	4(T)	comporent	component
69	10(T)	obtained	obtain
78	11(T)	reconance	resonance
111	2(B)	interpreted	interpreted

CHAPTER 1

INTRODUCTION

1.1 Pulsating Pipe Flow

Pulsating pipe flow appears in several practical situations, for example, when fluid is pumped through a channel by a reciprocating device, or when flow instabilities are present that give rise to oscillatory motions.

The situation that is chosen for this study is a general case of a fully developed flow in a cylindrical tube with a periodical pulsation under the condition that the pulsating component of flow rate is kept less than the time-averaged value.

Pulsating laminar flow was studied analytically by Sexl [19] and the frequency response curves were shown by Uchida [23].

For the pulsating turbulent flow, however, there have been only a few experimental studies, because it is very difficult to study a turbulence structure that varies during the cycle of pulsation. Qualitatively, some features have been shown. Schulz-Grunow [18] indicated that velocity profiles for pulsating turbulent flow were similar to the profiles for steady flow through a gradually convergent or divergent pipe. Recently, Gerrard [5] suggested that the turbulence intensity diminished during acceleration, and that in decelerating flow the turbulence intensity increased.

1.2 Heat or Mass Transfer in Pulsating laminar flow

Interphase heat or mass transfer in pulsating flow is of interest in many areas of application including chemical reactor design, studies on the fluctuation in velocity gradient at a wall using heat transfer probes or mass transfer probes, and studies on transport in the cardiovascular system.

There have been a number of experimental investigations [20, 24] concerning only the effect of pulsation in flow rate on the time-averaged rate of heat or mass transfer. However, these results are in conflict with each other.

An analytical approach to the problem was first made by Siegel and Perlmutter [21]. Using characteristic method they obtained a solution for heat transfer of pulsating slug flow between parallel plates, and clarified that the time-averaged heat-transfer rate was not appreciably changed by the pulsation. Simultaneously, they pointed out that a node in wall temperature or heat flux variation might exist. A further elaborated numerical calculation was made by Mochizuki and Hatta [13] by including the effect of the transverse velocity distribution.

Recently, from the viewpoint of dynamic response, some analytical approaches to frequency response of transfer coefficient to wall shear stress were made. Alabastro and Hellums [1] made a calculation by straightforward numerical integration and, for the cases of very high and low frequency by a perturbation method similar to that used by Lighthill [11]. Lebouché [9] also used

a perturbation method, but his results comprised a similarity relation which is used in analysis of the steady-state problem. Since his results represented only the low-frequency region, the validity of the similarity relation is not clear. In the results of both Alabastro *et al.* and Lebouché the node did not appear.

On the other hand, no experimental approach to the frequency response of transfer coefficient has been made, because of the difficulty of experimental technique.

1.3 Dynamic Process of Bursting

There has been found no literature in which the turbulence structure has been studied in pulsating flow.

For steady turbulent flow, the importance of the wall region in the transport phenomena and the generation and maintenance of turbulence is well known. Recently, visual studies have shed new light on the study of the turbulence structure of the wall region.

Applying a combined dye-injection and hydrogen-bubble technique to an artificially tripped turbulent boundary layer, Kline *et al.* [8] observed that the wall area ($0 < y^+ < 100$) showed a distinct pattern characterized by a deterministic sequence of events occurring randomly in both space and time. They described the sequence as being composed of three stages: (i) the appearance of a relatively low-speed region of fluid near the wall: (ii) the 'lift-up' of this 'low-speed streak' from the wall followed by some form of 'oscillatory growth' and (iii) ultimately, the 'breakup' of any signs of coherency in the visual representations of this struc-

ture. These entire three-stage process was called 'bursting'. From estimates made from the hydrogen-bubble data, they observed that practically all the turbulence production occurred during bursting. In addition they strongly suggested that the cycle was intermittent but had a definite preferred range of period of occurrence and a well-defined mean period, i.e. mean burst period.

Corino and Brodkey [3], using a dark-field illumination technique in successive strips of the flow, observed a deterministic sequence of events which is in essential agreement with those reported by Kline *et al.*. Corino and Brodkey suggested that an interaction between accelerated and retarded flow was fundamental to the lift-up process. The first event of this stage was the deceleration of the axial velocity characterized by the essential disappearance of the velocity gradient and by a velocity defect as great as 50 % of the local mean velocity. The second event was an acceleration; i.e. a mass of fluid coming from upstream and entering at a layer of $y^+ \approx 15$ was directed toward the wall and interacted with the fluid in the decelerated region. The third event was a lift-up.

Rao *et al.* [17] measured the burst period over the wide Reynolds number range using a hot-wire anemometry technique in a turbulent boundary layer. Their measurements indicated that the mean burst period scaled with the variables of the outer flow instead of the inner variables.

More recently, Nychas *et al.* [14] and Offen and Kline [15] using the same visual techniques as those used by Corino and Brodkey and by Kline *et al.* respectively, observed the outer region of turbulent boundary

layer and suggested that the transverse vortex was a part of the bursting process.

However, deterministic sequence of events related to the entire burst period has not been known yet.

1.4 Purpose and Outline of This Study

One objective of this study is to investigate the dynamic behaviour of momentum, heat and mass transfer from a view point of frequency response. Another objective is concerned with the dynamic behaviour of turbulence. Of special interest is an investigation of bursting phenomena in pulsating turbulent flow.

In Chapters 2 and 3, the frequency responses of momentum, heat and mass transfer are discussed.

Chapter 2 deals with the frequency response of momentum transfer. For pulsating laminar flow, Sexl's analysis [19] is verified experimentally. For pulsating turbulent flow, a contribution of Reynolds stress to the frequency response is discussed.

In Chapter 3, the frequency response of heat or mass transfer in pulsating laminar flow is studied. Detailed discussion is made about the discrepancy from the similarity relation under three heating conditions over the wide range of frequency, analytically and experimentally.

In Chapters 4 and 5, the dynamic behaviour of turbulence is discussed.

Chapter 4 deals with the dynamic behaviour of pulsating turbulent flow. The relation between the burst period and the pulsation period is clarified

through the measurements of the dynamic change of velocity and turbulence characteristics, by using a phase averaging technique and correlation functions.

In Chapter 5, dynamic process of bursting in resonant pulsating flow is discussed. The turbulence generation and propagation are examined by using a phase-averaged correlation function. Of interest is the relation between the burst period and the propagation time.

1.5 Fluid Mechanical Apparatus

The flowsheet of the pulsating tube-flow system is shown in Fig. 1.1. Liquid from the storage tank was pumped at a steady rate to a loop of P.V.C. tube (12 m long and 4.45 cm internal diameter) by a centrifugal pump made of stainless steel. The forerunning and test sections are single straight tube of 5 m long and three different inside diameters, i.e., 0.9, 2 and 5.16 cm.

Two bellows pumps, in which the fluids pulsate with a phase difference π to each other, were connected to the tube line at the inlet of the forerunning section and at the outlet of the test section, respectively; thus the pulsation was superimposed on a steady flow. The pulsation period could be altered within a range of 0.76 - 7.9 sec by means of a stepless variable speeder, and the amplitude of pulsation could be adjusted by varying the stroke of the pistons.

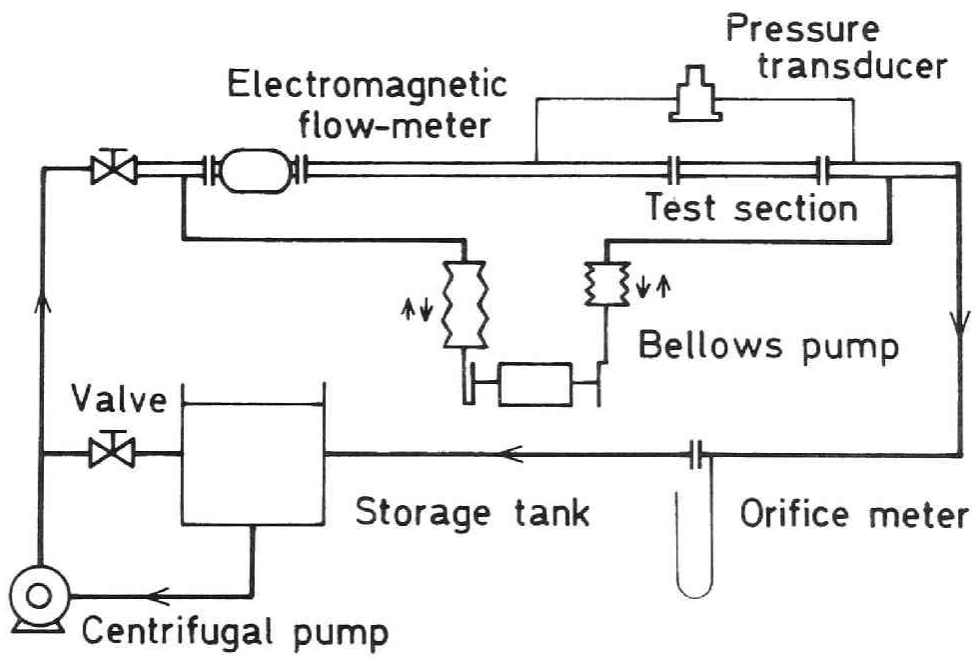


Fig. 1.1. Flow system.

CHAPTER 2

FREQUENCY RESPONSE OF MOMENTUM TRANSFER

2.1 Introduction

In this chapter, the frequency responses of flow rate and wall shear stress to pressure drop are studied experimentally. Discussions are made for both laminar and turbulent flows.

In pulsating turbulent flow in which the pulsation period is the same order as those of turbulence, it can be inferred that the structure of turbulence changes according to the flow pulsation; all the more so when the amplitude of pulsation is large enough to produce an appreciable effect on the generation of turbulent energy. Detailed discussions for the turbulence structure will be made in Chapters 4 and 5. The study in this chapter is restricted to the pulsating flow with the small amplitude; the amplitude of pressure drop is less than the time-averaged value.

First, frequency response curves for laminar flow were drawn experimentally and the results were compared with Sexl's analysis. Next, for turbulent flow an eddy viscosity contribution to the pulsating component was discussed by comparing experimental results with an analytical estimation based on the Prandtl's mixing-length theory.

2.2 Test Section and Measuring Equipment

For the test section, two pipes of different inside diameter (0.9 cm and 2 cm) were used.

At the inlet of these pipes, the flow rate was measured by an electromagnetic flowmeter (Yokogawa Model MFP-0.4). At the test section, the pressure drop between two points 200 cm apart was measured by a pressure transducer (Shinkoh Model DP 100) and the wall shear stress by the electrochemical method [12]. The test electrode consisted of a cathode of platinum film (length of mass transfer section $l = 0.002$ cm) and an anode of nickel pipe. Both surfaces of cathode and anode were carefully made flush to form a single tube. (see Fig. 3.4) From the mass transfer variation at the cathode, the variation of wall shear stress can be analytically calculated with high accuracy. The working fluids with their physical properties are listed in Table 2.1.

The electrical signals of wall shear stress and flow rate were amplified using a d.c. amplifier (Dana Model 3400) and then, each signal was recorded with that of pressure drop on a chart of photocorder (Yokogawa Model EMO-62).

The time constant of pressure transducer is negligible small (Ca. 0.002 sec), while those of electromagnetic flowmeter (0.1 sec) and wall shear stress meter (see Section 3.4.4) can not be neglected. Accordingly, corrections for the measurements of flow rate and wall shear stress were made by using the time constants.

2.3 Results and Discussion

Table 2.1. Test fluids

D [cm]	Re	test fluids and their physical properties
0.9	laminar flow $< 2 \times 10^3$	for flow rate { glycerol water 0 - 70 wt.% at 20 °C for wall shear stress { 2N KOH 0.01 mole $K_4Fe(CN)_6$ 0.01 mole $K_3Fe(CN)_6$ $\rho = 1.081$ [g/cm ³] $\mu = 0.01211$ [g/cm·sec] Sc = 1846 at 20 °C
	turbulent flow 5×10^3 1×10^4	{ 3N KOH 0.01 mole $K_4Fe(CN)_6$ 0.01 mole $K_3Fe(CN)_6$ $\rho = 1.132$ [g/cm ³] $\mu = 0.01404$ [g/cm·sec] Sc = 2390 at 20 °C
2	1×10^4 2×10^4 5×10^4 1×10^5	

2.3.1 Experimental curve in pulsating flow

One example of experimental curve are illustrated in Fig. 2.1. The three curves of pressure drop, wall shear stress and flow rate are nearly sinusoidal, and the latter two as output signals show apparent amplitude attenuations and phase shifts to that of pressure drop as input signal.

2.3.2 Frequency response for laminar flow

The amplitude ratio and phase lag of each output signal to the input signal were obtained from the first harmonics of the oscillating components. The harmonic analysis was made by using 20 values within one cycle.

Figures 2.2 and 2.3 show the experimental results of frequency response of wall shear stress and flow rate. In these figures the amplitude ratio is normalized by that for quasi-steady state ($\omega = 0$). They are correlated well on Stokes number Sn , i.e. nondimensional frequency, and agree well with Sexl's analysis shown by rigid lines. Comparison of two response curves shows that wall shear stress responses more quickly than flow rate at higher frequency.

2.3.3 Frequency response for turbulent flow

In turbulent flow, there exists large nonlinearity between flow rate and pressure drop. Therefore an assumption of linearity within a limited range around the steady value was made to use the same procedure as that for laminar flow.

From the experimental results, it was clarified that the attenuations and phase shifts of both wall shear

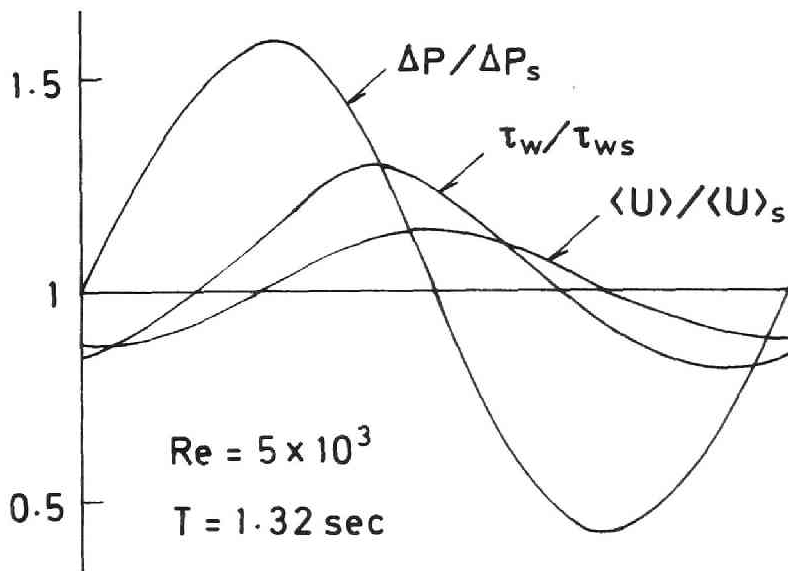


Fig. 2.1. Variations of pressure drop, wall shear stress and flow rate.

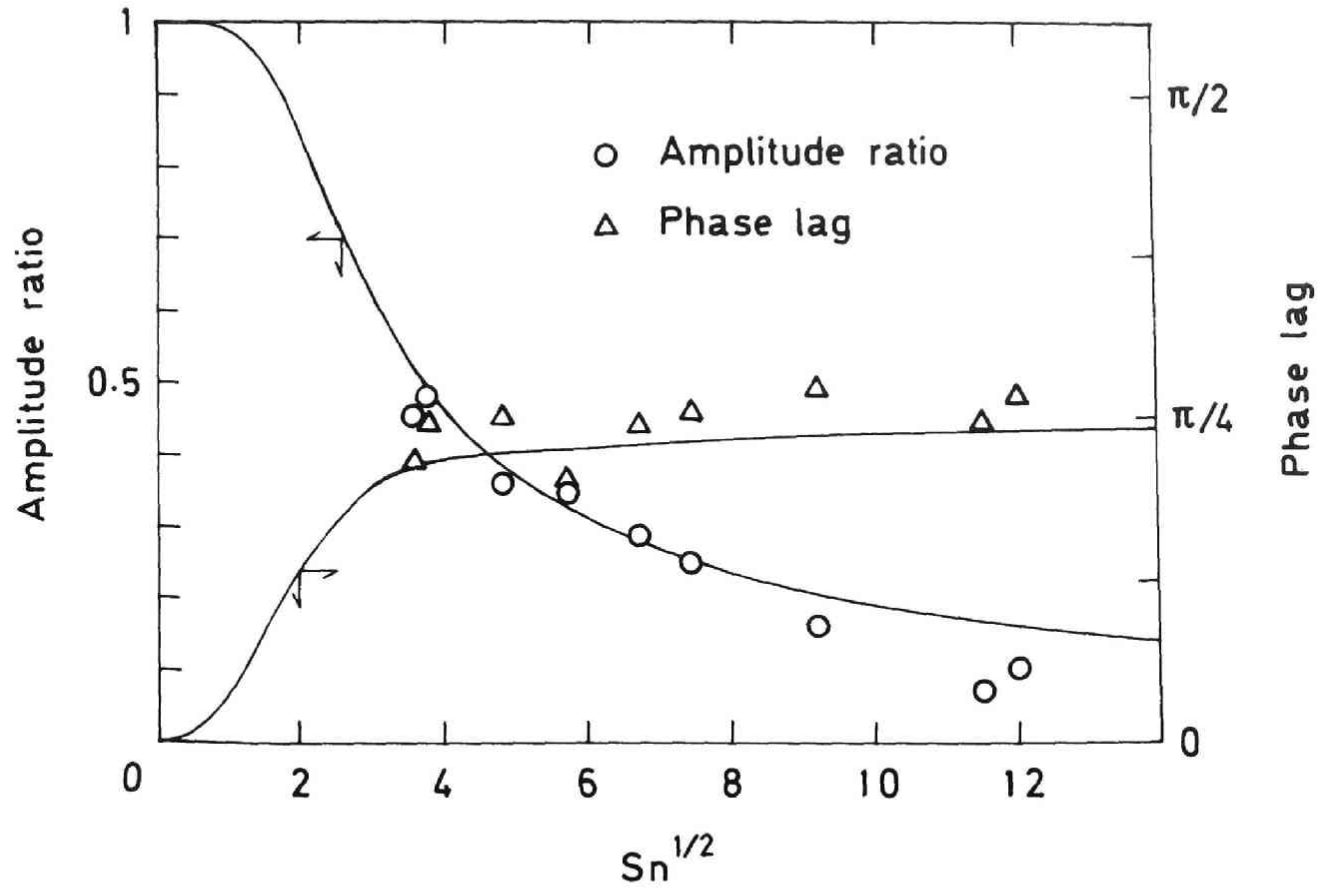


Fig. 2.2. Frequency response of wall shear stress for laminar flow.

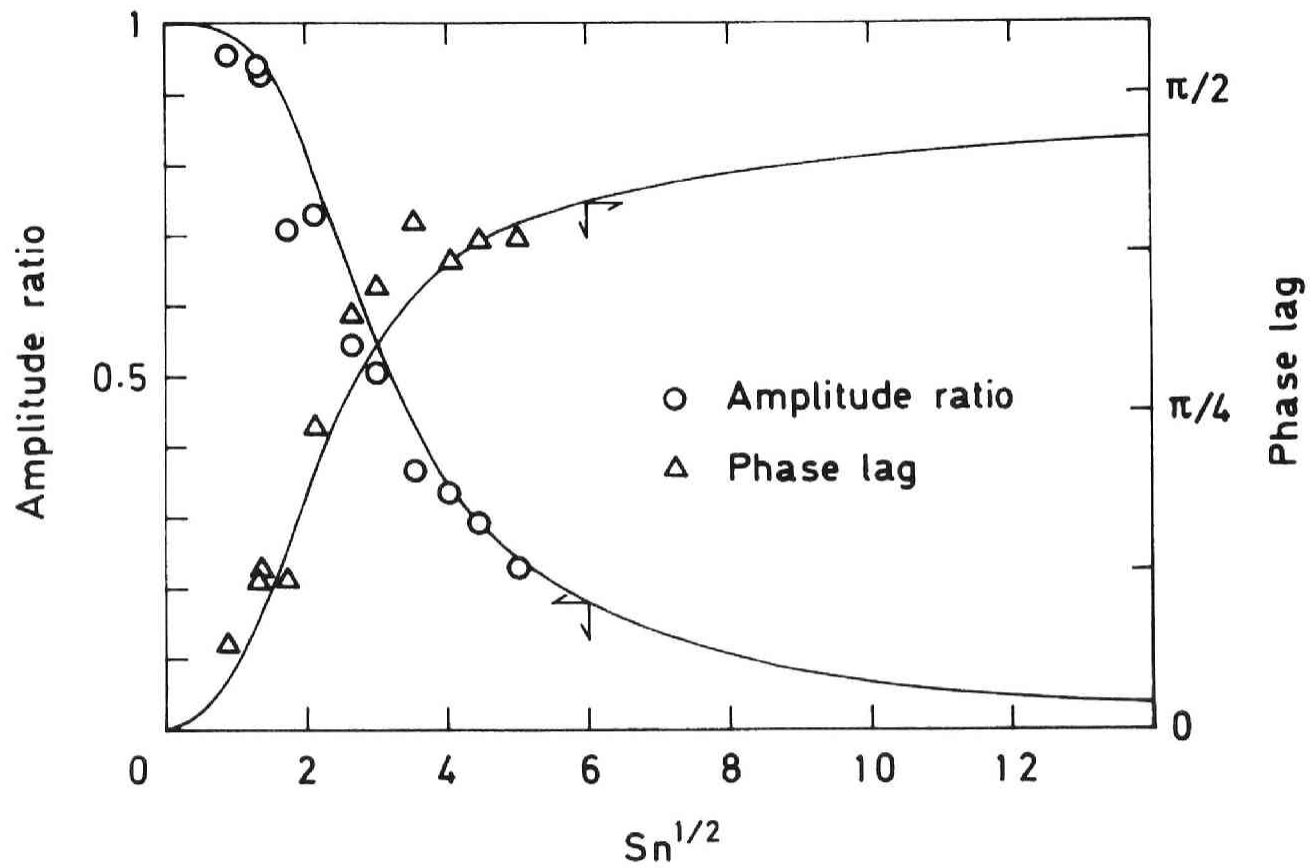


Fig. 2.3. Frequency response of flow rate for laminar flow.

stress and flow rate decreased as Reynolds number increased. This Reynolds number dependency is attributed to the unsteady-state Reynolds stress.

To correlate the results with a variable similar to Sn for laminar flow, a rough estimation was made. The momentum equation for this system takes the form:

$$\frac{\partial U}{\partial t} = -\frac{1}{\rho} \frac{\partial P}{\partial x} + \frac{\nu}{r} \frac{\partial}{\partial r} \left(r \frac{\partial U}{\partial r} \right) - \frac{1}{r} \frac{\partial}{\partial r} (r \overline{uv}) \quad (2.1)$$

For simplicity of calculation an eddy viscosity model based on the Prandtl's mixing-length theory is used as

$$-\rho \overline{uv} = \rho \epsilon \frac{\partial U}{\partial r} = -\rho \ell_m^2 \left(\frac{\partial U}{\partial r} \right)^2 \quad (2.2)$$

where ϵ is the eddy viscosity and ℓ_m is the mixing length.

Similar to the case of pulsating laminar flow, time-dependent variables were divided into steady components and pulsating components as follows.

$$-\frac{1}{\rho} \frac{\partial P}{\partial x} = \left(-\frac{1}{\rho} \frac{\partial P}{\partial x} \right)_s \{1 + a_p \exp(i\omega t)\} \quad (2.3)$$

$$U = U_s + U_p \exp(i\omega t) \quad (2.4)$$

where a_p is a real number but U_p can be a complex number. Substituting Eq. (2.4) into Eq. (2.2) and neglecting the second-order term, one finds the pulsating component of eddy viscosity to be twice of steady component.

$$-\rho \overline{uv}_p = 2\rho \epsilon \frac{\partial U_p}{\partial r} \exp(i\omega t) \quad (2.5)$$

substituting Eqs. (2.3)—(2.5) into Eq. (2.1) and subtracting the equation of steady component yield the expression for pulsating component as an ordinary differential equation with the parameter Sn

$$\frac{i Sn U}{1+2\epsilon_s/\nu} = -\frac{2}{1+2\epsilon_s/\nu} + \left\{ \frac{1}{R} + \frac{1}{1+2\epsilon_s/\nu} \frac{d(2\epsilon_s/\nu)}{dR} \right\} \\ \times \frac{dU}{dR} + \frac{d^2 U}{dR^2} \quad (2.6)$$

where $U = \frac{2U_p \nu}{a_p r_0^2 \left(-\frac{1}{\rho} \frac{\partial P}{\partial x} \right)_s}$ and $R = r/r_0$,

and boundary conditions are

$$\begin{aligned} U = 0 & \quad \text{at} \quad R = 1 \\ dU/dR = 0 & \quad \text{at} \quad R = 0 \end{aligned} \quad (2.7)$$

With an application of the principle of superposition, the numerical solutions of Eq. (2.6) for the experimental conditions were obtained by the Runge-Kutta-Gill method. The eddy viscosity in steady state are referred to those by von Kármán [7] for the wall region and that by Hinze [6] for the core region. First, an accuracy of numerical calculation was confirmed by comparing the calculation for laminar flow with Sexl's analysis. They were coincident within an accuracy of 0.1 %.

Figures 2.4 and 2.5 show both analytical and experimental results plotted against a combined variable $Sn/(1 + 2\epsilon_c/\nu)$, which is obtained from Eq. (2.6) by assuming that the eddy viscosity is constant and equal to that for the core region, i.e.

$$\epsilon_c/\nu = 0.07 R^+$$

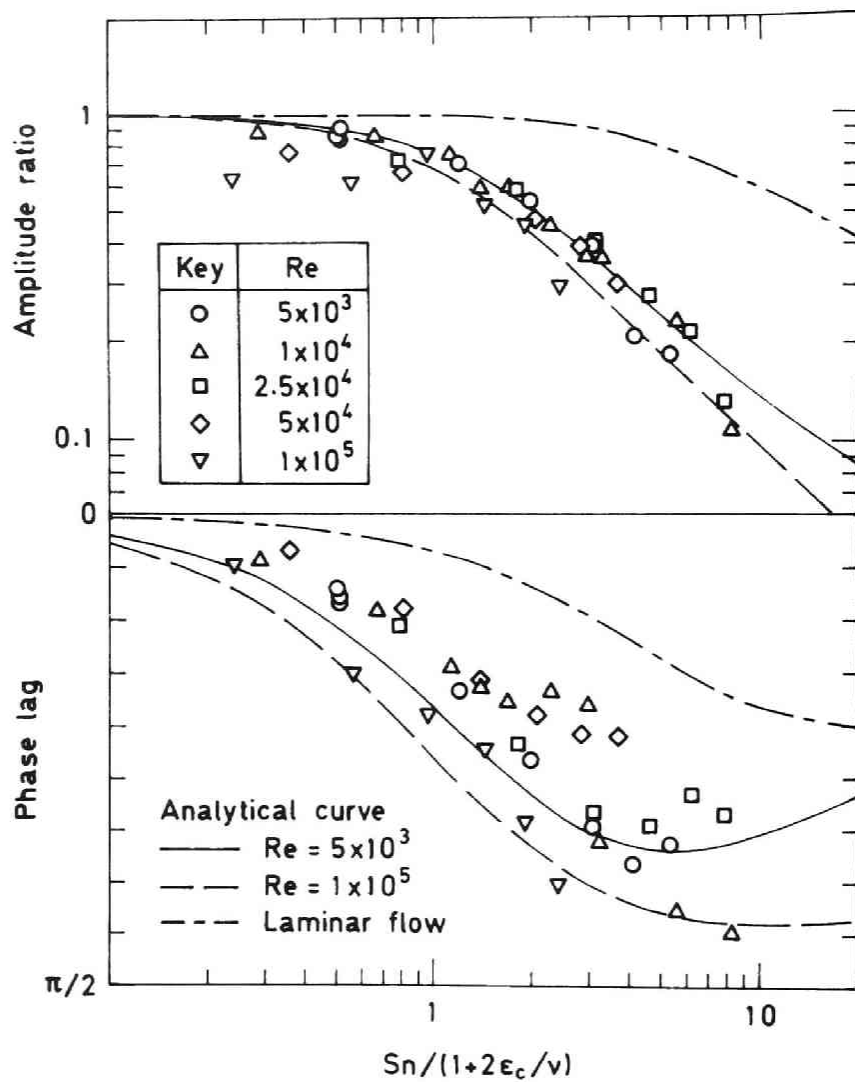


Fig. 2.4. Bode diagram of wall shear stress for turbulent flow.

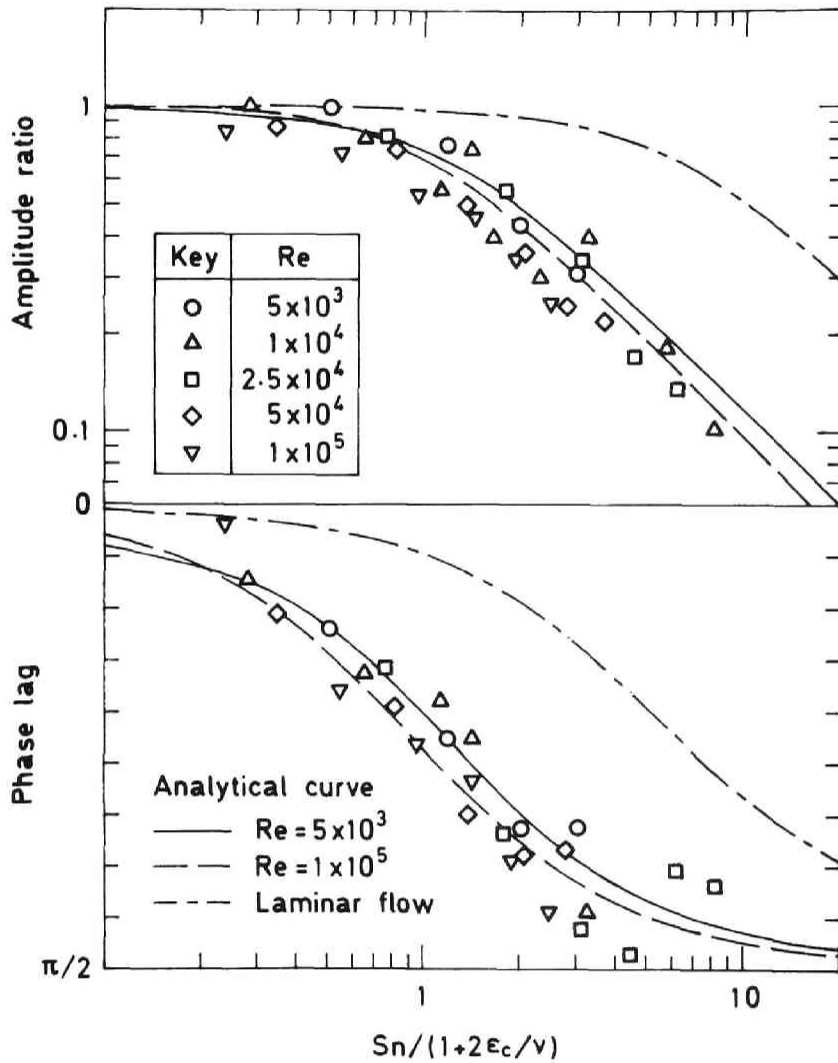


Fig. 2.5. Bode diagram of flow rate for turbulent flow.

In both figures, only two calculated curves for maximum and minimum values of Reynolds number of the experimental conditions, i.e. $Re = 5 \times 10^3$ and 10^5 , are indicated, as the other curves for $Re = 10^4$, 2.5×10^4 and 5×10^4 exist in the narrow zone between the two curves. Because of the radial distance dependency of an eddy viscosity, the calculated results are not universally represented by a single curve. However, the experimental results over the wide range of Reynolds number are well correlated with the combined variable $Sn/(1 + 2\varepsilon_c/\nu)$ within an experimental accuracy, and in good agreement with analytical curves. Thus, the contribution of Reynolds stress to the frequency response can be estimated by the eddy viscosity model similar to that for steady turbulent flow.

2.4 Conclusion

1. The frequency response of momentum transfer for laminar flow depends only on Stokes number, and measurements are well correlated with Sexl's analysis.
2. In turbulent flow, the amplitude attenuation and phase shift of wall shear stress and flow rate to pressure drop decreases as Reynolds number increases because of the unsteady-state Reynolds stress. This contribution of Reynolds stress to the frequency response is estimated by Prandtl's expression for eddy viscosity over the following ranges of parameters:

$$5 \times 10^3 < Re < 1 \times 10^5, \quad 10 < Sn < 800 \quad \text{and} \\ 0 < a_p < 1.0.$$

3. The eddy viscosity for the core region of the tube is main cause of the Reynolds number dependency of frequency response, so the modified parameter $Sn/(1 + 2\varepsilon_c/\nu)$ is useful for the rough estimation.

CHAPTER 3

FREQUENCY RESPONSE OF HEAT OR MASS TRANSFER

3.1 Introduction

In this chapter, the frequency response of heat or mass transfer in pulsating laminar flow is studied. The situation that is chosen for this study is the entrance-region heat transfer, because at fully developed region of heat transfer the transfer rate is independent of flow rate.

For the steady-state heat transfer at the entrance region of constant wall temperature, L  v  que [10] showed analytical results using the similarity variable. This similarity variable was applied to the other two heating conditions, i.e. constant wall heat flux and linearly varying wall temperature, by other investigators [2].

This section deals with the transfer under those three heating conditions. First, the frequency responses of transfer coefficients over the wide range of frequency were characterized analytically by using the similarity variable. Next, the results were compared with the exact numerical solutions and experimental results ; the validity of similarity relation and the existence of node were discussed. In the last part of this chapter, an effect of pulsating flow on the time-averaged transfer coefficient was discussed.

3.2 Analysis

Assuming that the similarity variable is applicable not only to steady flow but also to pulsating flow, the author made an analysis as follows.

The thickness of the temperature boundary layer is assumed to be thin enough so that the curvature of the tube wall is negligible and the velocity profile may be considered as a linear function of distance from the wall with a slope equal to the actual slope at the wall. Hence, unsteady energy equation can be written nondimensionally as

$$\frac{\partial \Gamma}{\partial \theta} + \frac{\tau_w(\theta)}{\tau_{ws}} Y \frac{\partial \Gamma}{\partial X} = \frac{\partial^2 \Gamma}{\partial Y^2} \quad (3.1)$$

where $\theta = \lambda t / C_p \rho r_0^2$, $Y = y/r_0$ and $X = x/DRePr$

Input and output signals can be divided into time-averaged and oscillating components as

$$\frac{\tau_w(\theta)}{\tau_{ws}} = 1 + a_\tau \exp(iSnPr\theta) \quad (3.2)$$

$$\Gamma = \Gamma_s(X, Y) + \Gamma_p(X, Y) \exp(iSnPr\theta) \quad (3.3)$$

where a_τ is a real number but Γ_p can be a complex number. Substituting Eqs. (3.2) and (3.3) into Eq. (3.1), neglecting second-order terms and comparing the terms of the same family, one obtains differential equations for the two components as

$$Y \frac{\partial \Gamma_s}{\partial X} = \frac{\partial^2 \Gamma_s}{\partial Y^2} \quad (3.4)$$

$$iSnPr\Gamma_p + a_\tau Y \frac{\partial \Gamma_s}{\partial X} + Y \frac{\partial \Gamma_p}{\partial X} = \frac{\partial^2 \Gamma_p}{\partial Y^2} \quad (3.5)$$

3.2.1 Solution for steady flow

Using the method of combination of variable, Lévêque [10] and Bird [2] obtained the solution of Eq. (3.4) in which similarity variable, Eq. (3.6) was used.

$$\eta = Y/(9X)^{1/3} \quad (3.6)$$

The three heating conditions are

[A] constant wall temperature.

[B] constant wall heat flux.

[C] linearly varying wall temperature.

The following dependent variable correspond to the above conditions, respectively.

$$F(\eta) = \begin{cases} (\Gamma' - \Gamma'_b)/(\Gamma'_w - \Gamma'_b) & (3.7) \\ \frac{\partial \Gamma'}{\partial Y} / \frac{\partial \Gamma'}{\partial Y} \Big|_{Y=0} & (3.8) \\ \frac{\partial}{\partial X} \left(\frac{\Gamma' - \Gamma'_b}{C} \right) & (3.9) \end{cases}$$

Then partial differential equation, Eq. (3.4) becomes ordinary differential equations.

For conditions [A] and [C],

$$\frac{d^2 F_S}{d\eta^2} + 3\eta^2 \frac{dF_S}{d\eta} = 0 \quad (3.10)$$

and for condition [B],

$$\eta \frac{d^2 F_S}{d\eta^2} + (3\eta^3 - 1) \frac{dF_S}{d\eta} = 0 \quad (3.11)$$

thus boundary conditions become equal in all three cases as

$$\begin{aligned}
 F_S &= 0 & \text{at } \eta &\rightarrow \infty \\
 F_S &= 1 & \text{at } \eta &= 0
 \end{aligned}
 \tag{3.12}$$

Accordingly, the solution of condition [C] is equal to the space-averaged value of the solution of condition [A]. As shown in Fig. 3.1 the Nusselt number as functions of X in steady laminar flow are similar for the three heating conditons.

3.2.2 Solution for pulsating flow

Now it is assumed that the similarity relation between X and Y which is valid in steady flow is preserved in pulsating flow. That is, the function F can also be applied to the oscillating components. Equation (3.5) becomes ordinary differential equations: for conditions [A] and [C]

$$\begin{aligned}
 \frac{d^2 F_P}{d \eta^2} + 3 \eta^2 \frac{d F_P}{d \eta} - 9^{2/3} i(\text{SnPr} X^{2/3}) F_P \\
 = \frac{9 a_\tau \eta^2}{\Gamma(1/3)} \exp(-\eta^3)
 \end{aligned}
 \tag{3.13}$$

and for condition [B]

$$\begin{aligned}
 \eta \frac{d^3 \bar{F}_P}{d \eta^3} + (3 \eta^3 - 1) \frac{d^2 \bar{F}_P}{d \eta^2} - 9^{2/3} i(\text{SnPr} X^{2/3}) \\
 \times \left(\eta \frac{d \bar{F}_P}{d \eta} - \bar{F}_P \right) = \frac{9 a_\tau \eta^4}{\Gamma(2/3)} \exp(-\eta^3)
 \end{aligned}
 \tag{3.14}$$

where

$$\bar{F}_P = \int_{\eta}^{\infty} F_P d\eta
 \tag{3.15}$$

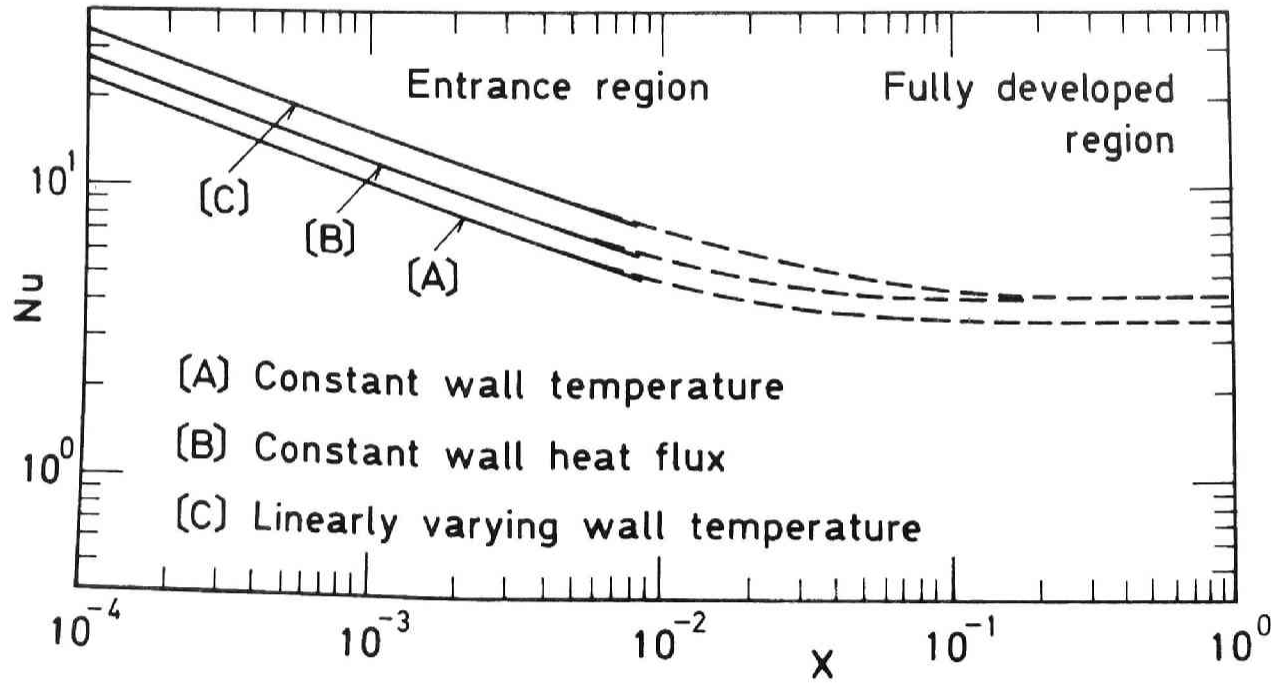


Fig. 3.1. Local Nusselt number in steady flow.

and boundary conditions become

$$F_p = 0 \left(\frac{d\bar{F}_p}{d\eta} = \bar{F}_p = 0 \right) \quad \text{at} \quad \eta \rightarrow \infty \quad (3.16)$$

$$F_p = 0 \left(\bar{F}_p = 0 \right) \quad \text{at} \quad \eta = 0$$

Note that there appears variable X in both Eqs. (3.13) and (3.14). Therefore, the similarity relation does not hold for unsteady temperature profiles in pulsating flow. However, if $\text{SnPr}X^{2/3}$ is regarded as a parameter, these ordinary differential equations are easily treated as first approximations. Hence the numerical solutions of Eqs. (3.13) and (3.14) were obtained by using the Runge-Kutta-Gill method with an application of the principle of superposition. As the upper boundary, $\eta = 2$ was selected instead of the infinite value because at $\eta = 2$, F_s and $dF_s/d\eta$ are less than 1.5×10^{-3} .

The amplitude ratio and phase lag were calculated by

$$\text{amplitude ratio} = \sqrt{\text{Re}^2(Z) + \text{Im}^2(Z)} \quad (3.17)$$

and

$$\text{phase lag} = -\tan^{-1} \{ \text{Im}(Z) / \text{Re}(Z) \} \quad (3.18)$$

where

$$Z = \frac{\text{Nu}_p}{\text{Nu}_s} / \frac{1}{3} a_\tau \quad (3.19)$$

for pseudo-steady state

$$\frac{\text{Nu}_p}{\text{Nu}_s} = \frac{1}{3} a_\tau \quad (3.20)$$

The results for these three heating conditions are shown in Fig. 3.2. For conditions [A] and [B], the

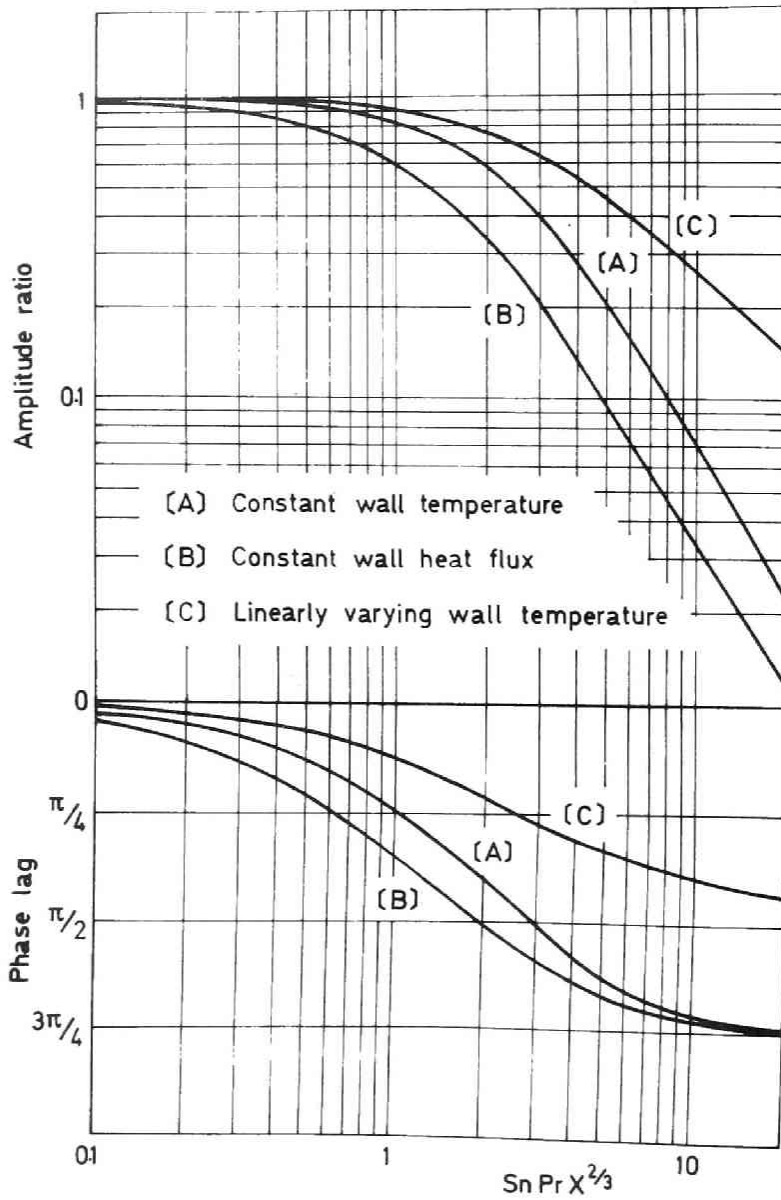


Fig. 3.2. Bode diagram of local Nusselt number for three heating conditions.

variations of amplitude and phase lag with respect to $\text{SnPrX}^{2/3}$ are similar. While for condition [C] the tendency of variation differs from the other two heating conditions. Especially at large values of $\text{SnPrX}^{2/3}$ the phase lag approaches $\pi/2$ for condition [C] but $3\pi/4$ for the others. Concerning the frequency response under heating condition [A], Fig. 3.3 shows a comparison between the solution of Eq. (3.13) and those calculated from Lighthill's approximation [11], which is valid for high frequency, and those of Lebouché's approximation [9] and those of Fortuna and Hanratty's calculation [4]. They are in good agreement with each other within a limited region.

For each experimental condition, the numerical solutions of Eq. (3.5) are also obtained, which does not comprise the similarity relation, and as well as for the following equation

$$\frac{\partial \Gamma}{\partial \theta} + \left(\frac{1}{2} R^2 + \frac{U_p e^{i\omega t}}{4 \langle U \rangle_s} \right) \frac{\partial \Gamma}{\partial X} = \frac{1}{R} \frac{\partial}{\partial R} \left(R \frac{\partial \Gamma}{\partial R} \right) \quad (3.21)$$

where the pulsating velocity profile U_p was calculated from Eq. (2.6) in Section 2.3.3. Equations (3.5) and (3.21) were calculated by using a finite difference method. Several solutions of varying grid size were used in the usual way to determine that satisfactory accuracy was obtained.

3.3 Test Section and Measuring Equipment

The experiments of frequency response were conducted for local value of heat transfer coefficient under heating

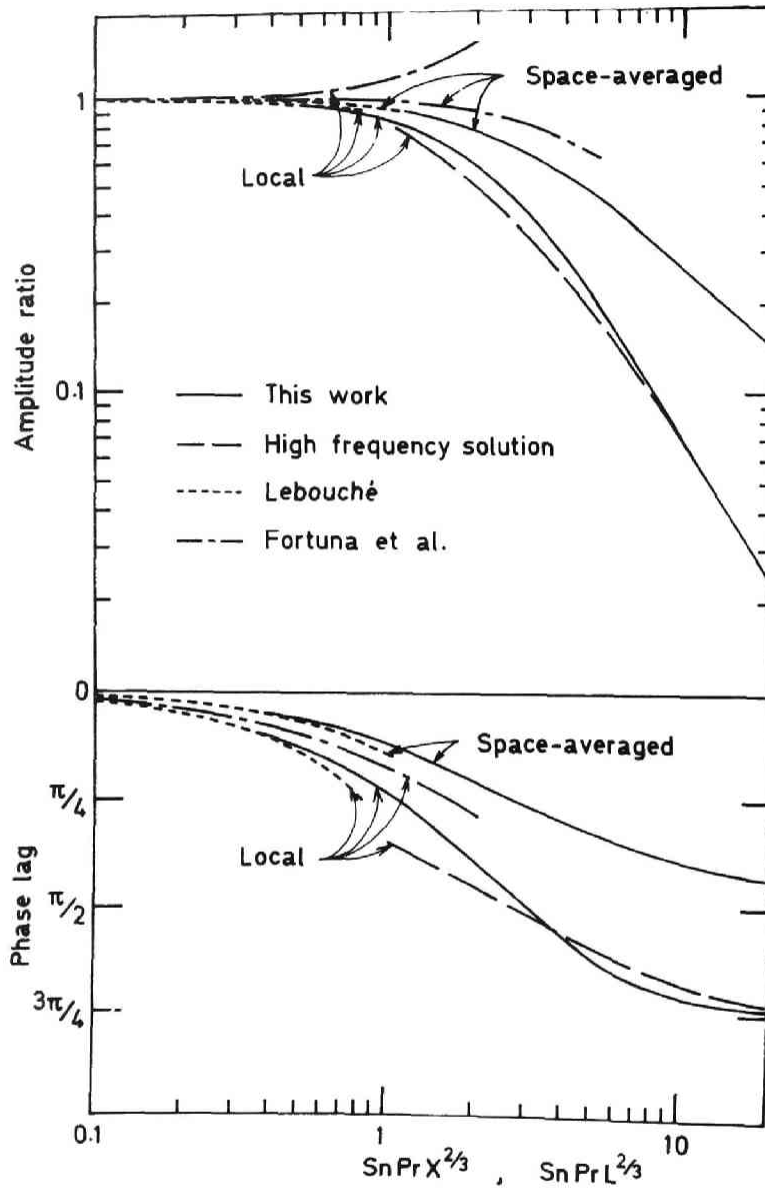


Fig. 3.3. Comparison of analytical results of several investigators.

condition [B] and for space-averaged value of mass transfer coefficient under heating condition [A].

The test section was a round tube of smooth surface of 2 cm inside diameter. To measure the wall temperature under heating condition [B], as shown in Fig. 3.4, the copper-constantan thermocouple sheets were embedded in the plastic inner wall; the surface was made flush, and nickel film was coated on the whole surface by chemical plating. Its thickness was about 0.5μ and its length was 50 cm. The terminals at both ends of this film were jointed to copper rings which were connected to a variable transformer stepped down from a 100-V., a.c. electrical source. The cold junction of the thermocouple was located upstream of the heated section so that the readings of the thermocouple indicate the difference between bulk and wall temperatures. The difference between bulk and wall temperatures was maintained within 5° C by changing the wall heat flux with a variable transformer to suppress the temperature dependency of fluid properties. The circulated liquid was water ($Pr = 7.87$ at 16°C) or a solution of 55 wt.% glycerol and 45 wt.% water ($Pr = 70.9$ at 16°C). The pressure drop as input signal was measured by a pressure transducer. The distance between the two pressure taps was 200 cm.

For heating condition [A], an experiment of mass transfer in a diffusion-controlled electrolytic reaction [12] was conducted. The circulated liquid was an aqueous solution of 0.001 - 0.01 mole of $\text{K}_4\text{Fe}(\text{CN})_6$ and $\text{K}_3\text{Fe}(\text{CN})_6$ per litre with 2N KOH ($Sc = 427$ at 50°C), 3N KOH ($Sc = 2390$ at 20°C), 5N KOH ($Sc = 3130$ at 20°C) or 5N NaOH ($Sc = 16020$ at 17°C) as a supporting electrolyte. The test section (2 cm I.D. circular tube) consisted of

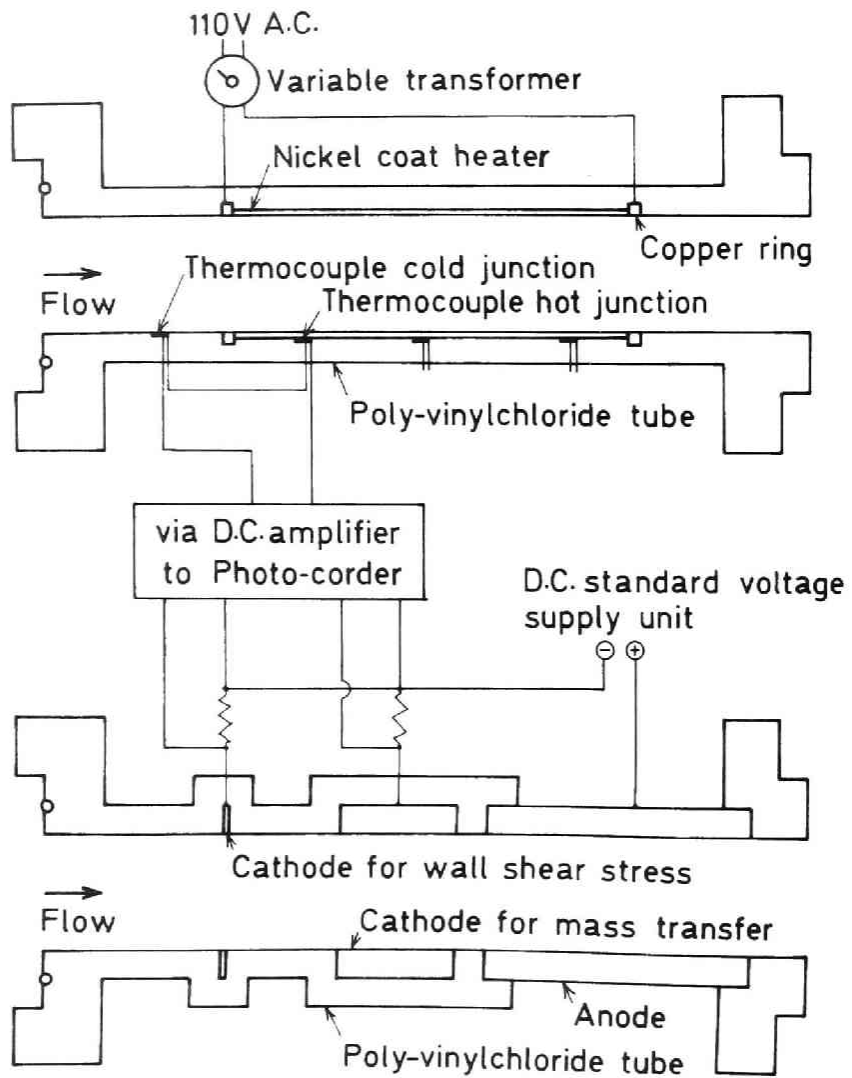


Fig. 3.4. Test sections.

nickel ring and an anode of nickel pipe, the surface area of which was larger than that of the cathodes. All surfaces of cathodes and anode were carefully made flush to form a single tube. The variation of mass transfer coefficient was recorded as the variation of electric current density in diffusion-controlled electrolytic reaction at limiting current. The change of wall shear stress as input variation was measured with a very small cathode (length of mass transfer section $\ell = 0.007$ cm) located at the entrance of the test section.

3.4 Experimental Results and Discussion

3.4.1 Transfer coefficient in steady flow

Prior to running the experiments in pulsating flow, the local heat-transfer coefficients and space-averaged mass-transfer coefficients in steady flow were measured. As shown in Fig. 3.5, the experimental results for heating conditions [A] and [B] are correlated well with L  v  que's solution [10] and Bird's solution [2], respectively. These results show the similarity relation between X and Y is valid over the whole region of the experimental condition of this study.

3.4.2 Experimental curve of transfer coefficient in pulsating flow

On a steady flow of $Pr = 7.87, 70.9$ and $Sc = 427, 2390, 3130, 16020$, a pulsating flow of pulsation period $T = 0.76 - 7.9$ sec ($T = 7.9$ sec only in local heat transfer measurements) was overlapped and the local transfer coefficients at positions of $x = 2.5$ cm, 5cm,

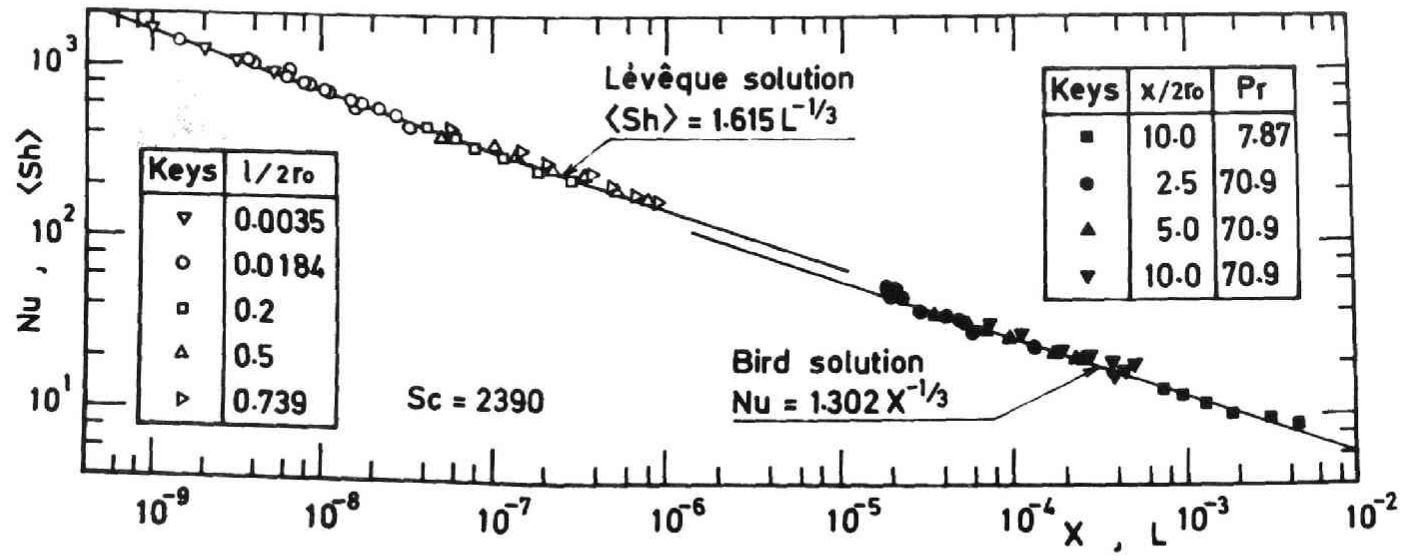


Fig. 3.5. Local Nusselt number and space-averaged Sherwood number in steady flow.

10 cm and 20 cm, and the space-averaged transfer coefficients on surfaces of $\ell = 0.4$ cm and 1 cm, were measured. Examples of experimental curves are shown in Figs. 3.6 and 3.7. Figure 3.6 shows that there are apparent phase shifts between the variation of pressure drop and that of reciprocal of temperature difference (which corresponds to Nusselt number). In Fig. 3.7, there can be seen the same trend between the variation of wall shear stress and that of mass flux (which corresponds to Sherwood number).

3.4.3 Frequency response of local Nusselt number

By the same method as that described in Section 2.3.2, the amplitude ratio and phase lag of output signal to the input signal were calculated. The results for local Nusselt number are shown in Figs. 3.8 and 3.9. In these diagrams, as Eq. (3.19) suggests, the variations of wall shear stress are used as input signal. The amplitude and phase of wall shear stress were calculated from the amplitude and frequency of the measured pressure drop by using Sexl's analysis (see Section 2.3.2).

Numerical calculations of Eqs. (3.5) and (3.21) at the value of $SnPr$ of these experimental conditions were also shown in these figures. The curves are almost coincident with each other. Therefore, up to the region where X is nearly equal to 10^{-2} , the approximation of linear velocity profile seems to be valid as in the case of steady state. In addition, these calculations correlate the experimental data fairly well; discrepancy found in the phase lag is supposed to be caused by an experimental error. On the other hand, it is clear that the first approximation, Eq. (3.14) is only valid at very high and low frequencies.

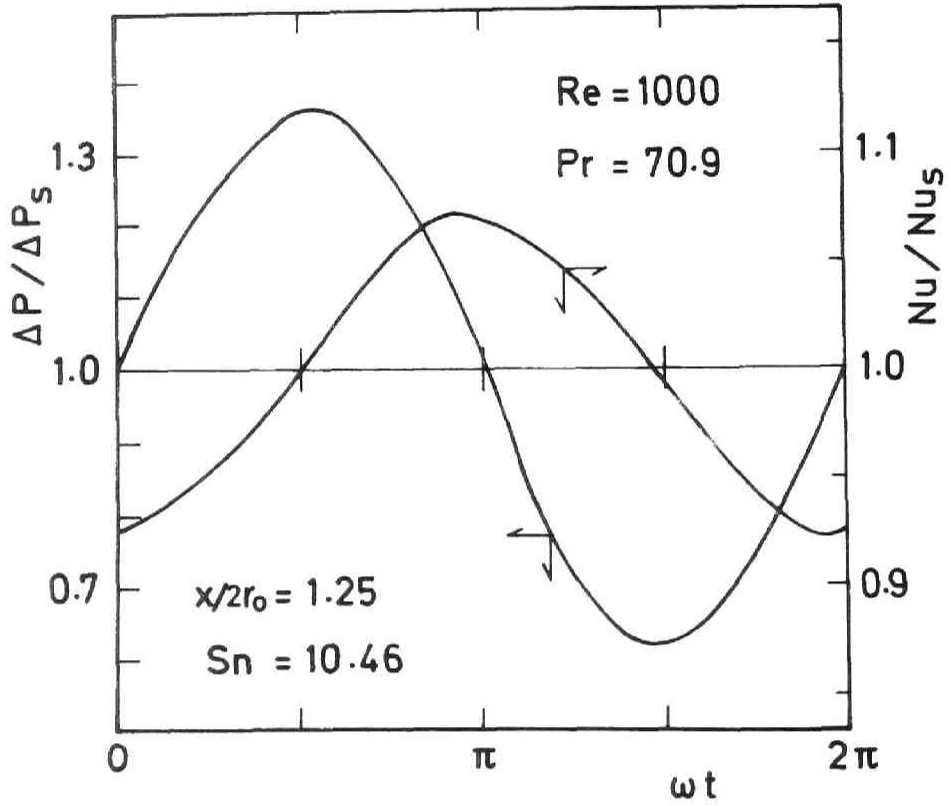


Fig. 3.6. Variations of pressure drop and Nusselt number.

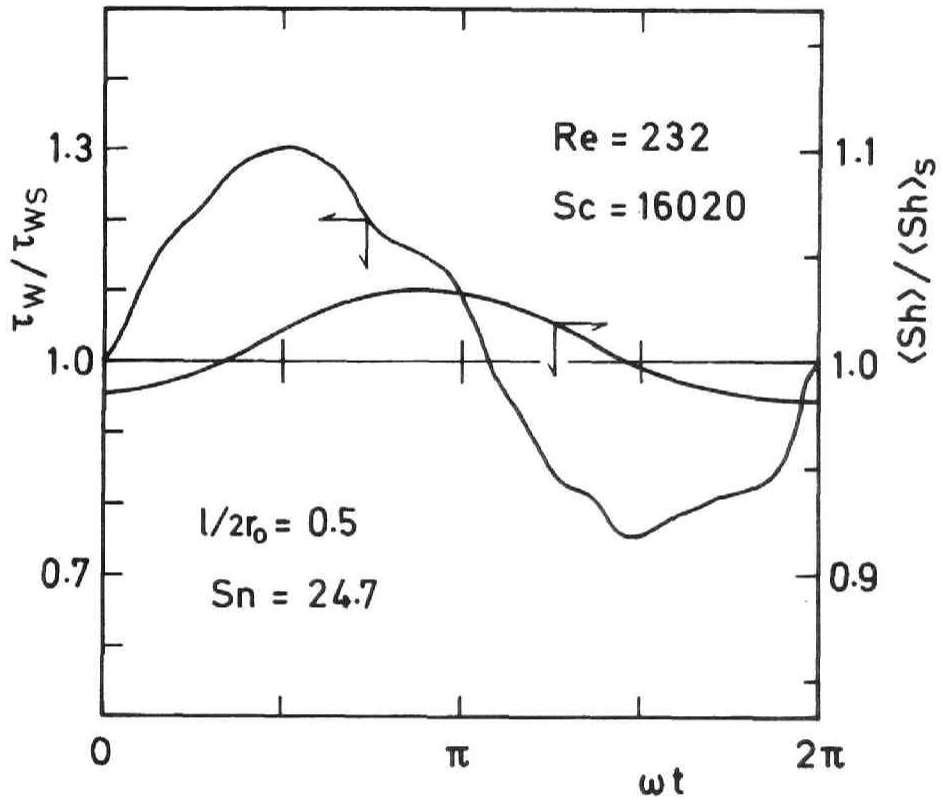


Fig. 3.7 Variations of wall shear stress and Sherwood number.

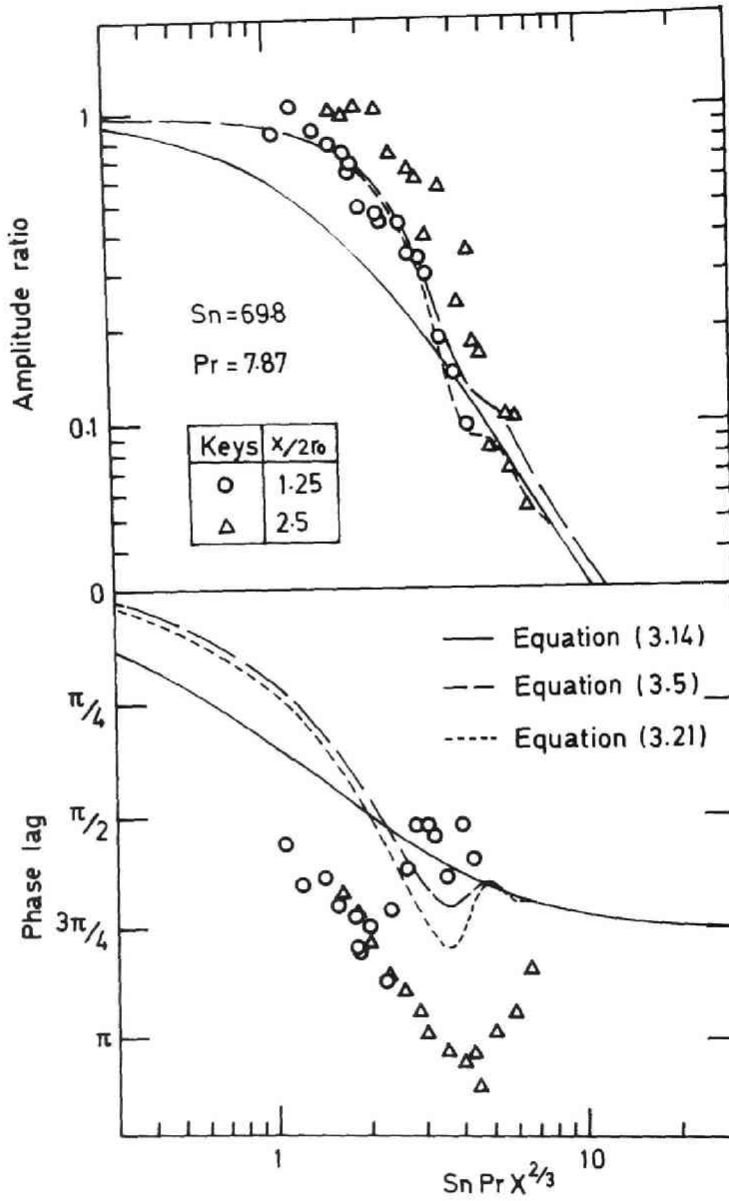


Fig. 3.8. Bode diagram of local Nusselt number for constant wall heat flux.

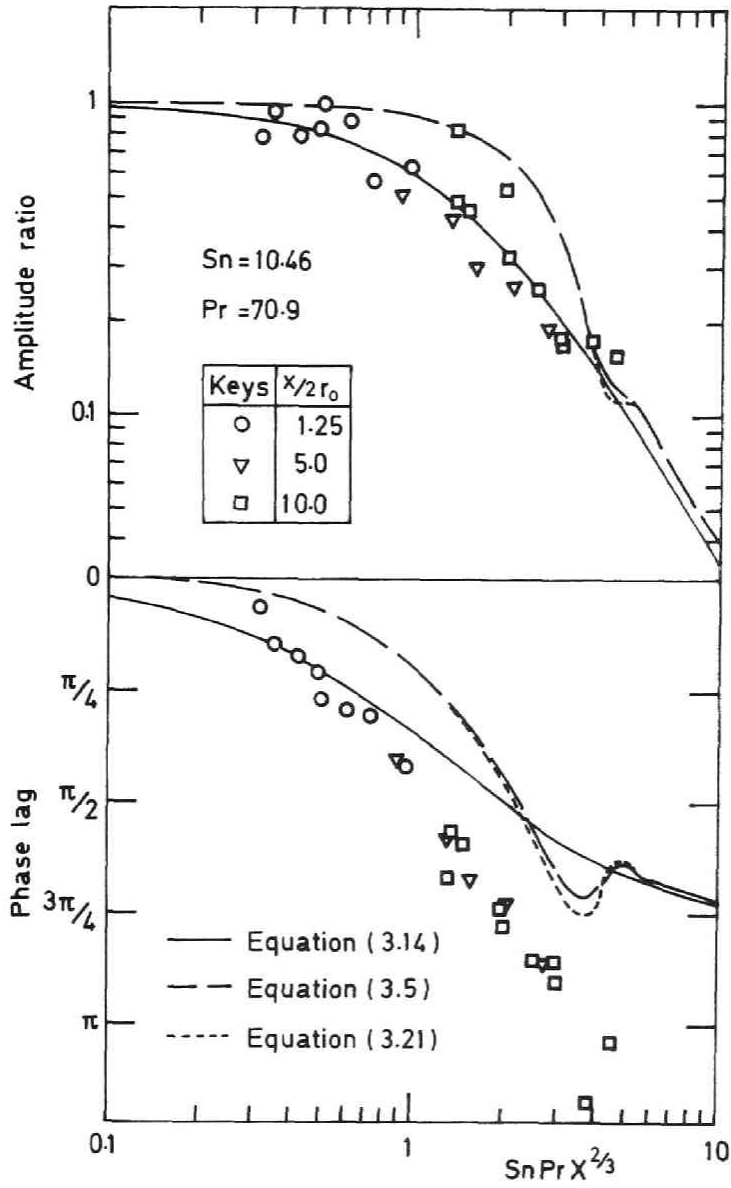


Fig. 3.9. Bode diagram of local Nusselt number for constant wall heat flux.

3.4.4 Frequency response of space-averaged Sherwood number

The local values of Sherwood number for maximum and minimum values of $S_n S_c$ of the experimental condition were calculated numerically from Eq. (3.5). These were coincident within an accuracy of 1 %. Integrating the local values gives the space-averaged values. In Fig. 3.10, these results are compared with the first approximation. The local values represent the same trends as in the case of constant wall heat flux. With respect to the space-averaged value, oscillation on bode diagram is reduced and the deviation from the first approximation is smaller than the cases of local value.

Together with these lines of space-averaged values, experimental results are plotted in Fig. 3.11. Though the amplitude ratios of experimental results are a little larger than the analytical values, the experiments are well correlated by the analytical solutions.

3.4.5 Resonance point

Siegel *et al.* [21] pointed out that a node in wall temperature or heat flux existed at every integer multiple of the length $X = \pi/2 S_n Pr$ which is the distance that the fluid travels during a complete oscillating cycle. Mochizuki *et al.* [13] showed that the node existed at each integer of multiple of $X = 3\pi/4 S_n Pr$, which is the distance that the fluid at centreline of the tube travels during a complete oscillating cycle.

The minimum points of amplitude ratio in Figs. 3.8 – 3.10 show that there also exist nodes in the entrance region of heat transfer. The points of node can be called

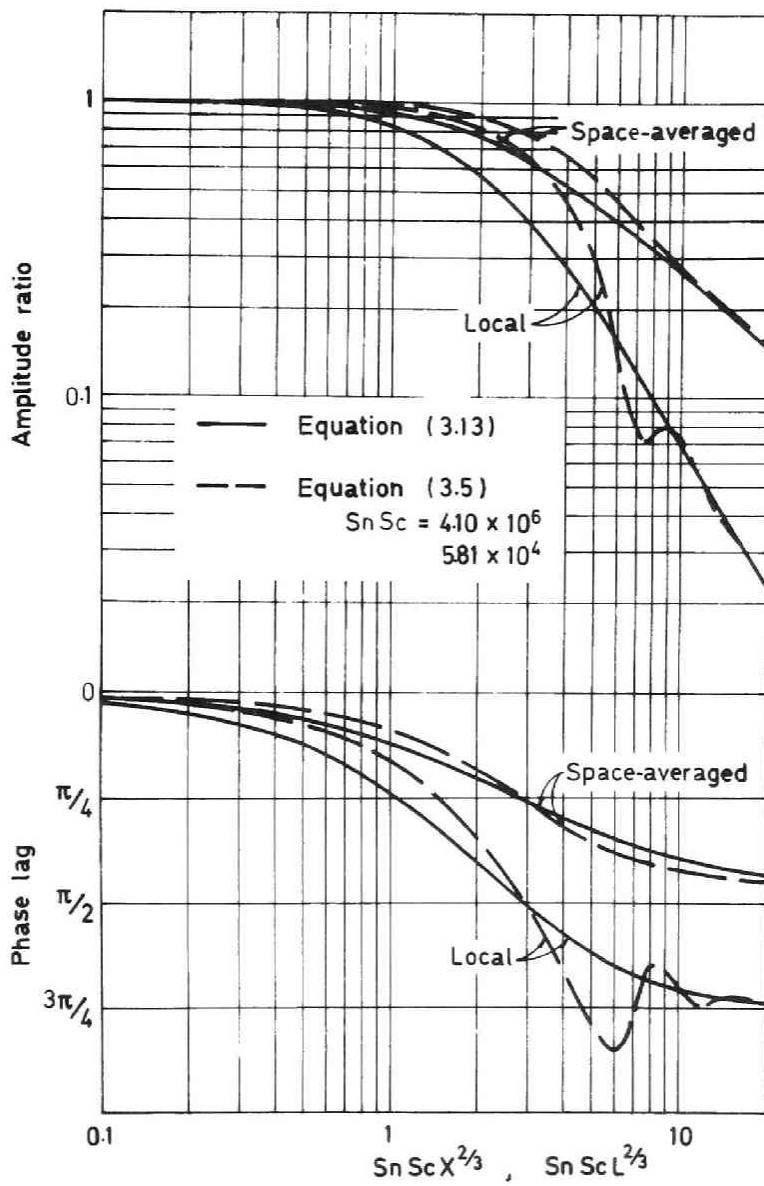


Fig. 3.10. Bode diagram of local and space-averaged Sherwood number for constant wall concentration.

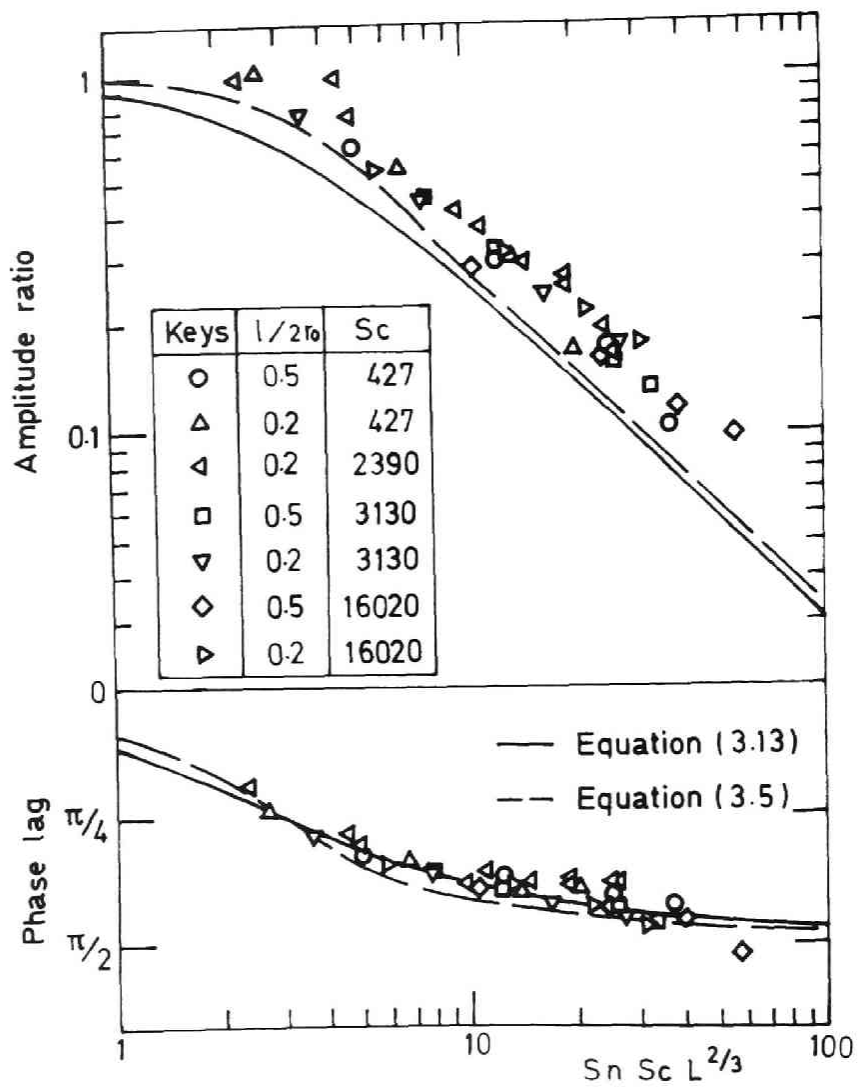


Fig. 3.11. Bode diagram of space-averaged Sherwood number for constant wall concentration.

resonance points, because the 'resonance' reported in the study of heat exchanger dynamics [22] with approximation of constant transfer coefficient is essentially the same as the phenomenon of the node appearance in the transfer coefficient. The numerical results in this work reveal that the resonance point does not scale with above mentioned $SnPrX$ but with $SnPrX^{2/3}$ which was obtained from similarity relation: $SnPrX^{2/3} = 7.5$ under heating condition [A] and $SnPrX^{2/3} = 4.6$ under heating condition [B]. This means that a characteristic velocity which controls the resonance is the velocity at one position which is expressible by using the similarity variable ($\eta = 0.56$ and $\eta = 0.34$, respectively).

3.4.6 Effect of flow pulsation on time-averaged transfer rate

It has been clarified from the analytical point of view that the time-averaged rate of heat transfer was not appreciably changed by flow pulsation, in the developing region by Siegel *et al.* [21], in the entrance region by Alabastro *et al.* [1]. However, some experimental studies showed that there was an increase of heat transfer coefficient in pulsating flow. This seems to be due to the following facts.

The analytical studies were made under the condition that the amplitude of pressure drop or wall shear stress as input is less than the steady component. On the other hand, in most experimental studies, the pulsating component of the flow rate was kept less than the steady component. So when the pulsating component of flow rate is large, the wall shear stress goes beyond zero, that

is, reverse flow occurs near the wall, because wall shear stress changes more quickly than flow rate with increasing frequency as described in Section 2.3.2. During the period of reverse flow, however, the mass transfer rate or temperature difference in the entrance region of heat transfer is still positive. As a result the integration of the oscillating curve of transfer coefficient with respect to time, i.e. the time-averaged value of transfer coefficient becomes larger than the steady-state one.

The experimental verification of this consideration was conducted by measuring the variations of pressure drop, flow rate and space-averaged mass-transfer rate in pulsating flows of large amplitude. The flow rate was measured by electromagnetic flowmeter. Figure 3.12 illustrates one example of such experimental results. The amplitude of flow rate is one half of the steady value and so the fluid as a whole does not flow reversely in any instance, while the amplitude of wall shear stress, which was calculated from the measurement of pressure drop, is larger than the steady-state value and so the fluid near the wall flows reversely at about $\omega t = \pi$. Nevertheless, the mass transfer coefficient is consistently positive, indicating the distortion of the curve by reverse flow near the minimum value. The greater the amplitude and smaller the steady flow rate, the more noticeable this phenomenon became. The tendency is similar to the experimental results of time-averaged mass-transfer rate by Shirotzuka [20].

However, this effect is of little use for practical application, because as seen in Fig. 3.11 the amplitude ratio of transfer coefficient decreases rapidly with

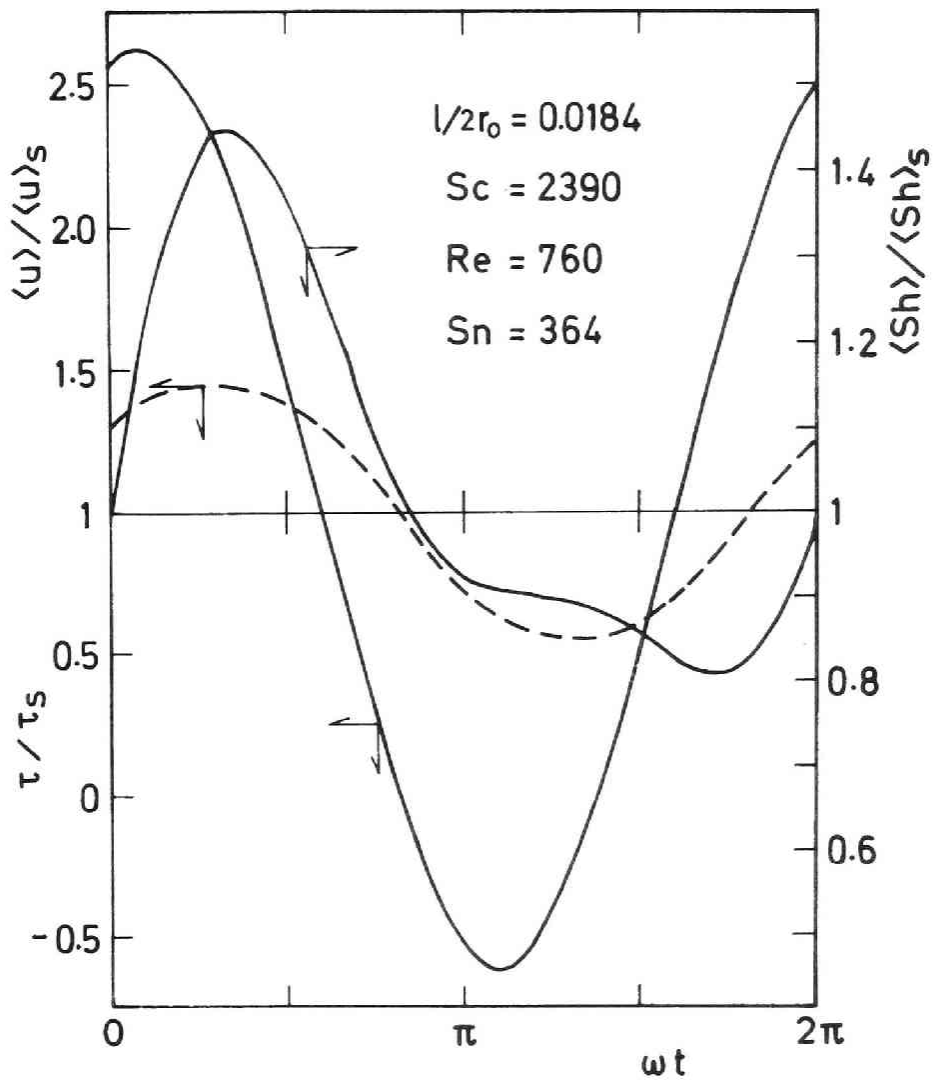


Fig. 3.12. Variations of wall shear stress, flow rate and Sherwood number.

increasing transfer length and increasing frequency at which the reverse flow becomes conspicuous.

3.5 Conclusion

1. Over the region where steady-state transfer is subject to the linear velocity gradient near the wall, the same linear profile can be used in analysis of unsteady-state transfer.
2. The similarity relation between X and Y which is valid in steady-state transfer does not exist in unsteady-state transfer.
3. The amplitude ratio and phase lag oscillate around the first approximations obtained from assuming the similarity relation owing to the history of the fluid from the inlet section of transfer.
4. The resonance point which appears explicitly in the local value is characterized by $SnPrX^{2/3}$. This parameter is obtained from the similarity relation and it means that the characteristic velocity of the resonance is determined by the steady thermal condition.
5. In the space-averaged value, the nonsimilarity between X and Y is reduced, and the amplitude ratio and phase lag change smoothly with respect to frequency.
6. The phase lag of space-averaged values approaches $\pi/2$ at large value of $SnPrL^{2/3}$, while that of the local value approaches $3\pi/4$.
7. The increase of time-averaged value of transfer rate is mainly due to reverse flow near the wall at large amplitude of the flow rate.

4.1 Introduction

This chapter deals with the experiments on the dynamic behaviour of velocity and some turbulence characteristics in pulsating turbulent flow.

In chapter 2, the eddy viscosity of pulsating turbulent flow was assumed to be similar to that of steady flow, and this assumption was verified to be useful for the prediction of frequency response of momentum transfer. However, actual behaviour of turbulence is inferred to be changed by flow pulsation; especially when the amplitude of pulsation is large and the pulsation period is the same order as those of bursting, an essential change of structure and production of turbulence may occur. On the other hand, even in steady turbulent flow the bursting phenomenon [3, 8] shows a periodicity and large axial velocity change, i.e. deceleration and acceleration. Accordingly, it is believed that an investigation of the periodicity of bursting in pulsating turbulent flow can reveal the essential aspects of turbulence generation in pulsating flow as well as in steady turbulent flow. Thus the condition that is chosen for the study is the pulsating turbulent flow in which the amplitude of velocity pulsation is larger than that of turbulent fluctuation near the wall.

First, under constant Reynolds number ($Re = 10^4$), the profiles of velocity and some turbulence characteristics were examined dynamically over the wide range of

pulsation period. Secondly, the burst period of both steady and pulsating flows were measured and the relation between the burst period and that of pulsation was made clear. Finally, such relations were obtained at other Reynolds numbers for a systematic treatment of pulsating turbulent flow.

4.2 Test Section and Measuring Equipment

The test section is a circular tube of smooth surface, 2 cm internal diameter and 2 m in length; it is located downstream of a forerunning section of 150 diameters long. At the test section, a pressure drop between two points 175 cm apart was measured by a pressure transducer, and an instantaneous velocity profile was measured by the electrochemical method [12]. The working fluid is an aqueous solution ($\rho = 1.046 \text{ g/cm}^3$, $\mu = 0.0112 \text{ g/cm}\cdot\text{sec}$ at 20° C) of 0.01 mole of $\text{K}_4\text{Fe}(\text{CN})_6$ and $\text{K}_3\text{Fe}(\text{CN})_6$ per litre with 1N KOH as a supporting electrolyte.

The electrical circuitry being used is shown in Fig. 4.1. The instantaneous velocity was converted into electric current by using the electrochemical method. Its voltage drop across a standard resistor was amplified with a d.c. amplifier. The electrical signal from this amplifier and that from the pressure transducer mentioned above were recorded on separate channels of a magnetic tape using a tape recorder (Teac Model R-400). For analog-digital conversion, a hybrid computer (Hitachi Cloap 2000) was used.

Concerning the time between bursts, a correlator

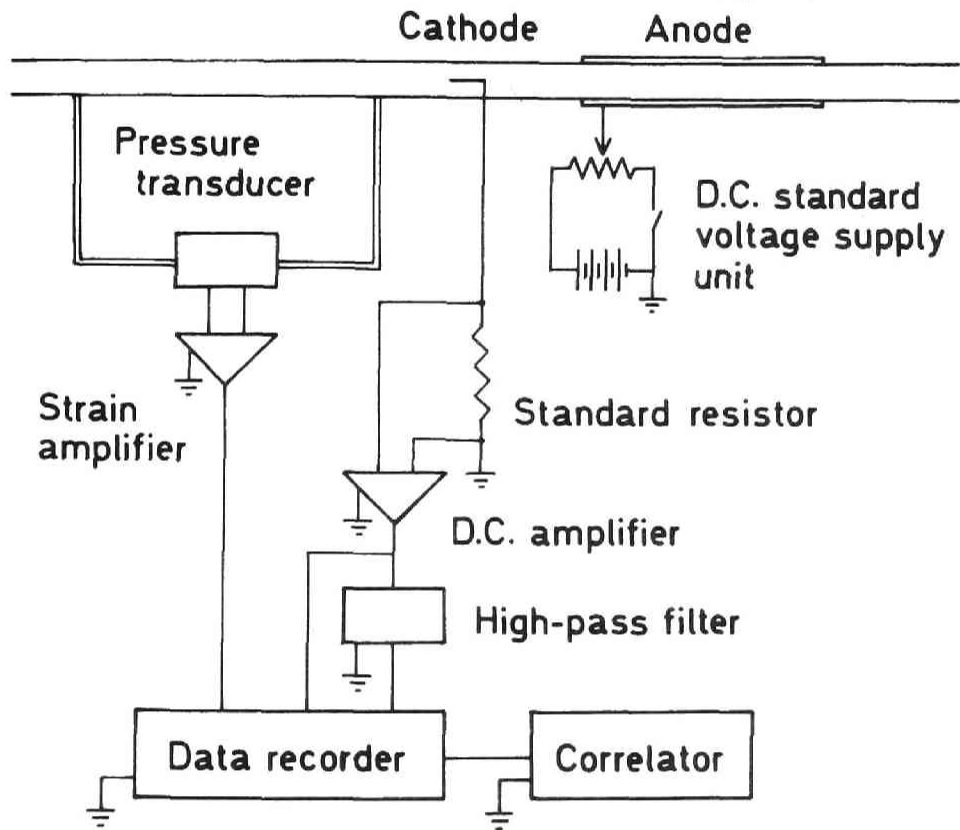


Fig. 4.1. Electrical circuitry.

(Teac Model C-100) was used to determine the time delayed auto- and cross-correlations. The original signal is separated by cut-off high- and low-pass filters (Kanomax Model 21-1211) into the fluctuating component and the pulsating component, from which the cross-correlation is calculated.

Figure 4.2 shows the probe used (a cathode of electrochemical method; this is not a hot-wire anemometer) and its calibration curve. The probe consists of a platinum wire (diameter 0.1 mm, length 1.1 mm) and glass fusing supports which are connected with a stainless-steel support.

4.3 Results and Discussion

4.3.1 Profiles in steady flow

Prior to running the experiments of pulsating flow, the characteristics of steady turbulent flow, namely the mean velocity and the r.m.s. fluctuation profiles, were determined. The turbulence intensity profile shown in Fig. 4.3 and the velocity profile are in sufficiently good agreement with the measurements of other investigators [16].

Taking into account of the fact that the frequency of the pulsation of velocity is an order of magnitude lower than the frequency of turbulent fluctuation, it may be concluded from Fig. 4.3 that no correction for the measured value of the pulsating velocity is necessary, although the dynamic response of this kind of probe has not yet been clarified.

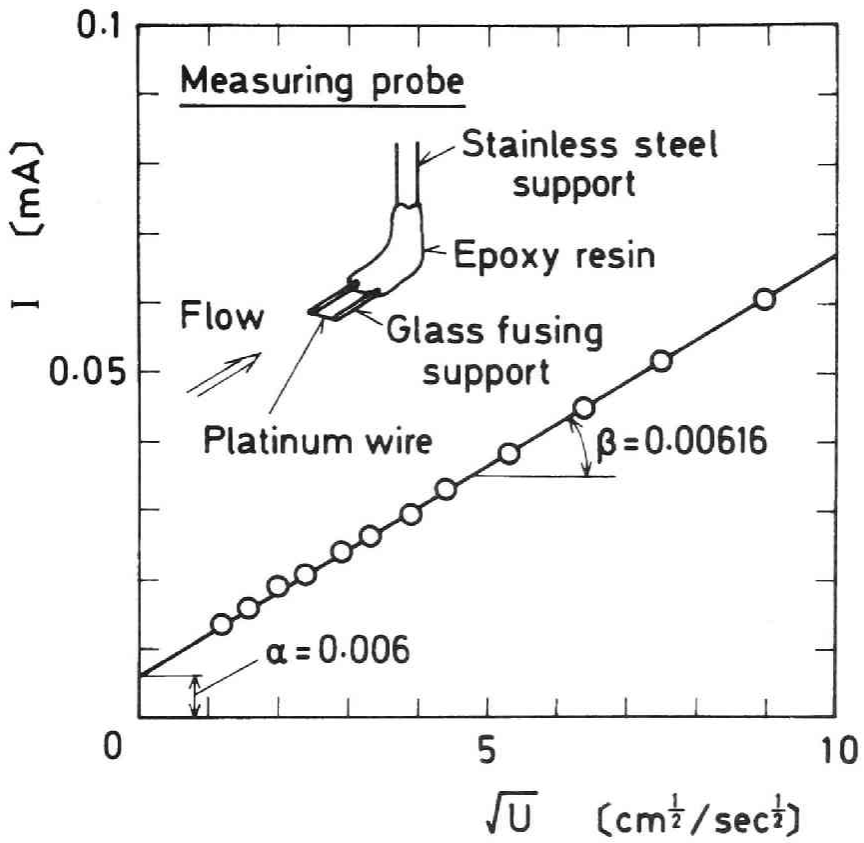


Fig. 4.2. Probe for measuring velocity and its calibration curve.

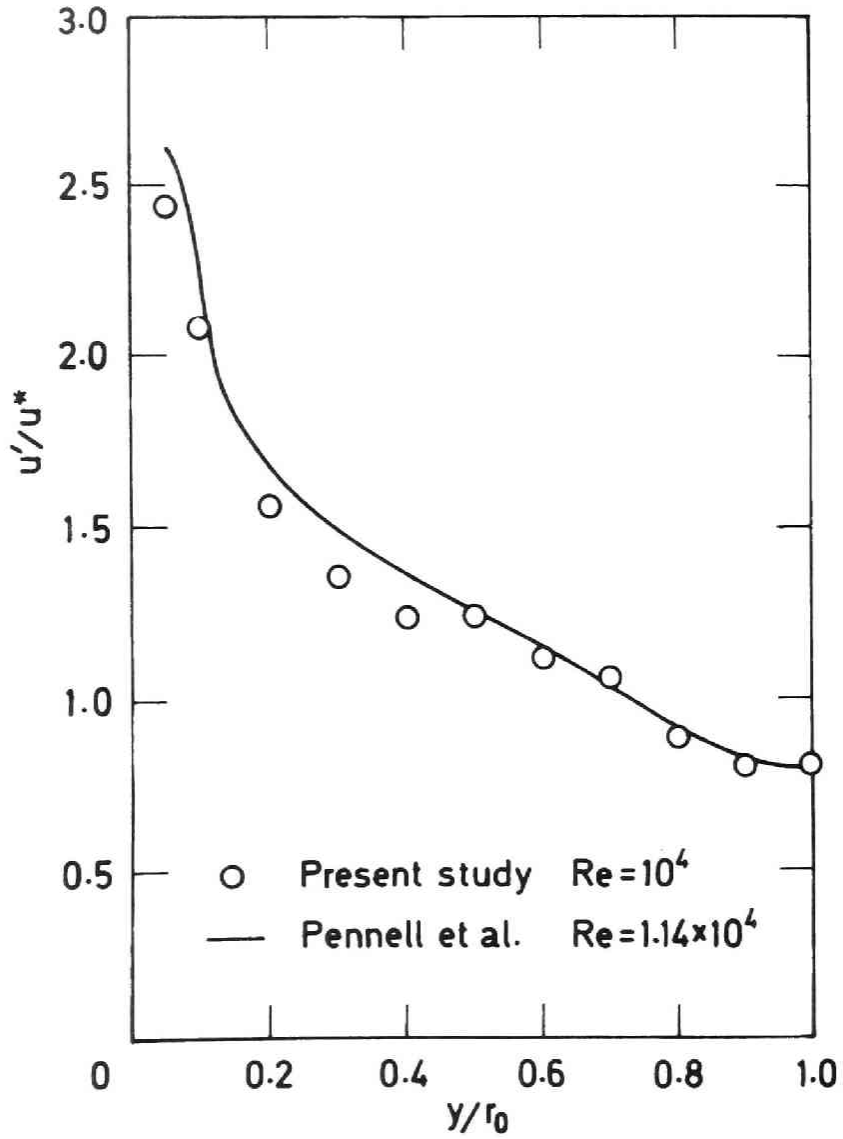


Fig. 4.3. Turbulence intensity profile in steady flow.

4.3.2 Velocities in pulsating flow

Figure 4.4 illustrates one example of velocity variation with respect to time. Apparently, the determination of pulsating component from only one cycle is not accurate enough. Accordingly, the phase average, i.e. an average of the corresponding value from several different cycles at the same phase angle, was made:

$$U(t) = \frac{1}{N} \sum_{n=1}^N U_i(t + nT) \quad (4.1)$$

where $U_i = U + u$, and $N = 20$ were chosen. The same averaging procedure was used to determine the change of pressure drop.

For calculating the turbulence intensity by extracting the turbulent component, however, a procedure of this kind would require a longer recording time and a higher exactness in the hybrid computer than are available, in order to do enough subtractions of U from U_i at exactly the same phase angle. On the other hand, the experiments reveal that the frequencies of turbulent fluctuations, which contribute the essential part to the intensity, are an order of magnitude higher than those of pulsation. Hence the pulsating component was removed with a high-pass filter and the small effect of amplitude attenuation by the filter was corrected using an attenuating ratio measured in the steady flow; thus the error caused by the filtration could be eliminated satisfactorily.

The calculation of turbulence intensity were made by using

$$u'(t) = \sqrt{\frac{1}{N \times M} \sum_{n=1}^N \sum_{m=1}^M \{u(t + nT + m\Delta T)\}^2} \quad (4.2)$$

Pulsating flow



Turbulent fluctuation



Fig. 4.4. Variations of velocity and turbulent fluctuation with respect to time ($T < T_c$).

where $M = 7$, $N = 20$ and $M\Delta T/T = 1/32$ were chosen to avoid too long recording and calculation times, based on the experimental fact that the intensity of turbulence changes continuously and smoothly.

As for analog-digital conversion, it required very high accuracy to adjust an external clock to the pulsation period T . Hence, it was always checked whether the autocorrelation coefficient of $\Delta P/\Delta x$ at T took a maximum value.

The calculations of $\Delta P/\Delta x$, U and u' were made for 11 radial points and at 16 phase angles within one cycle, starting from a time when the pressure drop had the same value as in steady-state flow, i.e. $\omega t = 0$. The curves for the pressure drop and for the velocity U in pulsating flow were nearly sinusoidal. Using above-mentioned phase angle, the pulsating profiles of velocity and of turbulence intensity were obtained.

From the measurements at various period of pulsation ranging from 0.76 to 7.9 sec, it is found that the results can be clearly classified into two groups by a critical period of pulsation T_c . Those two groups will be distinguished by calling them Profiles I ($T > T_c$) and Profiles II ($T < T_c$), respectively. Detailed discussions will be found in the following sections, where two typical results normalized with τ_w , u^* and R^+ (determined in the steady-flow condition) are shown.

4.3.3 Profiles I ($T > T_c$)

Figure 4.5 shows the velocity profiles in pulsating flow, where the plots indicate the measurements and the curved lines indicate the approximated biquadratic equa-

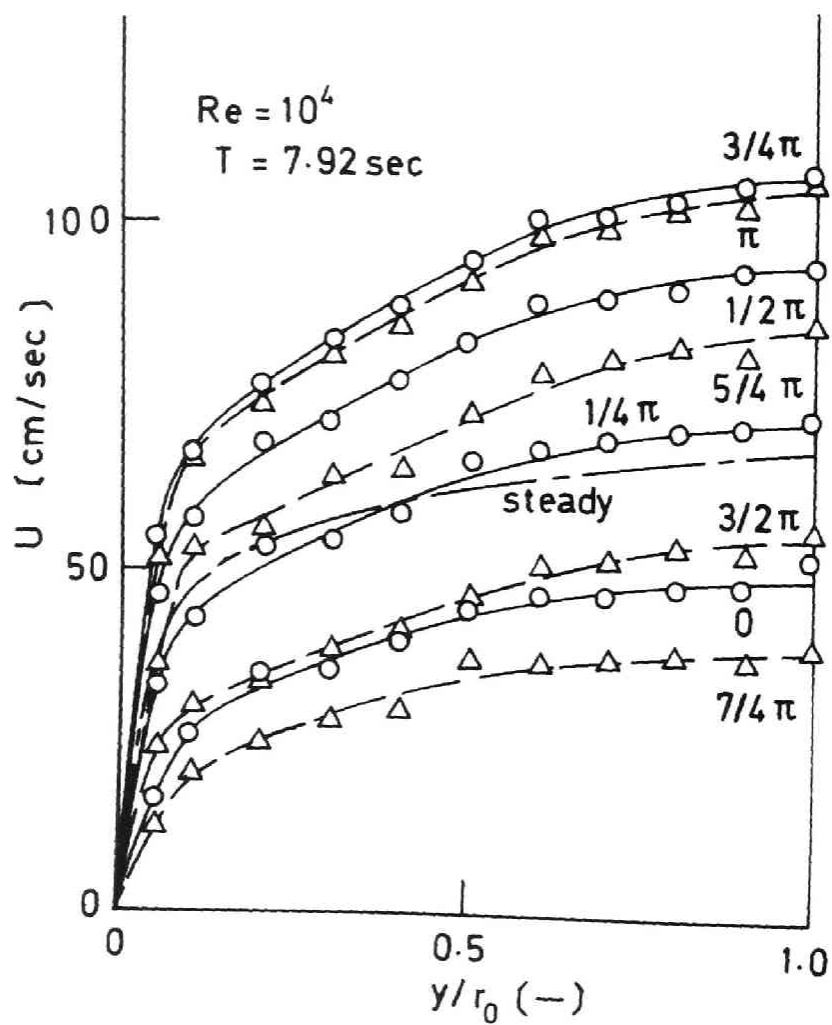


Fig. 4.5. Velocity profiles in pulsating flow ($T > T_c$).

tions obtained by the least squares method. The profile for steady flow is also included. The parameter varied in this diagram is the phase angle (based on one cycle of the pressure-drop curve).

The velocity profiles in pulsating flow are similar to that in steady flow, but mostly their radial gradients are a little larger, as can be seen from Fig. 4.5.

Figures 4.6 and 4.7 show the shear stress profiles and the Reynolds stress profiles, respectively. These were calculated by the integrated equation of motion, i.e.

$$\tau = \frac{r\rho}{2} \left\{ \frac{1}{\rho} \frac{\partial P}{\partial x} - \frac{\partial}{\partial t} \left(\int_0^r 2\pi r' U dr' / \pi r^2 \right) \right\} \quad (4.3)$$

Both results point out the similarity to those in steady flow.

Eddy viscosity profiles are shown in Fig. 4.8. The values in pulsating flow in most parts are smaller than those in steady flow, so the variation of the Reynolds stress is not so large as the variation of the velocity gradient.

Figure 4.9 shows the profiles of intensity of turbulence. Unlike the velocity pulsation, the intensity of turbulence does not vary so much. It seems that the turbulent fluctuations are not affected by the pulsating flow.

As the velocity profiles in pulsating flow are similar to that for steady flow, the system seems to reach its equilibrium state at every moment. But this cannot be concluded; as the intensity of turbulence does not change with the flow pulsation, the system does not

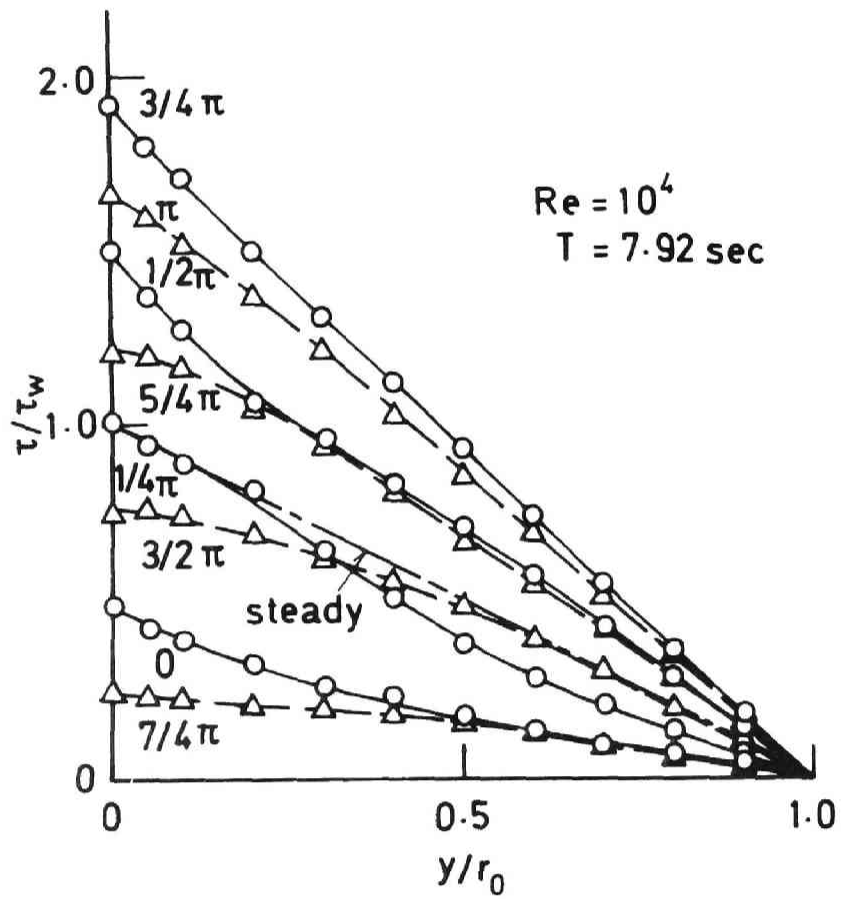


Fig. 4.6. Shear stress profiles in pulsating flow ($T > T_c$).

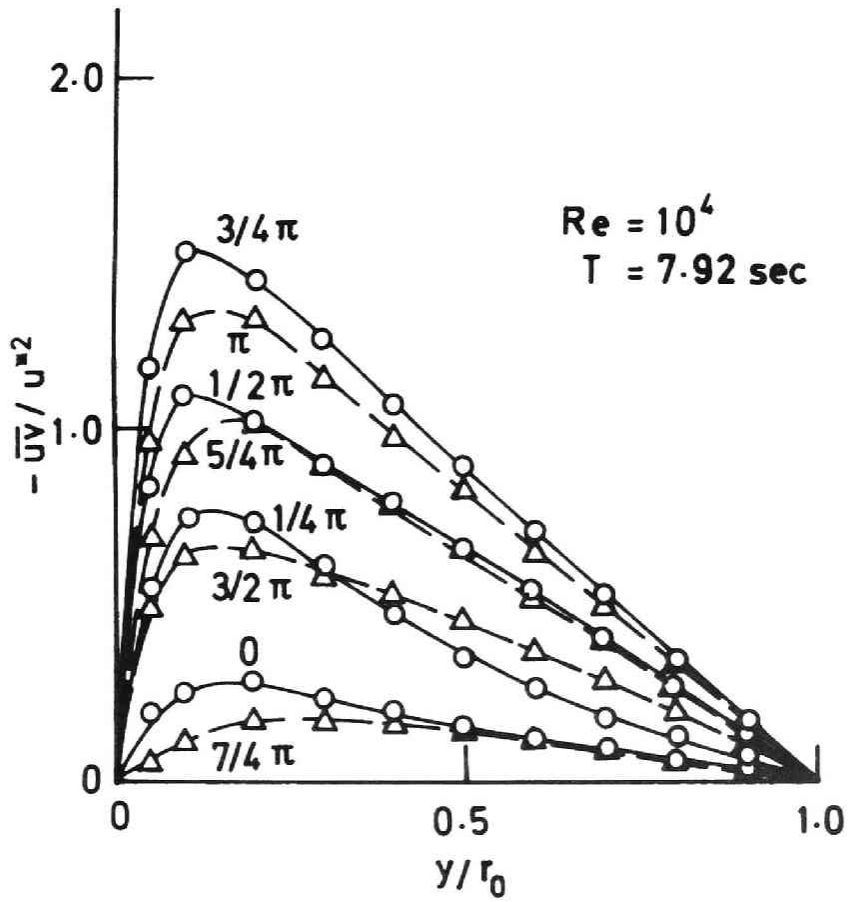


Fig. 4.7. Reynolds stress profiles in pulsating flow ($T > T_c$).

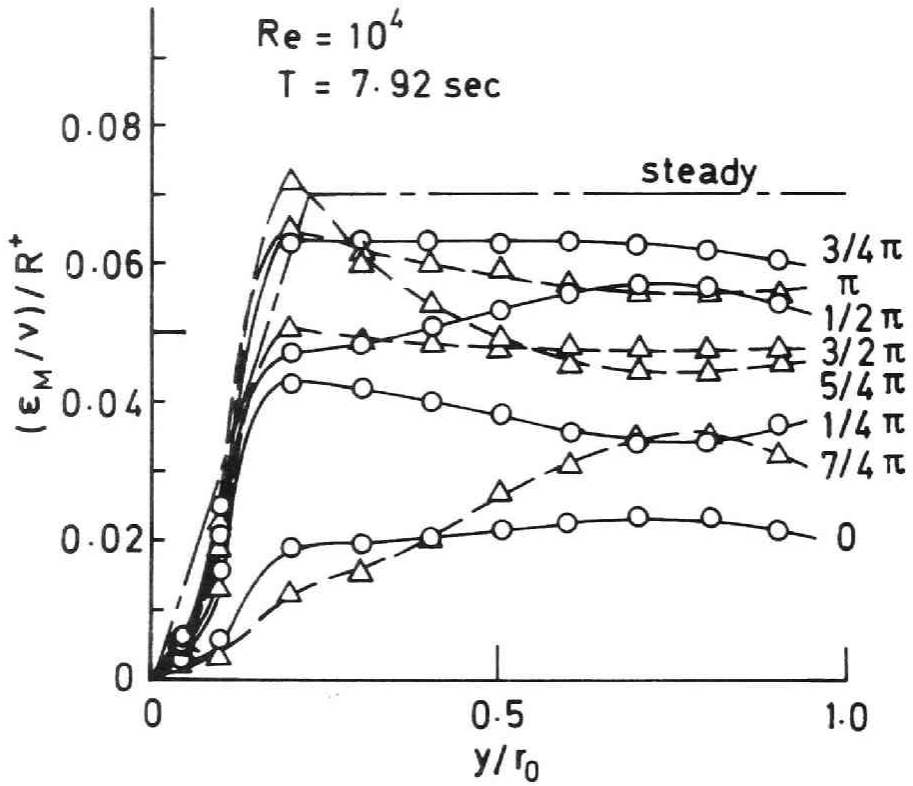


Fig. 4.8. Eddy viscosity profiles in pulsating flow ($T > T_c$).

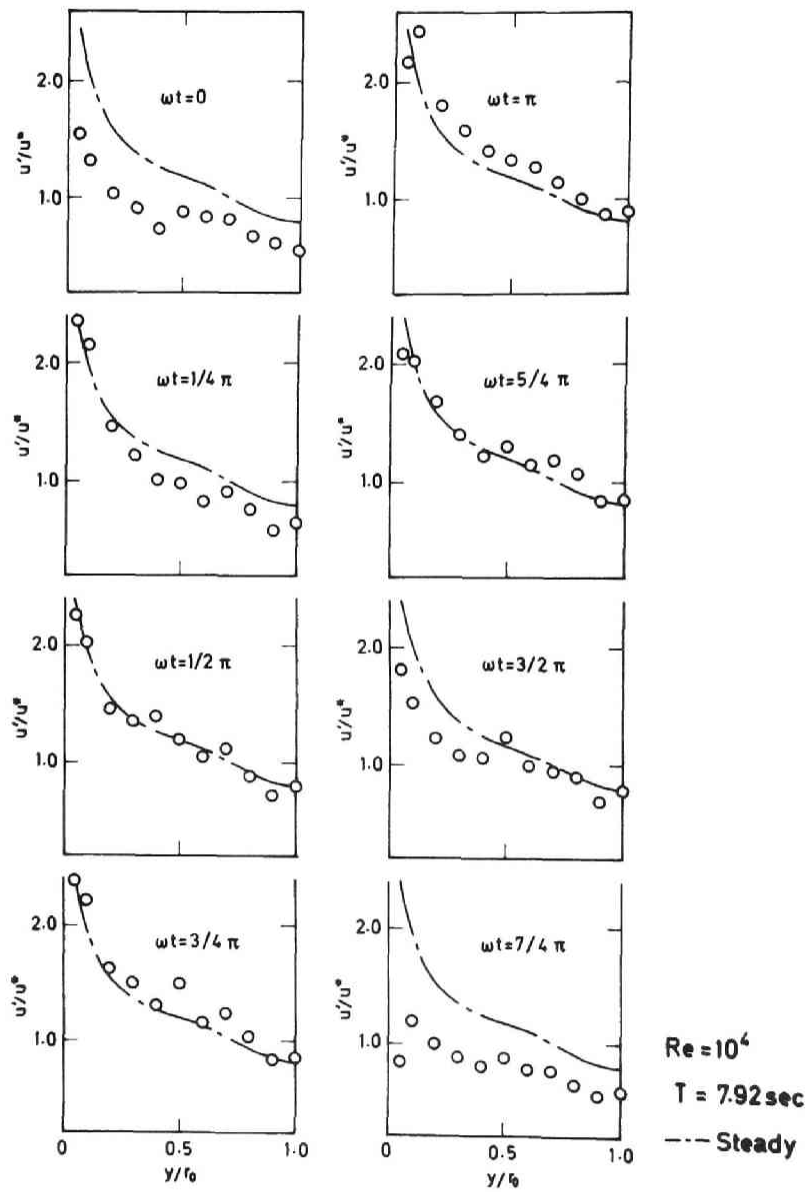


Fig. 4.9. Profiles of intensity of turbulence in pulsating flow ($T > T_C$).

really reach its equilibrium, and the structure of turbulence is not affected remarkably by the pulsation.

4.3.4 Profiles II ($T < T_C$)

The velocity profiles in pulsating flow shown in Fig. 4.10 are different both from those shown in Fig. 4.5 and from the profiles for steady flow. They are smooth in the acceleration period but they show the velocity defect and the decrease of velocity gradient near the wall in the deceleration period.

The profiles of shear stress and Reynolds stress shown in Figs. 4.11 and 4.12 also differ from the steady-state ones and those shown in Figs. 4.6 and 4.7, respectively. Different trends are obvious in the acceleration and in the deceleration period. The shear stress and the Reynolds stress take large negative values during a considerable time interval. This was confirmed by the measurement of wall shear stress using a probe mounted flush with the wall. In the flow section where the velocities could be measured with a probe, they do not take negative values, as a reverse flow occurs only very near the wall.

Since the Reynolds stress takes negative values, while the velocity gradient is positive, the eddy viscosity profile shown in Fig. 4.13 include negative values. Therefore one cannot apply the simple eddy viscosity model to the case of Profiles II.

Figure 4.14 shows the profiles of intensity of turbulence. They also change around the steady-state curve, and rise considerably in the zone $3\pi/4 < \omega t < 3\pi/2$ but not elsewhere. Gerrard [5] observed the similar

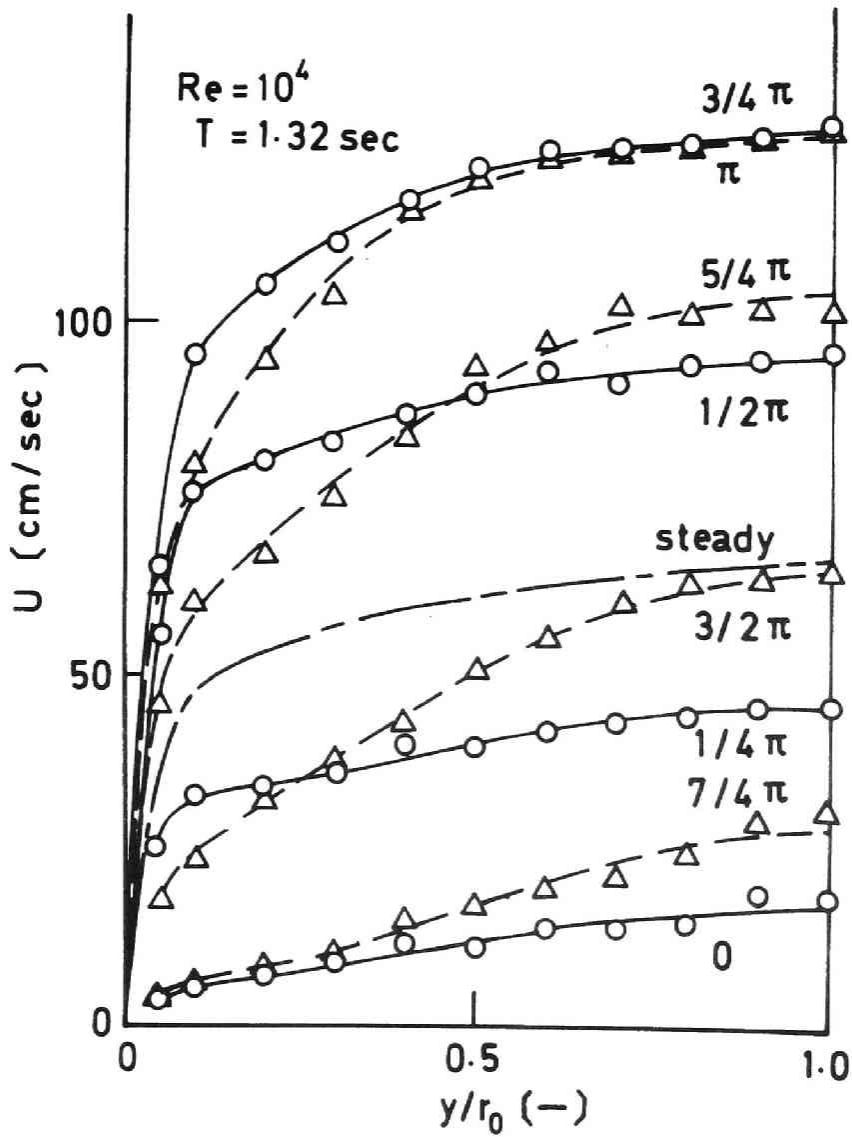


Fig. 4.10. Velocity profiles in pulsating flow ($T < T_c$).

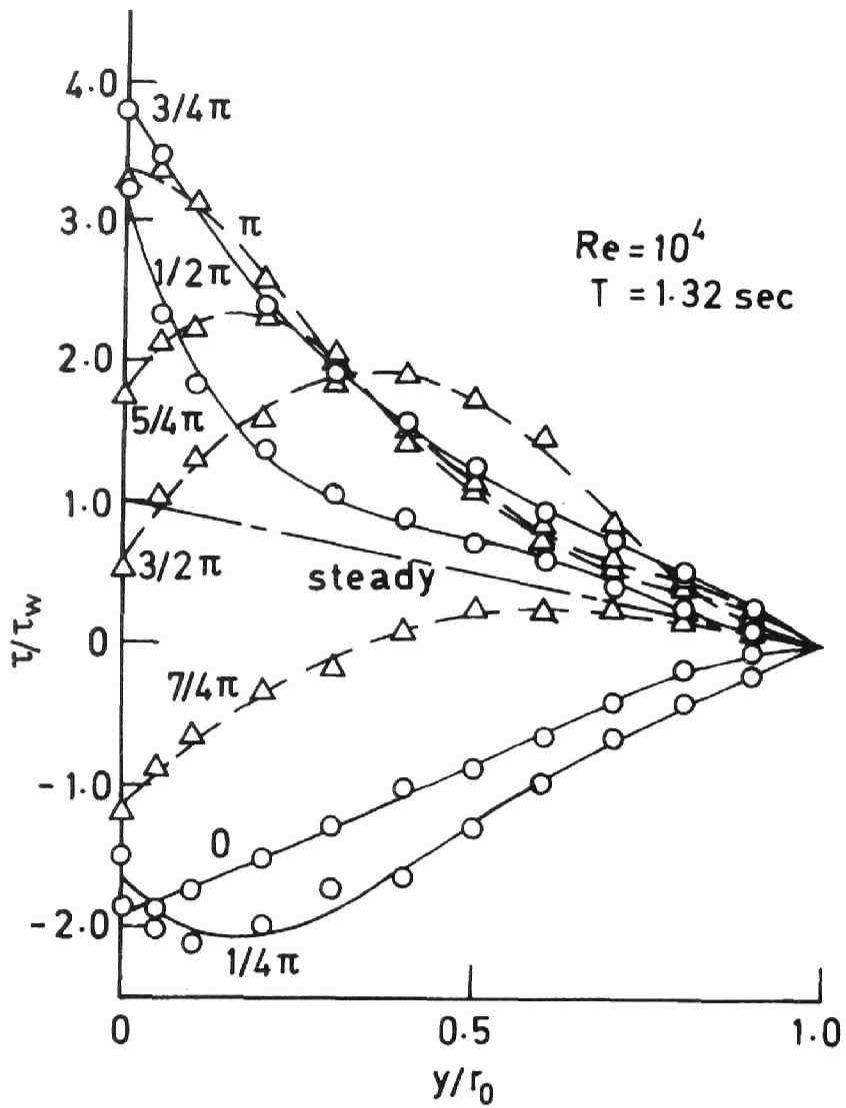


Fig. 4.11. Shear stress profiles in pulsating flow ($T < T_c$).

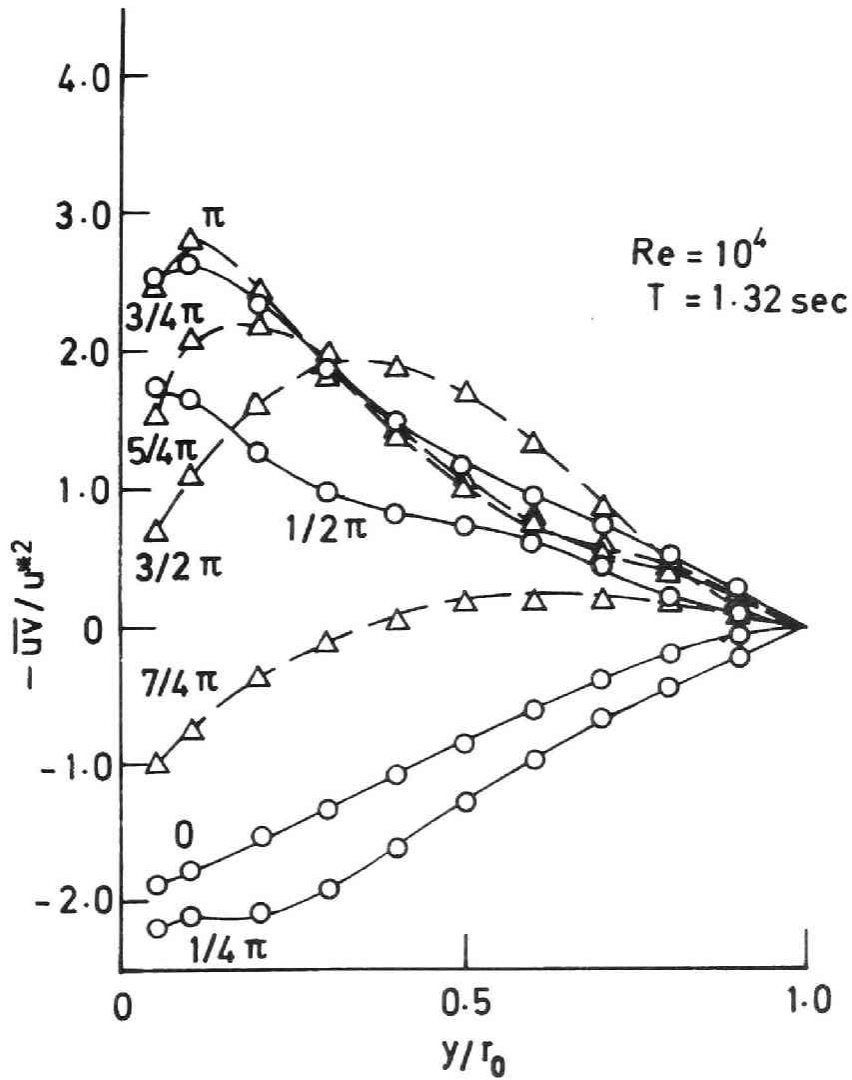


Fig. 4.12. Reynolds stress profiles in pulsating flow ($T < T_c$).

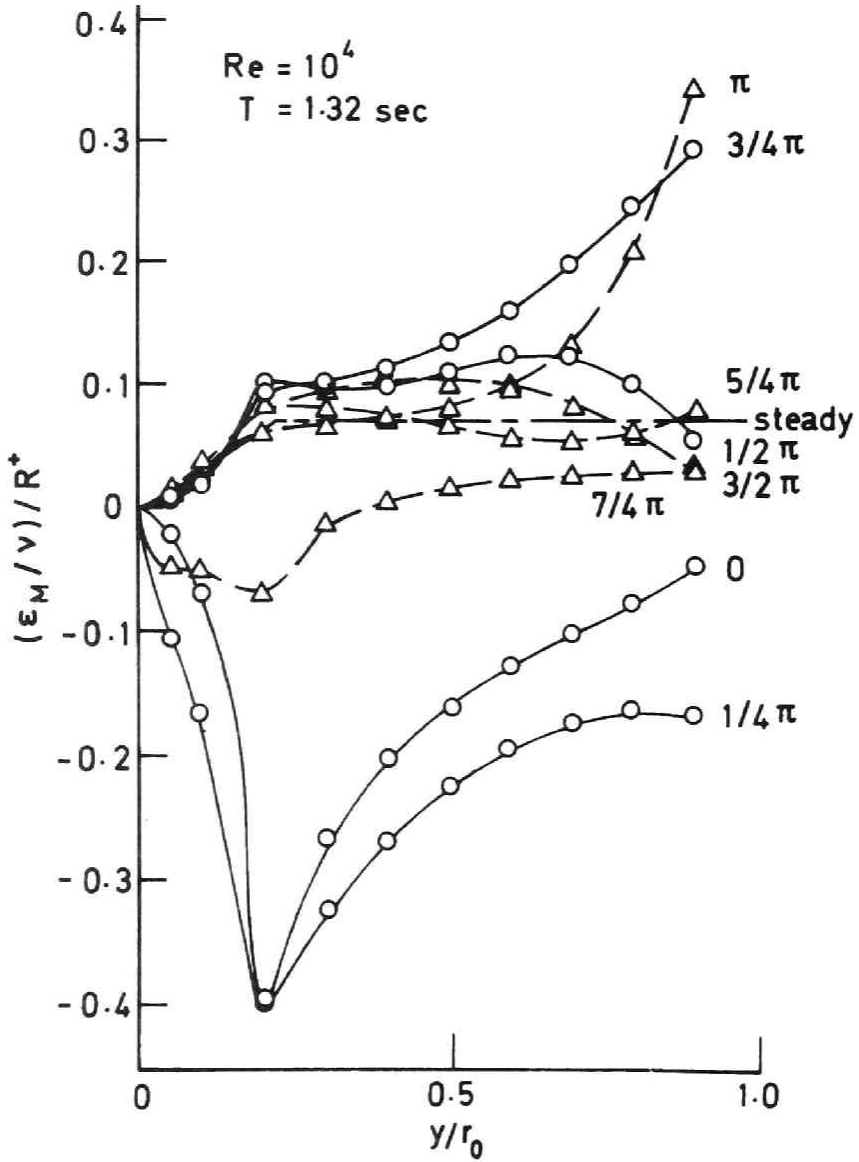


Fig. 4.13. Eddy viscosity profiles in pulsating flow ($T < T_c$).

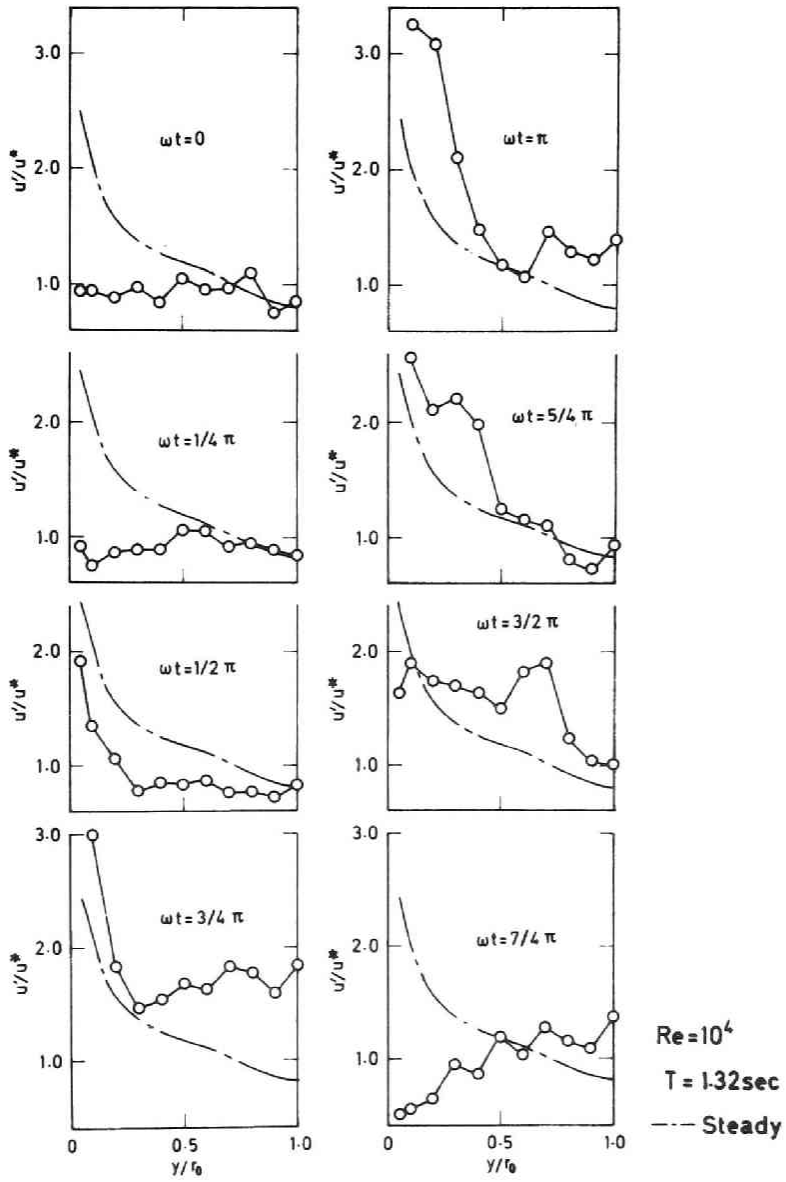


Fig. 4.14. Profiles of intensity of turbulence in pulsating flow ($T < T_c$).

variation of turbulent fluctuation, so his experiment was apparently done within the same region.

According to the results of Profiles II, there obviously is a fundamental change in the structure of turbulence: Profiles II show many similarities to the profiles of velocity and turbulence intensity of steady turbulent flow during the bursting.

Detailed studies of the bursting phenomena have been made by Kline *et al.* [8] in a turbulent boundary-layer flow. They pointed out that the production of turbulence occurred essentially during bursting times in the zone $0 < y^+ < 100$, and showed the profiles of turbulence intensity during bursting and non-bursting periods, which were similar to those at $\omega t = \pi$ and at $\omega t = 0$ in Fig. 4. 14, respectively. If we take into account simultaneously the above-mentioned facts and the facts of local acceleration and deceleration of fluid described by Corino and Brodkey [3] for steady turbulent flow, we can say that there are similarities between the bursting process (changing the instantaneous velocity and the intensity of its fluctuation) and the behaviour of the flow represented by Profiles II.

Moreover, Kline *et al.* [8] suggested that the bursting had a definite 'preferred range of period of occurrence'. By paying attention also to the relation between the pulsation and the burst period, a quantitative study for tube flow will be made as described below.

4.3.5 Time between bursts in steady flow T_B

Since detailed measurements of T_B in steady turbulent tube flow have not been reported, such measurements were

made, prior to measurements in pulsating flow.

As shown in Fig. 4. 15, the value of T_B were measured by the delay time of the location of the maximum in the autocorrelation curve of velocity fluctuations. Many studies using an autocorrelation have been made assuming that all the information is included between $R_{uu} = 1$ and $R_{uu} = 0$; however this is not so. Kline *et al.* [8] have shown that the mean value of T_B obtained by the visualization method agreed well with the delay time required to obtain the second mild maximum of autocorrelation functions of longitudinal velocity fluctuations in the viscous layer.

Figure 4. 16 shows a histogram of T_B from 100 measurements which were obtained while keeping the time constant of the averaging circuit of the correlator at its minimum. The value of T_B are largely spread around the mean value, and they nearly obey a log-normal distribution proposed by Rao *et al.* [17] according to measurements in a turbulent boundary-layer flow. The following mean value of T_B are the results obtained while keeping the time constant of the averaging circuit of the correlator at its maximum.

According to the studies by Kline *et al.* [8] it has been assumed that $\overline{T_B}$ does not change, at least in the zone of $0 < y^+ < 100$. This was checked and is shown in Fig. 4. 17. Within the Reynolds number range of accomplished measurements, a peak value of autocorrelation at constant delay time $\overline{T_B}$ clearly appeared in the region between the wall and about $y^+ = 100$ —200. However, the upper limit of y^+ depends on Reynolds number, this dependency was not determined precisely.

All available measurements of $\overline{T_B}$ shown in Fig. 4. 18

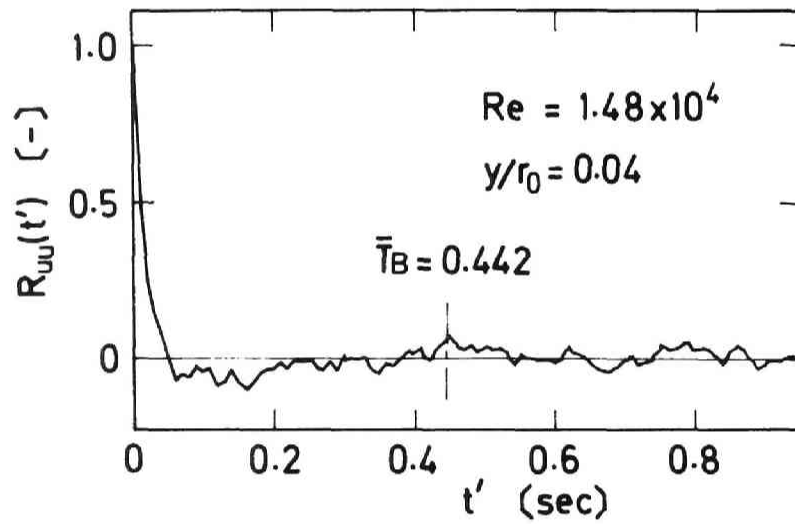


Fig. 4.15. Relation between \bar{T}_B and autocorrelation coefficient.

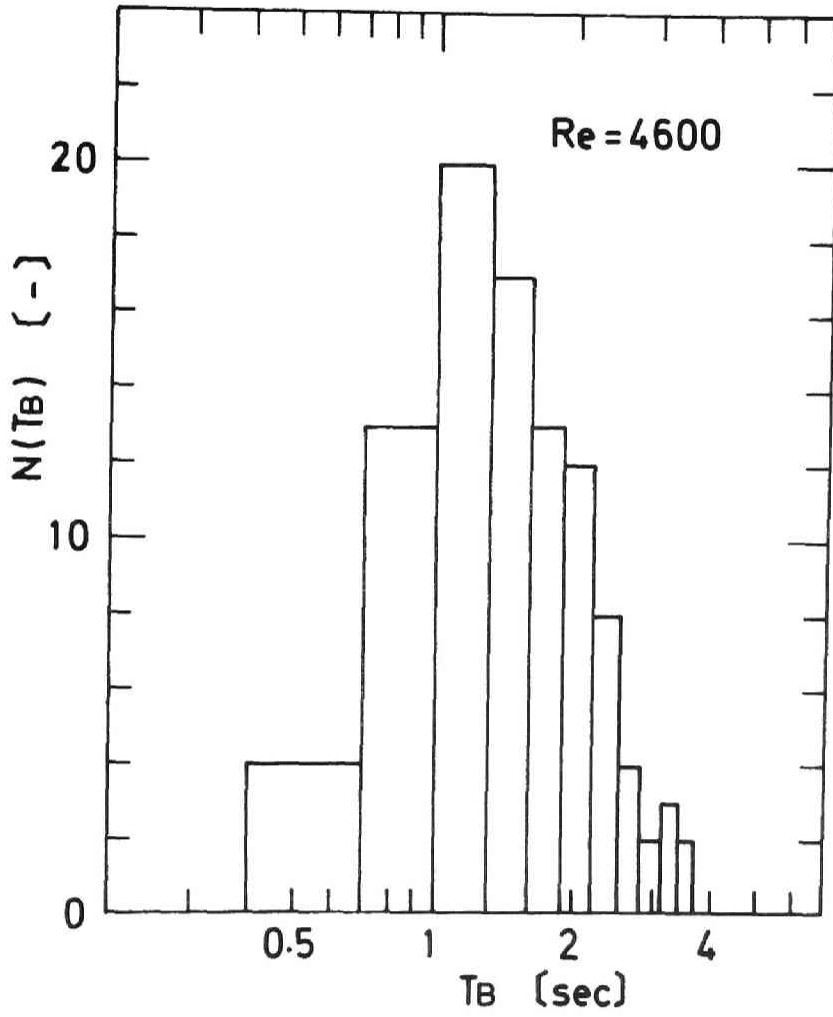


Fig. 4.16. Histogram of time between bursts.

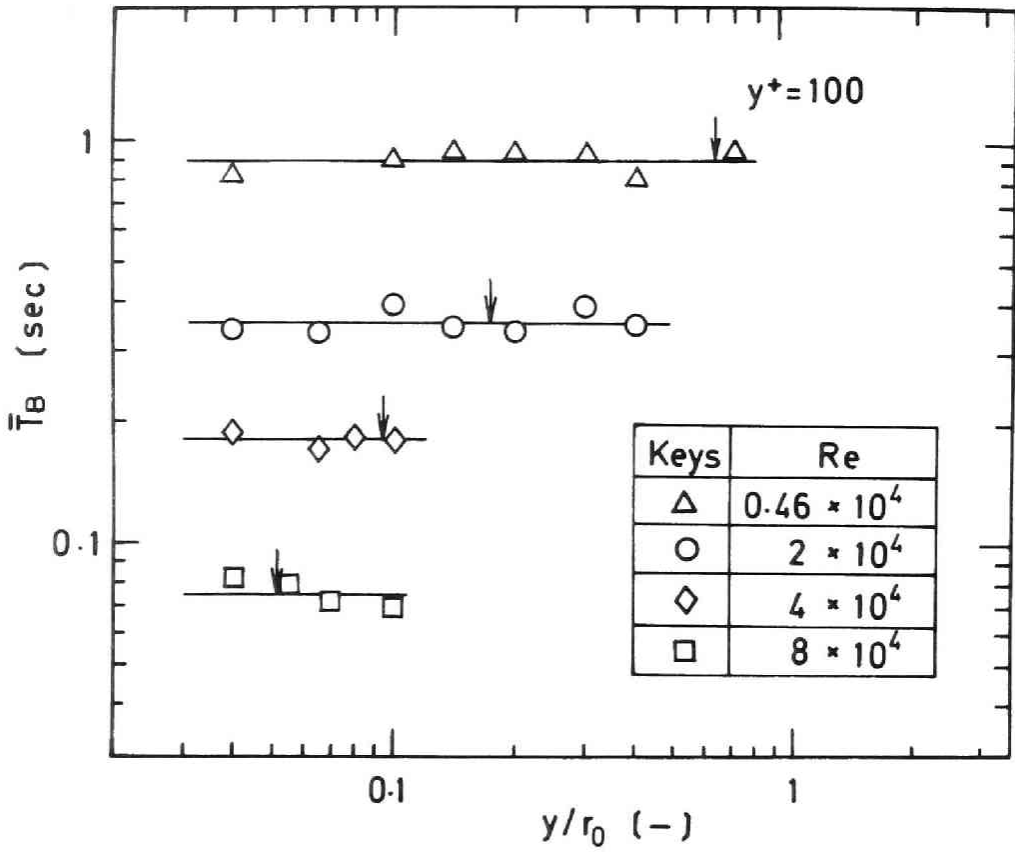


Fig. 4.17. Radial distribution of \bar{T}_B .

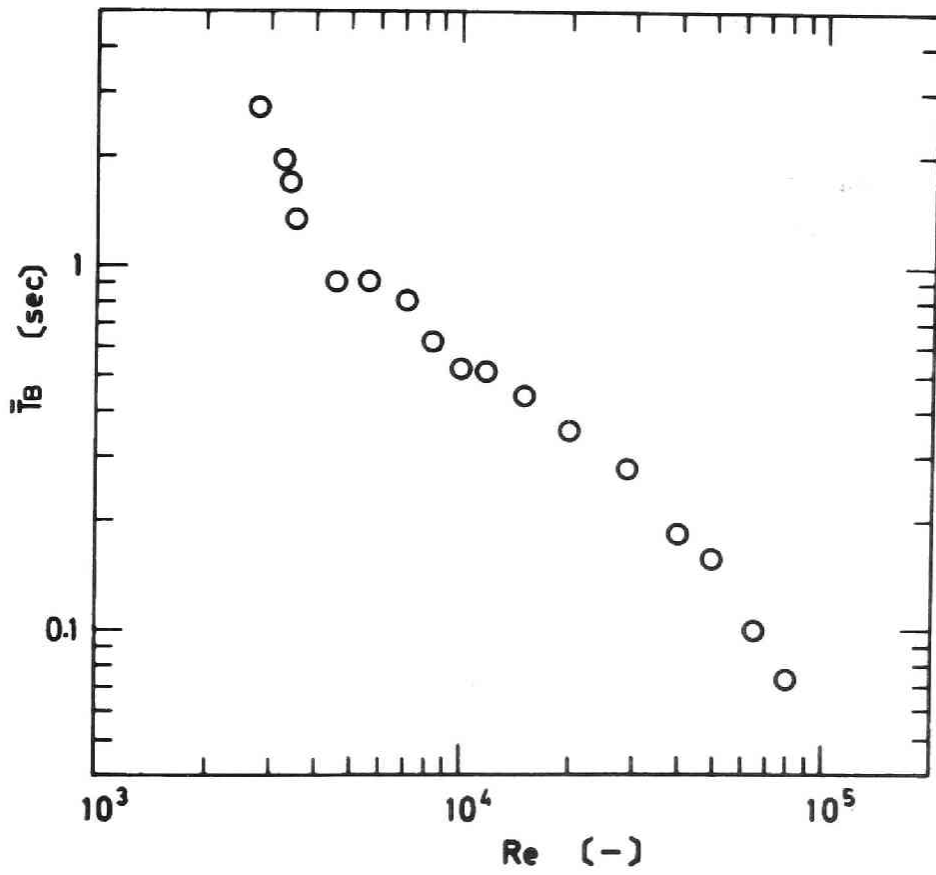


Fig. 4.18. \bar{T}_B as a function of Reynolds number.

were converted into dimensionless terms by using the bulk parameters U and D ; the results $\overline{T_B} \langle U \rangle / D$ are shown in Fig. 4. 19. From Fig. 4. 19 it can be said that the bursting repeats at a distance from 10 to 20 times the diameter D if the fluid is convected with the mean velocity $\langle U \rangle$, although this scaling shows some Reynolds number dependency.

4.3.6 Time between bursts in pulsating flow $\overline{T_{B_p}}$

In the same manner as in the measurements in steady-state flow, $\overline{T_B}$ was measured in pulsating flow. First, as shown in Fig. 4. 20, its constancy within a limited region from the wall was confirmed.

Figure 4. 21 shows $\overline{T_{B_p}}$ plotted against T . At large value of T , the values of $\overline{T_{B_p}}$ are constant and agree well with $\overline{T_B}$ shown by a rigid line. The smallest value of T in such a region is called the critical period T_C . In the region of $T > T_C$, pulsation does not affect the mean value of the burst period, so the turbulence can be considered as being unchanged, as mentioned before.

Next we will discuss the other region, i.e. $T < T_C$. As shown by a broken line in Fig. 4. 21, the delay time $\overline{T_{B_p}}$ determined by the maximum value of the autocorrelation agreed well with the pulsation period. However, from this result alone, it cannot be said that the value of $\overline{T_{B_p}}$ is equal to T , because the pulsating component itself might show this maximum.

Therefore, to confirm that $\overline{T_{B_p}} = T$ in this region, the cross-correlation coefficient between the fluctuating component and the pulsating component was measured. As a result, where T is greater than T_C , the cross-correlation does not exist, i.e. it is zero at any delay time,

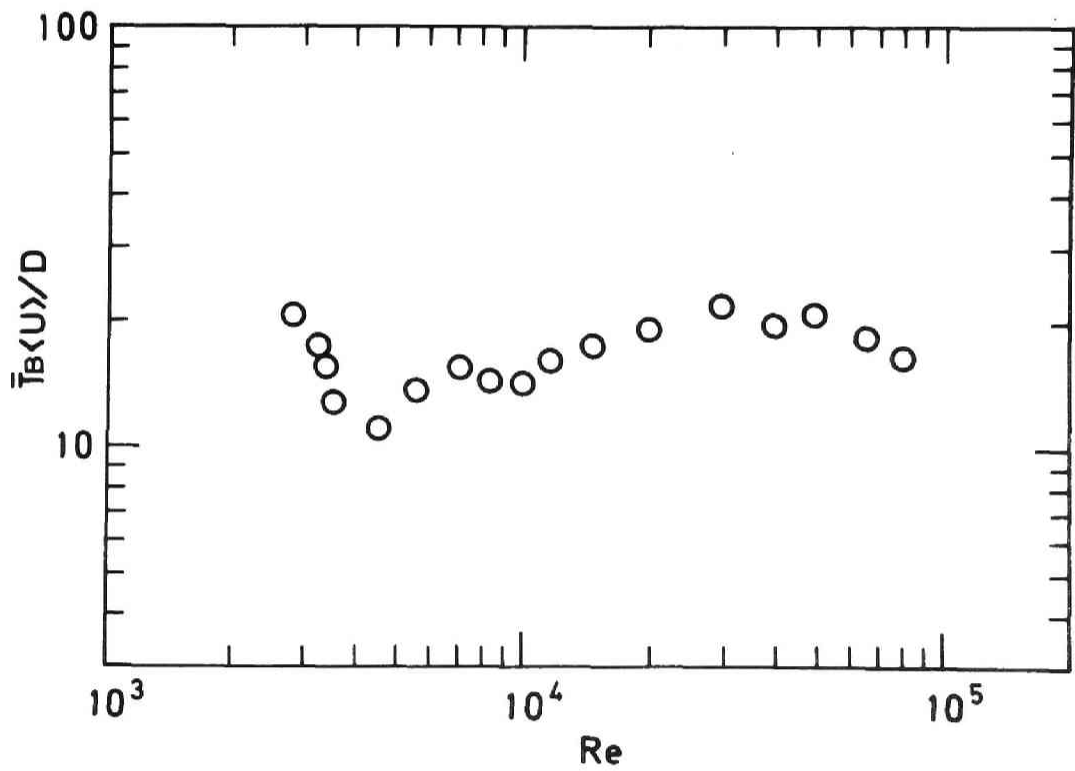


Fig. 4.19. Normalized \bar{T}_B as a function of Reynolds number.

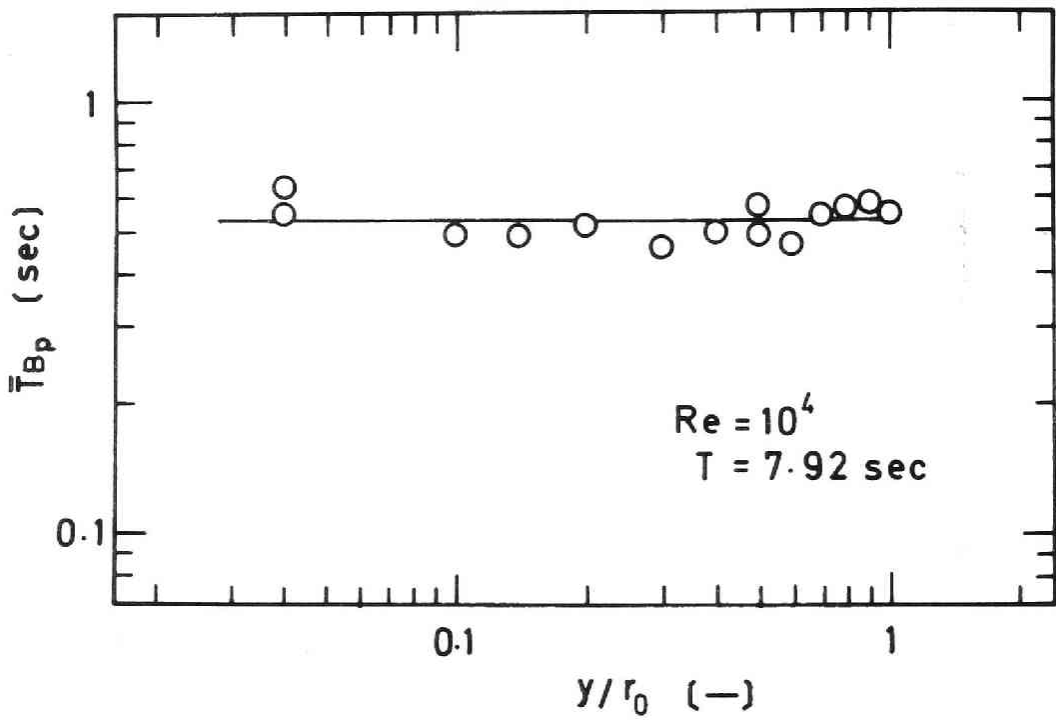


Fig. 4.20. Radial distribution of \bar{T}_B in pulsating flow.

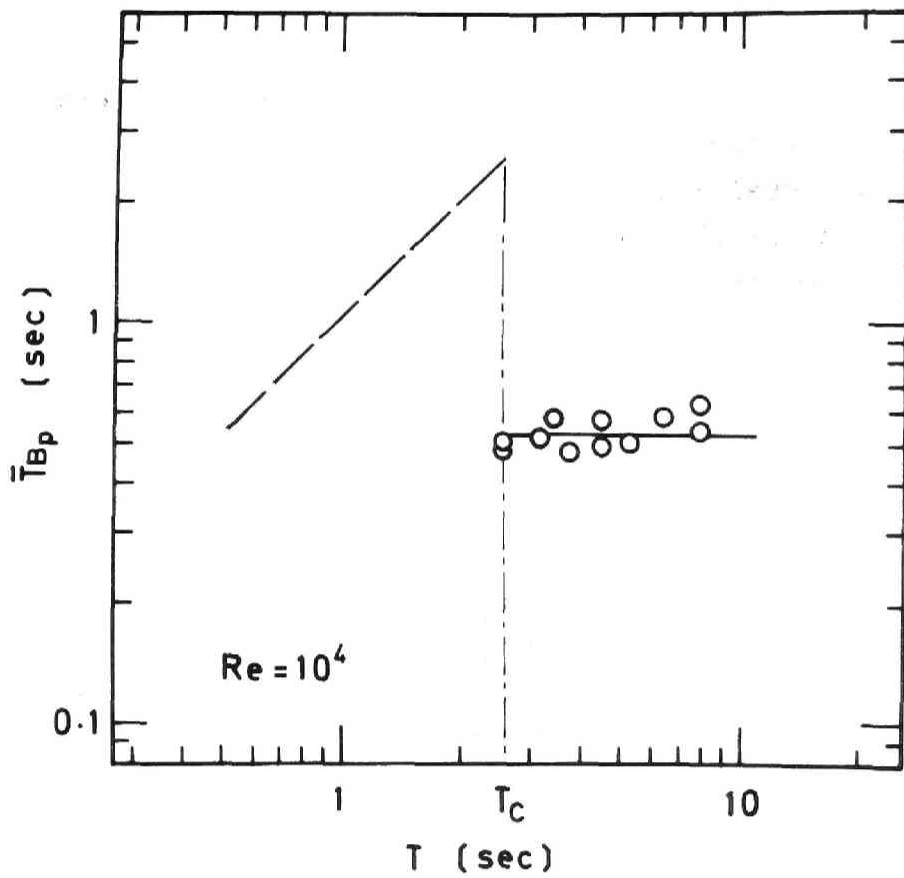


Fig. 4.21. \bar{T}_{Bp} as a function of pulsation period.

but where T is less than T_c , the cross-correlation is generally not equal to zero, obviously because of the same periodicity.

Figure 4. 22 shows that the maximum correlations are independent of the cut-off frequency of n of the high-pass filter, if n has a value above 50.

Figure 4. 23 shows the maximum correlation $R_{UU}(T)$ plotted against T . From the facts mentioned above it can be concluded that if T is less than T_c , the value of $\overline{T_{Bp}}$ is equal to T ; that is a resonance (note that this resonance is not the 'reconance' in heat transfer!) occurs between the pulsation and the bursting. Accordingly, as shown in Figs. 4. 10 and 4. 14 the velocity and turbulent fluctuation pulsate in a manner similar to the bursting in steady-state flow.

Moreover, a comparison of Fig. 4. 23 with Fig. 4. 16 shows that T_c agrees with the maximum time between bursts of steady-state flow. So, the region where $\overline{T_{Bp}} = T$ is the region where T_B exists, i.e., the preferred range of the burst period of steady-state flow.

From the results of bursting in pulsating flow, it becomes clear that the preferred range of burst periods is not changed by the flow pulsation and that it also controls the pulsating turbulent flow. That is, when the pulsation period is higher than the upper limit of this range, the mean burst period is equal to that of steady-state flow, but when the pulsation period is included in the region, the resonance occurs, i.e., bursting of the same period as the pulsation period dominates.

4.3.7 Classification of pulsating turbulent flow

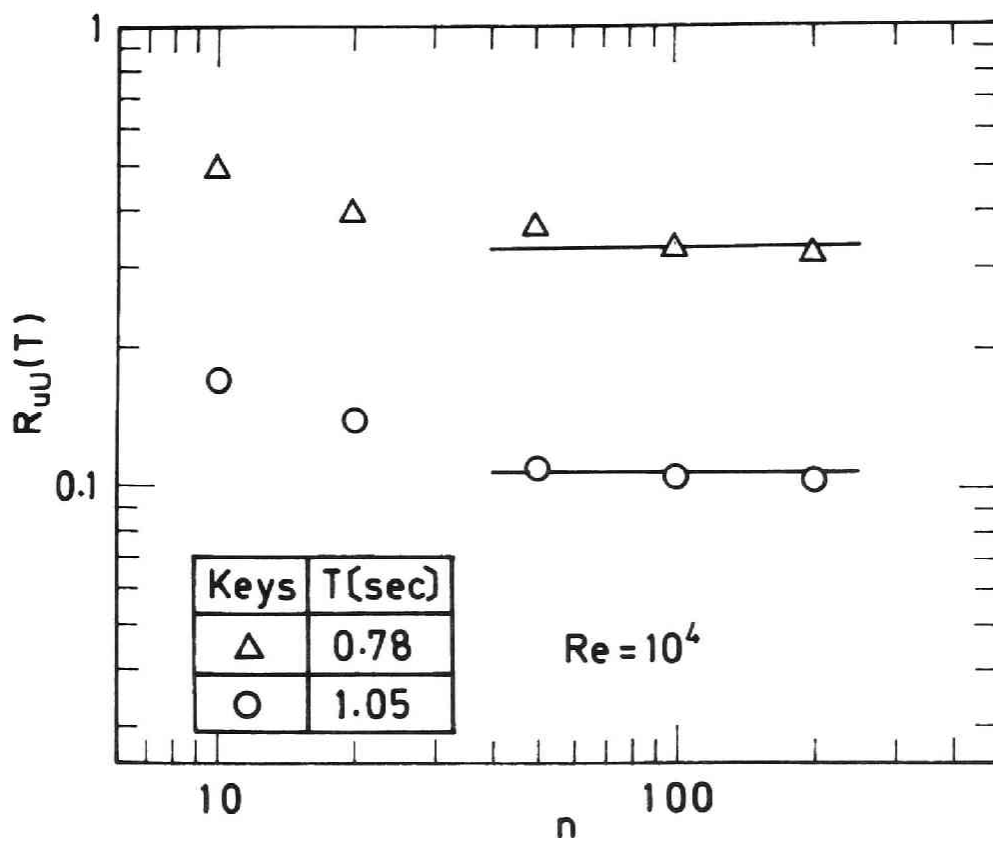


Fig. 4.22. Effect of filter cut-off frequency on determined value of $R_{uU}(T)$.

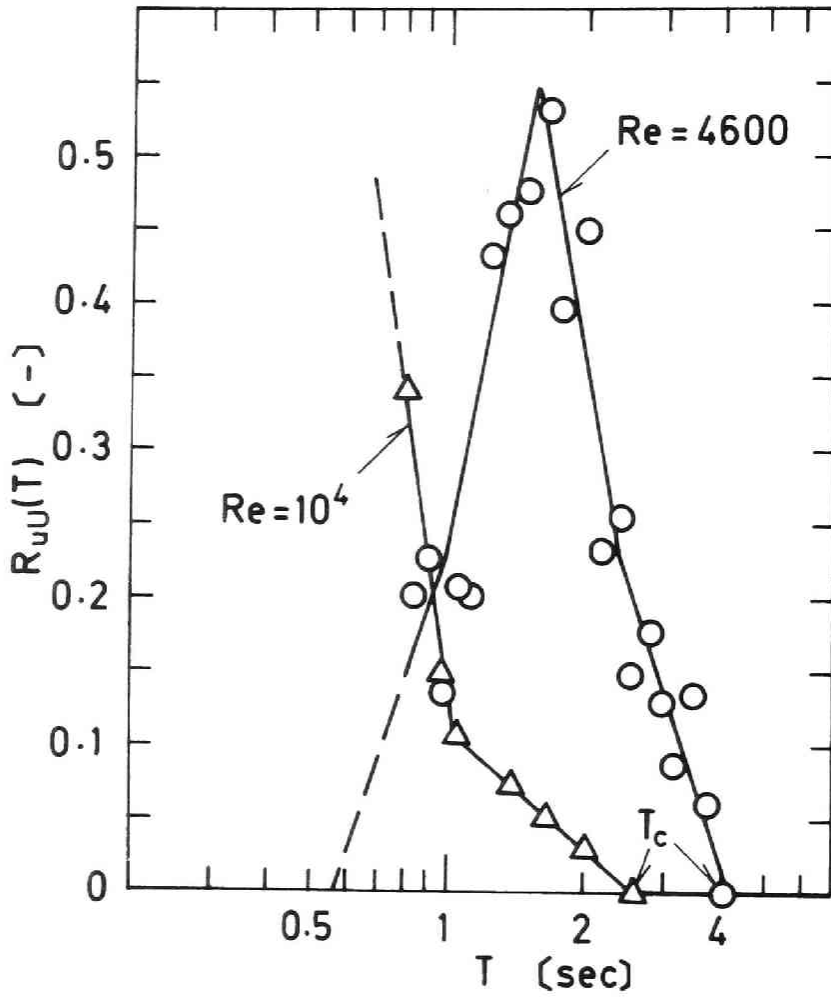


Fig. 4.23. $R_{uu}(T)$ as a function of pulsation period.

Figure 4. 24 shows T_c (together with $\overline{T_B}$ and the later mentioned T_q) plotted against the Reynolds number. The value of T_c , which is obtained from the correlations mentioned above, seems to be coincident with $\overline{T_B}$ at $Re = 2300$, but this is not so at other Reynolds number. The dependency of T_c on Re seems to be very complex, maybe even stepwise, but, as a rough approximation, the relation may be written as

$$\frac{T_c \langle U \rangle}{D} \approx 0.19 Re^{2/3} \quad (2300 < Re < 10^5) \quad (4.4)$$

Using the $T_c \langle U \rangle / D$ versus Re curve, we may classify the pulsating turbulent flow over a wide range of Reynolds number: the critical period of pulsation T_c separates the range of Profiles I from the range of Profiles II. The range of Profiles II including the profiles of Gerrard [5] lies below the T_c curve and the range of Profiles I lies above the T_c curve. The observation by Gerrard was made at a very large pulsation period ($T = 12.19$ sec) but the dimensionless term fits in the range of Profiles II.

Finally, the upper and lower limits of both regions (Profiles I and II) will be described. It is reasonable to expect that at a large value of T there exists a region where $\overline{T_{B_p}}$ changes smoothly with the pulsation, and that the structure of turbulence changes according to the turbulence structure of steady flow at a corresponding value of velocity. Such a state is a pseudo-steady state, where the amplitude ratio of flow rate is close to unity. The dotted line for T_q in Fig. 4. 24 is obtained from the analysis in Section 2.3.3 so as that the amplitude ratio is equal to 0.95. The upper limit

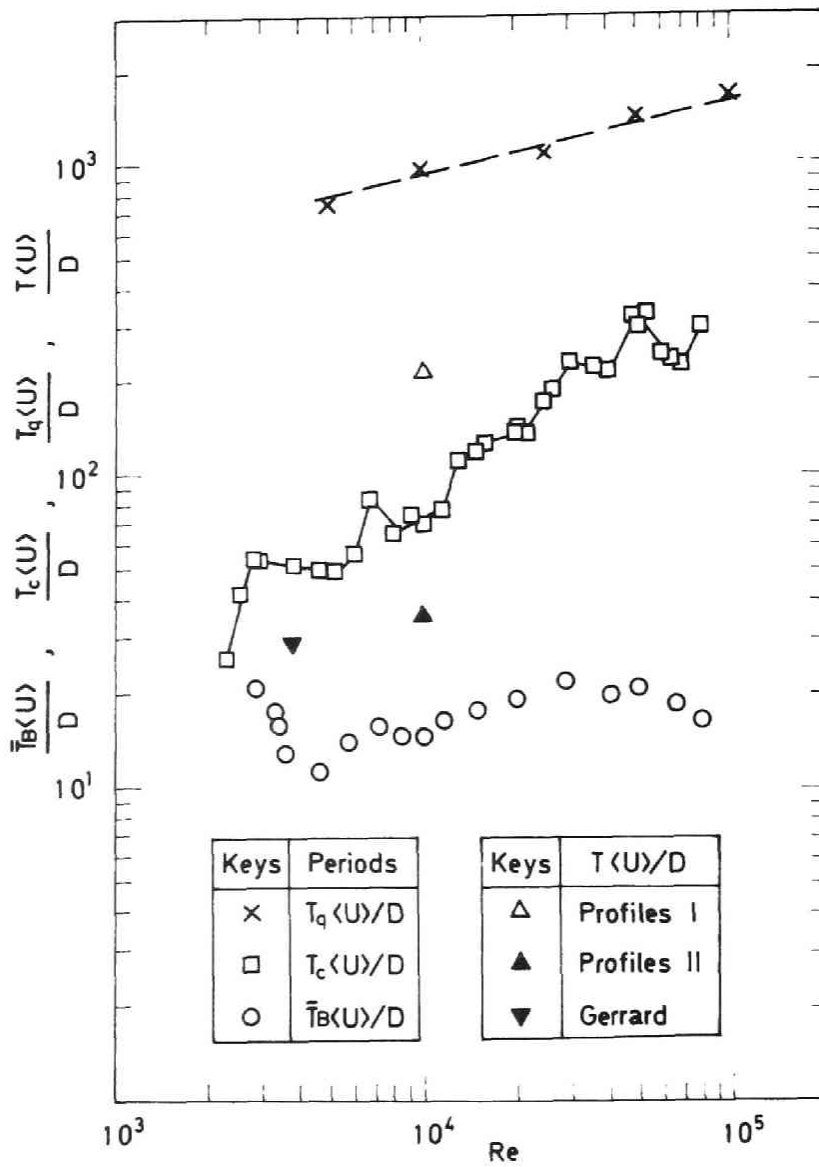


Fig. 4.24. Normalized T_c , \bar{T}_B and T_q as functions of Reynolds number.

may be estimated to exist near this line.

The lower limit may be the smallest value of T_B , below which it is assumed that the pulsation does not affect the bursting but interacts with the turbulent fluctuation and distort it directly. The smallest value of T_B may be estimated from $\overline{T_B}$, $\overline{T_C}$ and the log-normal distribution.

4.4 Conclusion

1. The time between bursts of steady turbulent flow in a tube was determined in a satisfactory way.
2. The preferred range of burst periods of steady flow control the bursting phenomena in pulsating turbulent flow.
3. By means of the critical pulsation period T_C , which is equal to the maximum time between bursts, two types of behaviour of pulsating turbulent flow can be distinguished.
4. If the pulsation period T is longer than the critical pulsation period T_C , the pulsation does not affect the mean time between bursts, so the turbulence intensity does not pulsate and the velocity pulsates smoothly.
5. If T is shorter than T_C , the resonance occurs, i.e., the bursting of the same period as that of pulsation dominates, so the velocity and turbulent fluctuation pulsate in a manner similar to those in the bursting phenomenon of steady flow.

CHAPTER 5

DYNAMIC PROCESS OF BURSTING IN PULSATING TURBULENT FLOW

5.1 Introduction

In this chapter, the dynamic process of bursting is studied experimentally.

As shown in Section 4.3.5, the occurrence of the bursting has a well-defined mean frequency which scales on the bulk parameters rather than the wall parameters. While, according to Kline *et al.* [8], the time period of the observed bursting process near the wall is only a part of the whole burst period and the process from the last stage, so called 'breakup' to the first stage of the next bursting has not been clarified. Therefore, a sequence of events subsequent to the breakup is imagined to occur in the core region. However, it seems very difficult to make clear the entire cycle of bursting in steady turbulent flow, because the generation of turbulence near the wall occurs randomly in space and time.

On the other hand, as was clarified in Section 4.3.6, the bursting phenomenon in the pulsating flow shows the same periodicity as the pulsation period, i.e. the resonance occurs, if the pulsation period is within a preferred range of burst period. It is expected that the detailed study of spatial and temporal relation between events in resonant pulsating flow will show the entire cycle of events of bursting phenomenon. Thus

the study in the resonant pulsating flow is worthwhile.

First, under constant Reynolds number ($Re = 10^4$) some characteristics of resonance were examined in the whole range of burst period. Next, the turbulence generation and its propagation to radial direction were made clear by using a correlation function. Especially, detailed studies were made for the propagation process and its time period. Finally, a relation between the burst period and the propagation time was discussed.

5.2 Test Section and Measuring Equipment

In the present work, the same test section and fluid as those mentioned in Section 4.2 were used for the bulk of measurements. For short pulsation period $T < \overline{T_B}$, however, measurements were made in a tube of 5.16 cm inside diameter, at a position 78 diameters downstream from the entry.

The analog-to-digital conversion and data reduction were done with a hybrid computer using several assembly language programs. To avoid too long recording time and difficulty to adjust an external clock to the pulsation period, the electrical signals of velocity and time pulse were directly connected to the analog input. The time pulse was generated by a photo-transistor at 32 phase angles per cycle according to the flow pulsation.

5.3 Results and Discussion

5.3.1 Region of burst period in steady flow

In order to confirm a flow being fully developed in the tube of 5.16 cm inside diameter, turbulence characteristics in steady flow were measured first. Figures 5. 1 and 5. 2 show the turbulence intensity profile and the mean burst period $\overline{T_B}$, respectively. The mean burst period was determined from the delay time required to obtain the second mild maximum in the curve of the autocorrelation coefficient. They are sufficiently in good agreement with the measurements in the 2 cm I.D. circular tube.

The minimum burst period $T_{B_{\min}}$ is also shown in Fig. 5. 2, which was obtained by the same method as that used in Section 4.3.5. As was pointed out in Section 4.3.7, the value of $T_{B_{\min}}$ is nearly symmetric to the maximum burst period T_C with respect to $\overline{T_B}$ on a log scale.

In the following sections, discussions will be made on the pulsating flow of pulsation period within the preferred region of burst period, i.e. $T_{B_{\min}} < T < T_C$.

5.3.2 Resonant pulsating flow

At various periods of pulsation ranging from $T_{B_{\min}}$ to $\overline{T_B}$ the velocity and the turbulence intensity profiles were measured in the circular tube of 5.16 cm inside diameter. The phase averaging were made at 32 phase angles within one cycle by using the instantaneous values of 100 pulsation cycles:

for velocity

$$U(t) = \frac{1}{N} \sum_{n=1}^N U_i(t + nT)$$

and for turbulence intensity

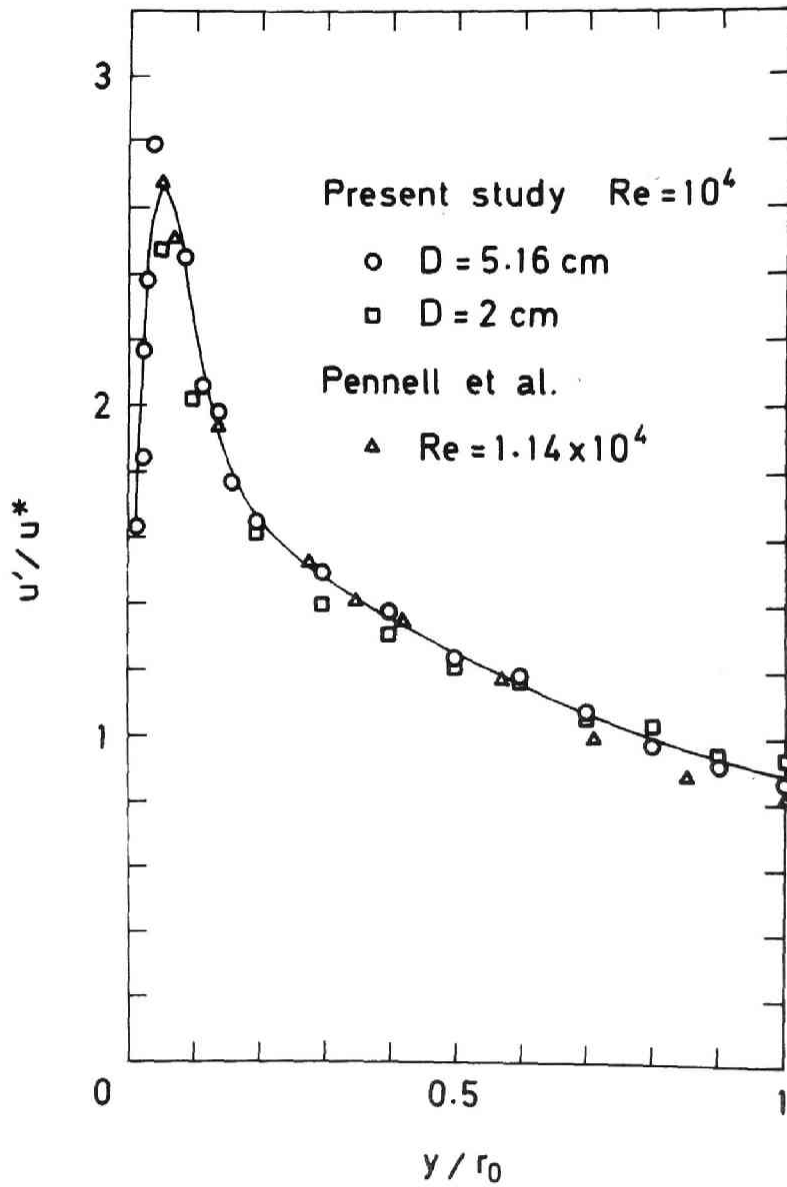


Fig. 5.1. Turbulence intensity profile in steady flow.

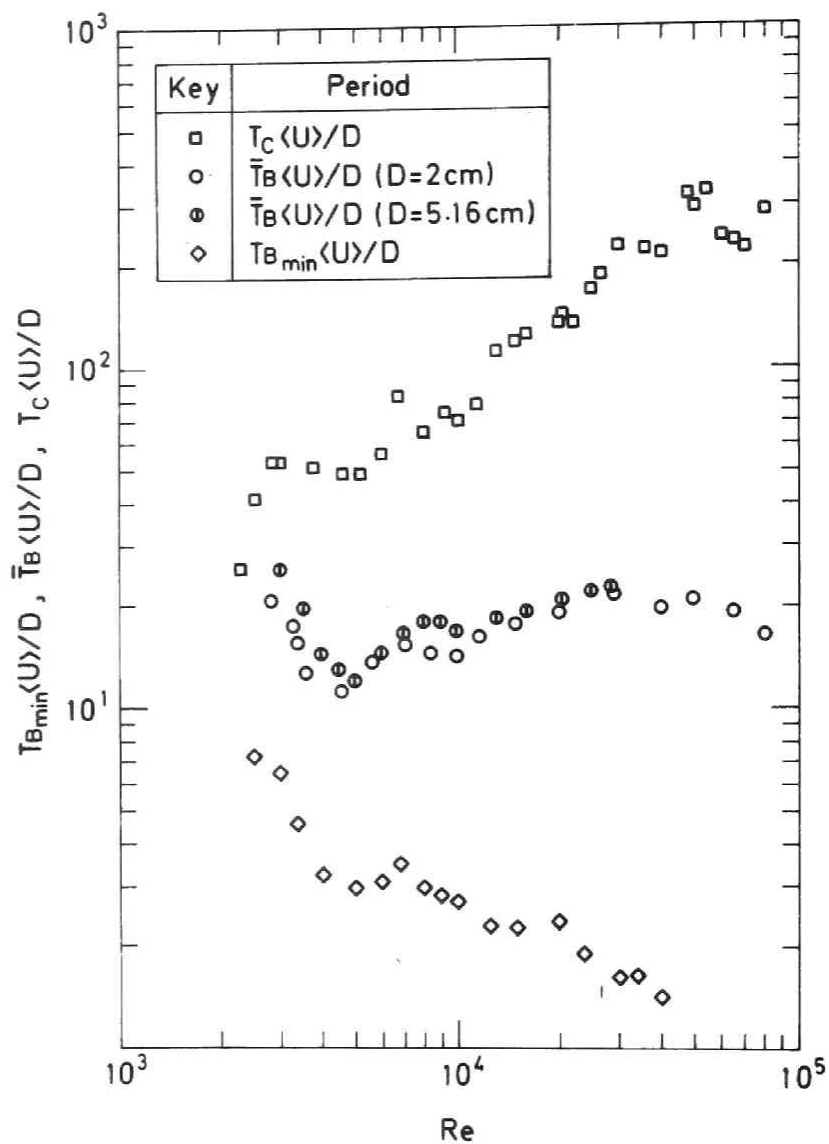


Fig. 5.2. T_C , \bar{T}_B and $T_{B_{min}}$ normalized with bulk parameters as functions of Reynolds number.

$$u'(t) = \sqrt{\frac{1}{N} \sum_{n=1}^N \{ U_i(t + nT) - U(t) \}^2} \quad (5.1)$$

where $N = 100$.

From the measurements, it was clarified that the resonance between pulsation and turbulence generation occurred in the whole region of $T_{B_{\min}} < T < T_C$. In addition, it was found that the characteristics of resonance which were pointed out in Section 4.3.4 became more obscure with decreasing pulsation period. These details will next be described.

Figure 5. 3 shows a typical set of velocity profiles. The parameter varied in this diagram is the phase angle ωt (started from the time when the flow rate had the minimum value). The velocity profiles in the pulsating flow are similar to those of the steady flow with an exception that the profiles near the wall are somewhat contorted in the acceleration period.

Figure 5. 4 shows normalized profiles of intensity of turbulence. The friction velocity u^* was determined in the steady-flow condition. Near the wall they vary around the profile of steady flow, and rise considerably at about $\omega t = \pi$. This violent change of intensity of turbulence is apparently caused by the resonance. In the core region of the tube, however, these profiles are different from Profiles II (see Section 4.3.4) and similar to those for steady flow.

The area in which this similarity persists expands to the wall continuously as pulsation period decreases from $\overline{T_B}$ to $T_{B_{\min}}$. Figure 5. 5 illustrates several examples of velocity signal at $y/r_0 = 0.05$. The periodicity of turbulent fluctuation appears distinctly at long

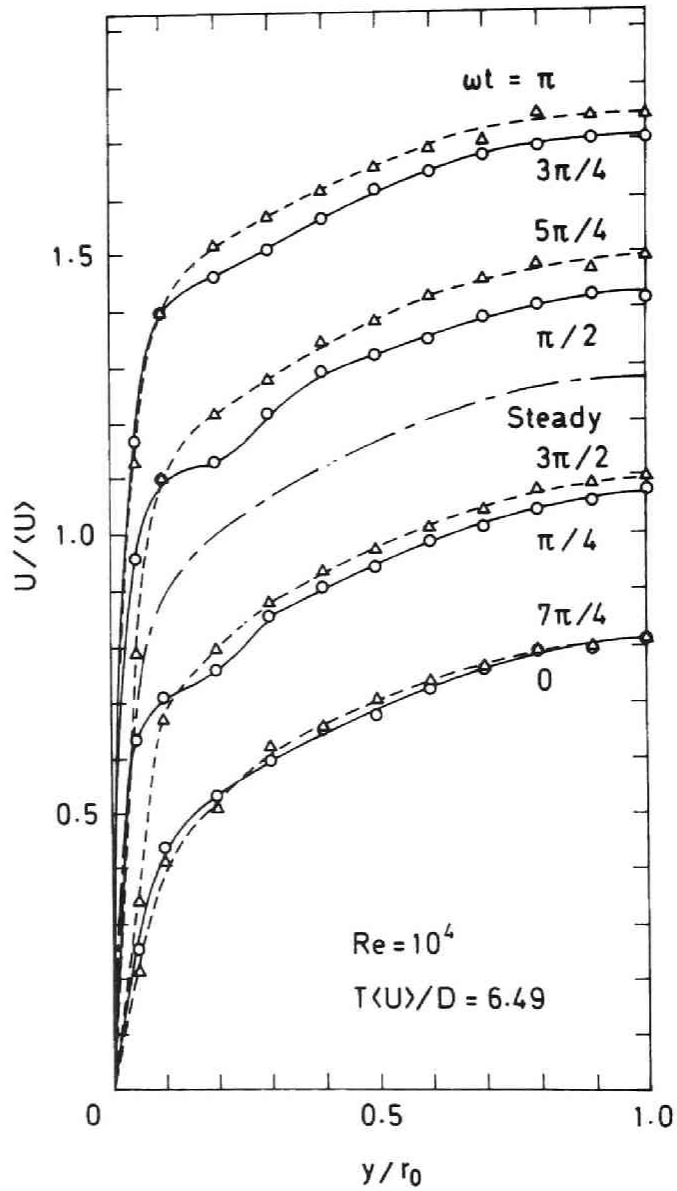


Fig. 5.3. Velocity profiles in pulsating flow.

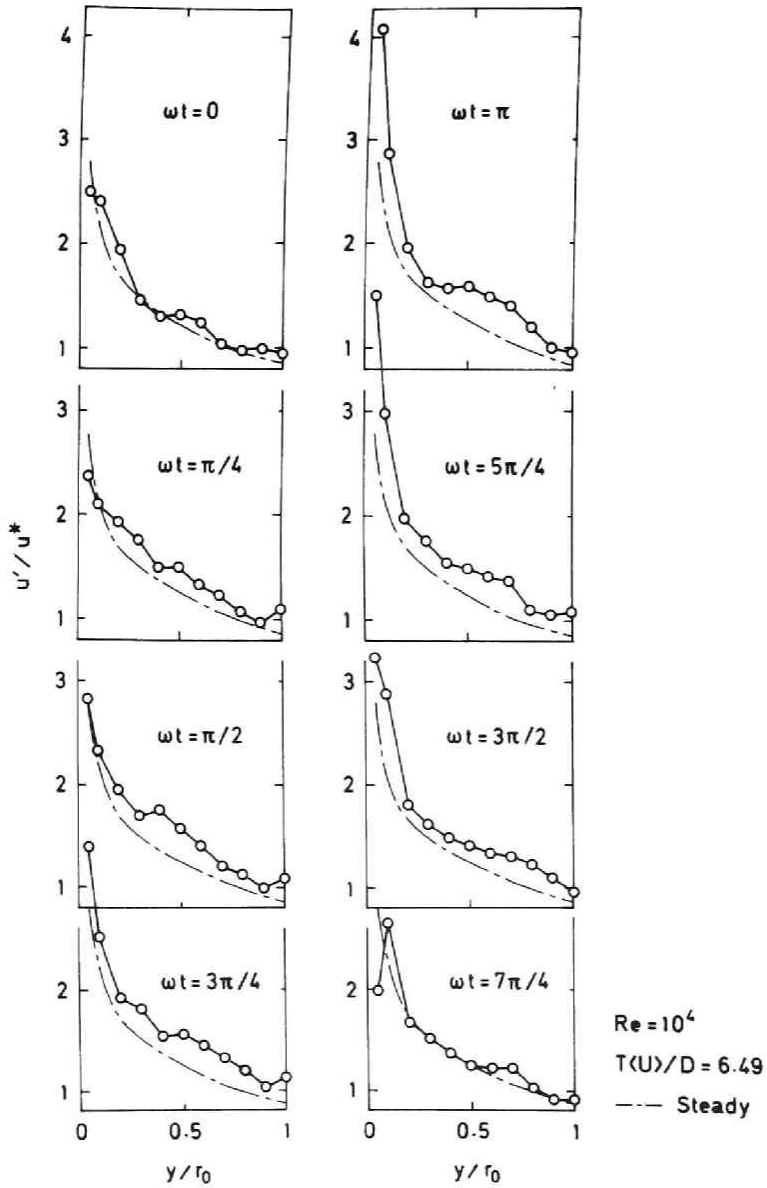


Fig. 5.4. Turbulence intensity profiles in pulsating flow.

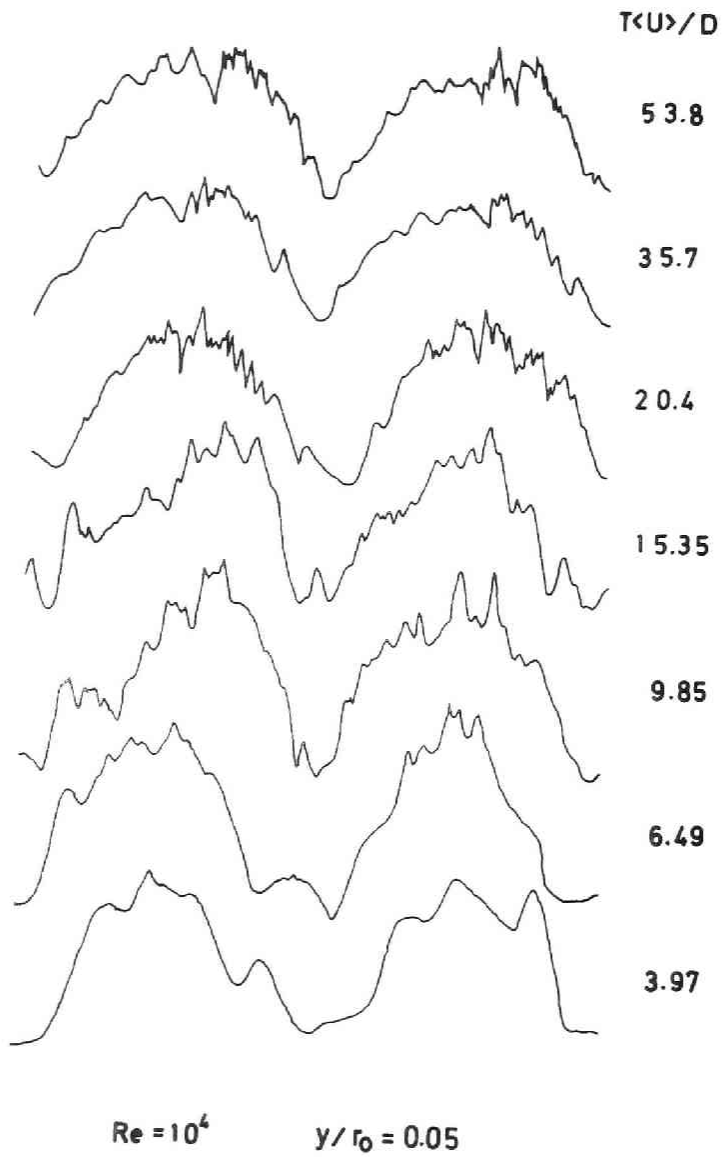


Fig. 5.5. Variations of velocity ($T_{B_{\min}} < T < T_C$).

pulsation period ($T\langle U \rangle/D \geq 20.4$) but it becomes obscure with decreasing pulsation period.

Above mentioned results strongly suggest that the pulsation affects only the generation of turbulence and that another factor controls the bursting process subsequent to the generation of turbulence. Detailed discussions will be made in the following section by using a correlation function measured in the region of $\overline{T_B} < T < T_C$, where the periodical change of turbulence is detectable at the core region of the tube.

5.3.3 Phase-averaged correlation coefficient

The correlation function for u , $R_{uu}(t, t')$ is defined by the equation

$$R_{uu}(t, t') = \frac{\overline{u(t) u(t + t')}}{\overline{u'(t) u'(t + t')}} \quad (5.2)$$

where t' is delay time and $u'(t)$ is not equal to $u'(t + t')$ with an exception when t' is equal to T , because the turbulence intensity varies with respect to phase. An overline in Eq. (5.2) means the phase average, so Eq. (5.2) is rewritten as

$$R_{uu}(t, t') = \frac{\sum_{n=1}^N u(t + nT) u(t + nT + t')}{\sqrt{\sum_{n=1}^N \{u(t + nT)\}^2 \sum_{n=1}^N \{u(t + nT + t')\}^2}} \quad (5.3)$$

where $N = 100$ and $-T/2 < t' < T/2$.

Measurements were conducted at $T\langle U \rangle/D = 20.4$ by using the 2 cm I.D. circular tube. Under this condition,

both profiles of velocity and turbulence intensity shown in Figs. 5. 6 and 5. 7 are similar to Profiles II.

Figure 5. 8 shows the correlation curves at $y/r_0 = 0.05$ or $y^+ = 15.7$, where the generation of turbulent energy near the wall is supposed to be detected. As can be seen, there occurs a periodical change of time scale: a large scale of turbulence decreases during the phase $0 < \omega t < \pi/2$ and increases slowly during $\pi/2 < \omega t < 2\pi$. Note that they are not always symmetric with respect to the axis of $t' = 0$, although an usual correlation curve in steady flow is assumed to be always symmetric, i.e. an even function of delay time. Especially, a distinct asymmetry at $\omega t = \pi/4$ indicates that the time period of scale change to the smaller one is very short in comparison with time scale of the turbulent fluctuation. This fact and nonexistence of corresponding reversed change in the cycle strongly suggest that the turbulence generates at $\omega t = \pi/4$.

Figure 5. 9 shows the energy spectra, which are obtained by using a Fourier transformation of the correlation function at $\omega t = \pi/4$. They correspond to the two region, i.e. $t' > 0$ and $t' < 0$, of the correlation coefficient. Different from a steady-flow spectrum, which decreases with a gentle slope as the frequency increases, they show a selectivity of frequency n , and selective frequencies of the two spectra are complementary to each other. Thus at the instance of generation, the turbulence which consists of selective components of frequency changes to the complementary constitution.

5.3.4 Propagation of generated turbulence

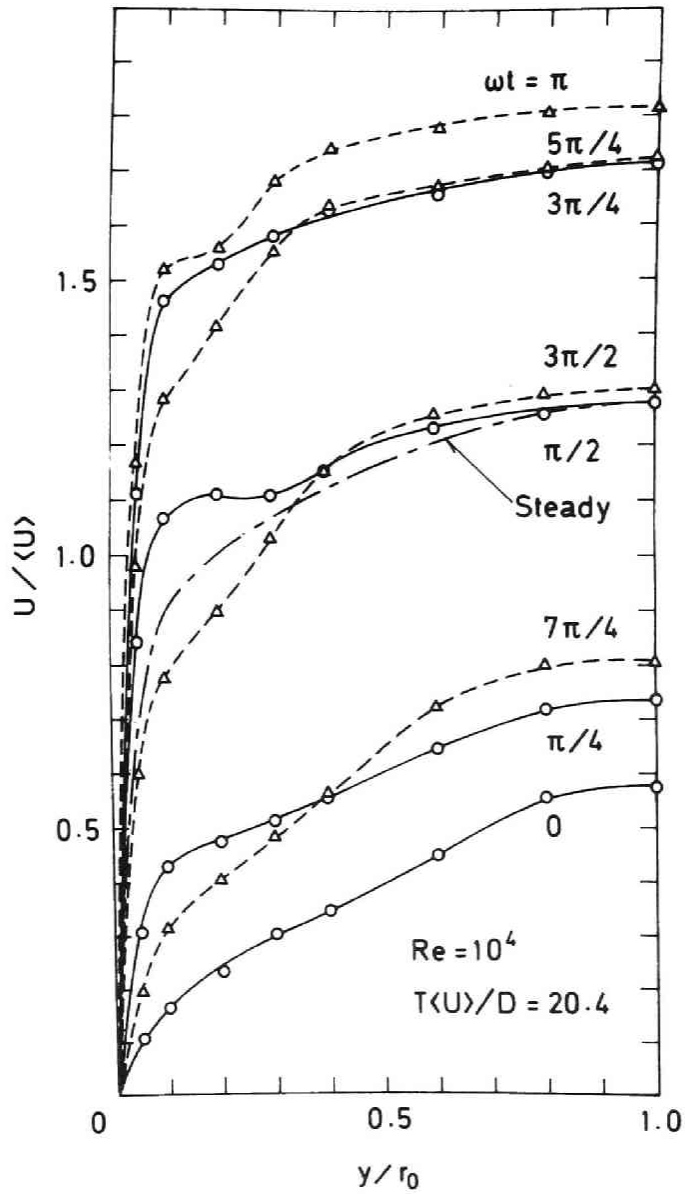


Fig. 5.6. Velocity profiles in pulsating flow.

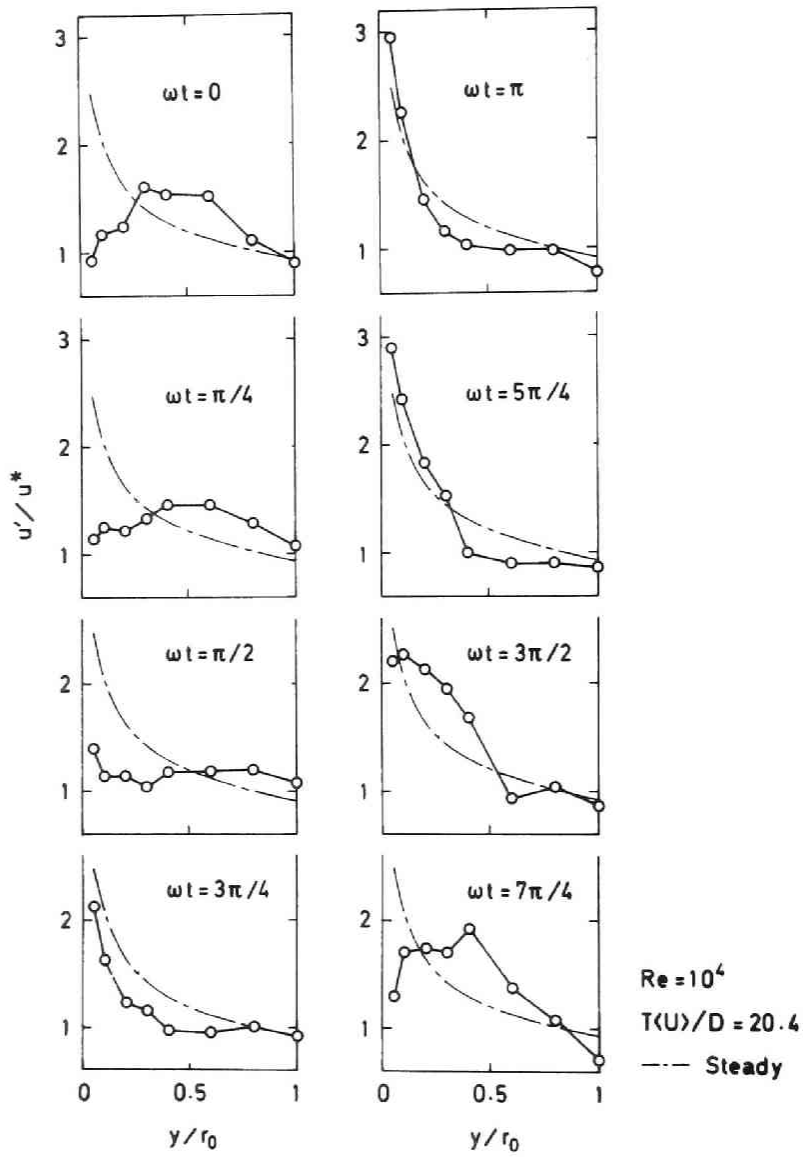


Fig. 5.7. Turbulence intensity profiles in pulsating flow.

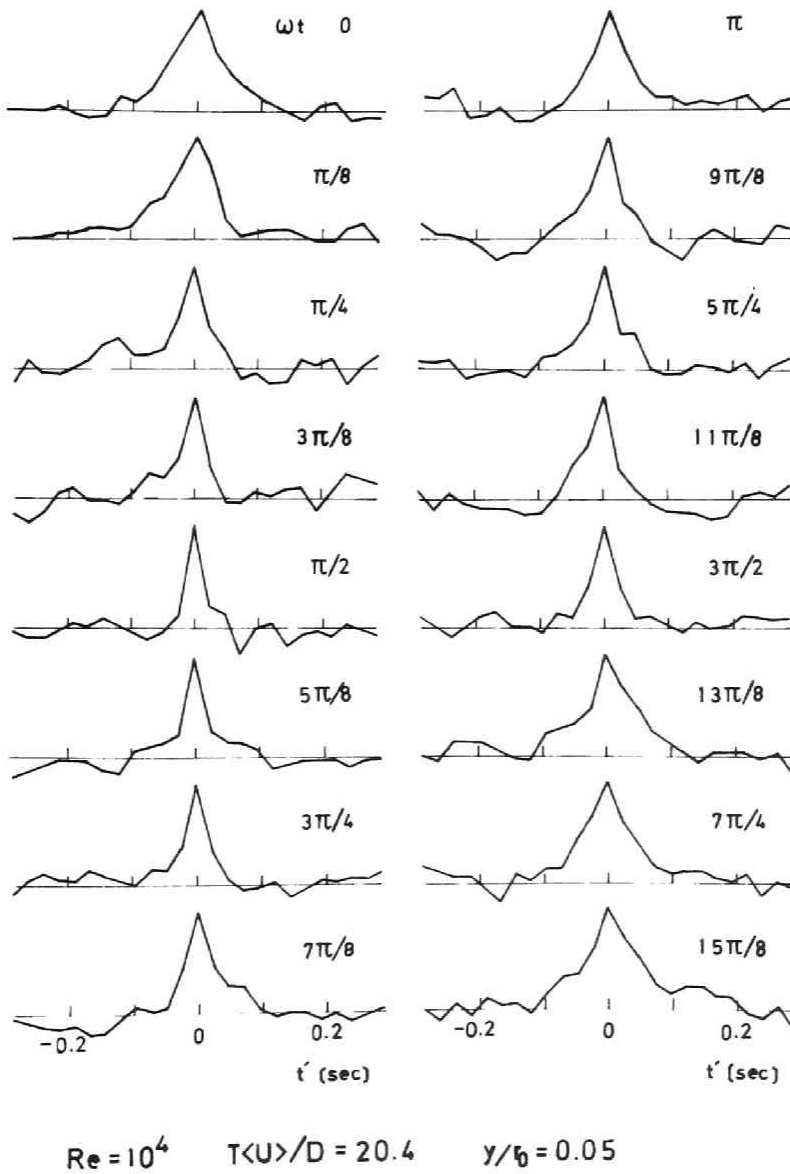


Fig. 5.8. Autocorrelation coefficients in pulsating flow.

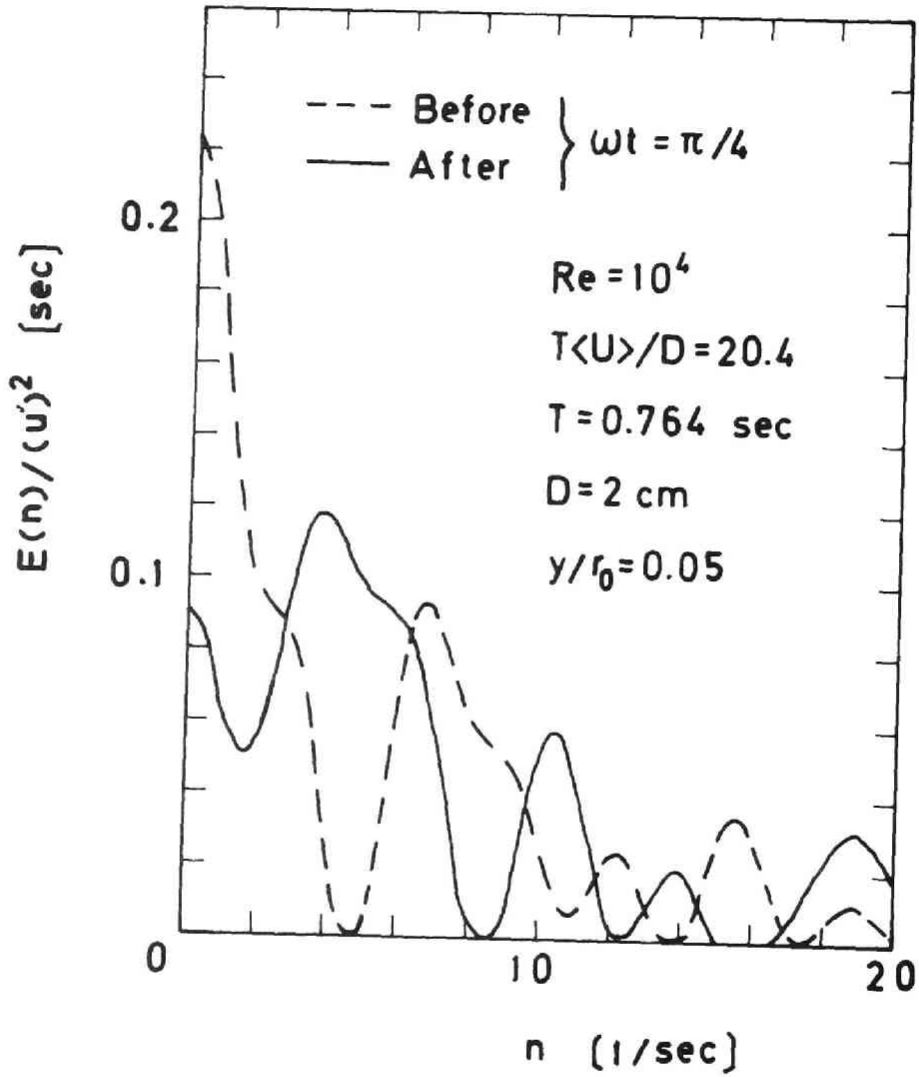


Fig. 5.9. One-dimensional energy spectra just before and after phase angle $\pi/4$.

Next, propagation process of the generated turbulence will be studied. The asymmetrical correlation curve, which represents a rapid change of scale, was also found at $y^+ \geq 15.7$. Figure 5. 10 shows the most asymmetrical correlation curves at different radial points. It occurs at the later phase but less conspicuously with increasing radial distance from the wall; the difference of phase is indicated in the same figure as the time period $\overline{\Delta t}$.

Figure 5. 11 shows a variation of intensity of turbulence from the instance of the rapid change of scale at each radial point. Although maximum value decreases as the distance from the wall increases, a similar variation appears throughout the cross-section of the tube and the phase difference of the maximum intensity is nearly equal to that of the rapid change of scale.

From the above results, it is clear that decreasing its coherency the generated turbulence propagates to the centreline of the tube.

Figure 5. 12 shows the change of medium frequency during the propagation. It becomes high at $y/r_0 = 0.1$ and then decreases lower slowly. So it can be said that the propagation process is not monotonously diffusive one but affected by some discrete events occurring in sequence.

In fact, the changes of the propagation time and the medium frequency indicate that the process is made up by three stages: (i) the generated turbulence propagates slowly to $y/r_0 \simeq 0.1$ or $y^+ \simeq 31.4$; (ii) it changes to high frequency and propagates quickly to $y/r_0 \simeq 0.3$ or $y^+ \simeq 94.3$ and then, (iii) becoming lower

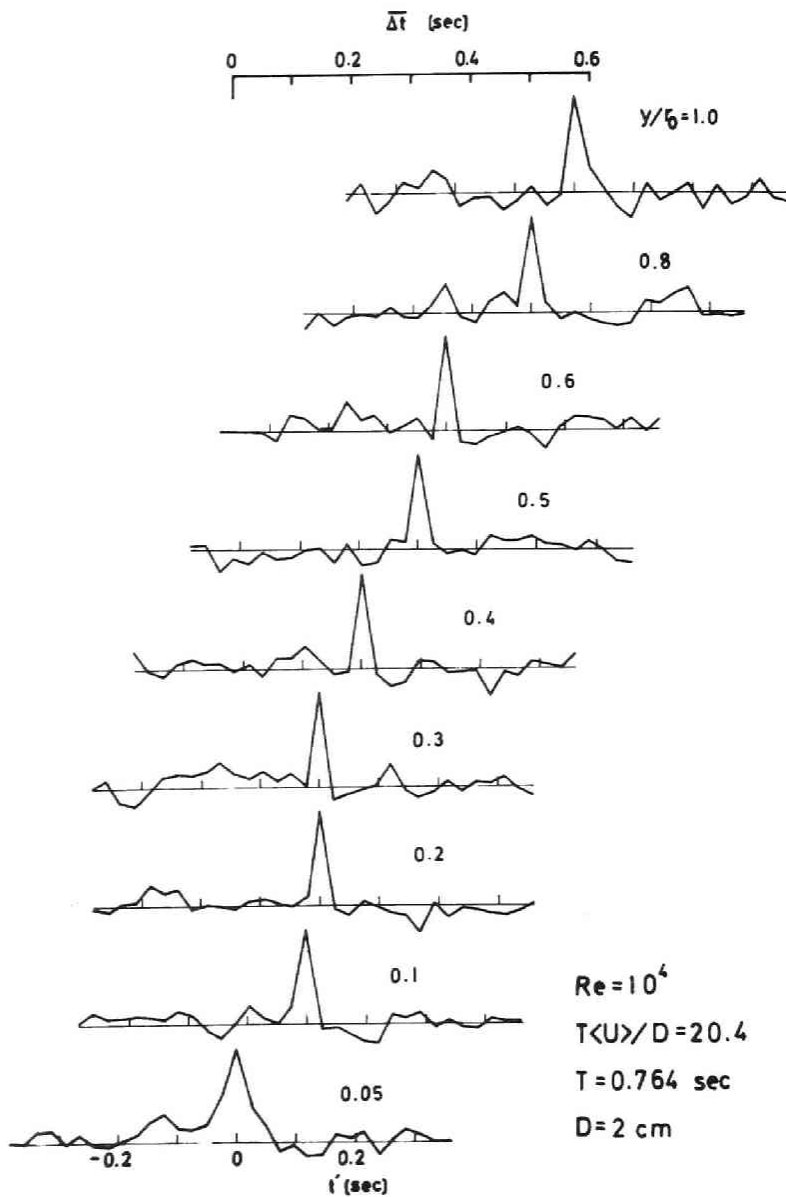


Fig. 5.10. Radial distribution of asymmetrical autocorrelation coefficients.

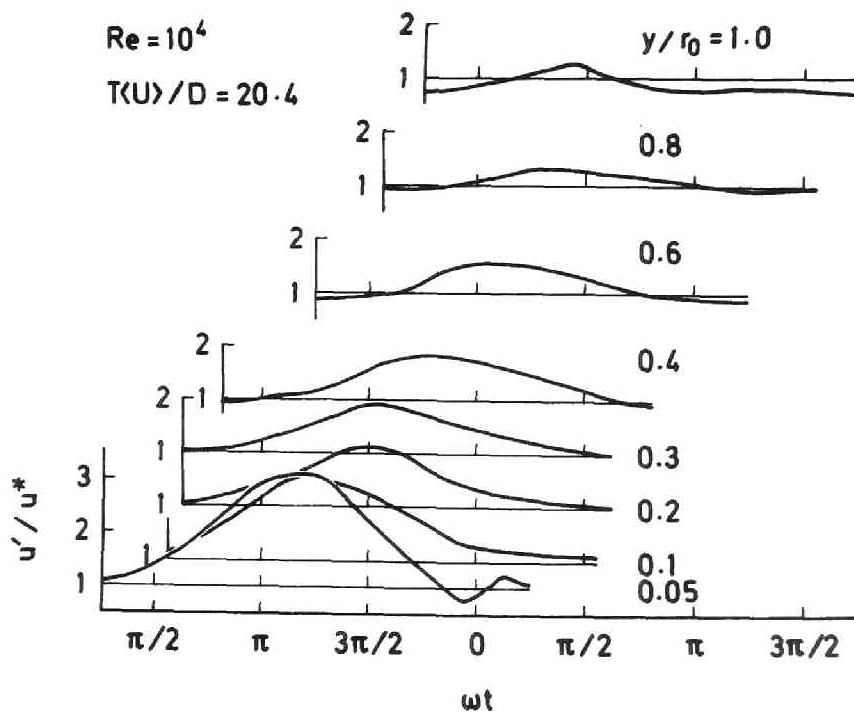


Fig. 5.11. Variations of turbulence intensity after rapid change of time scale.

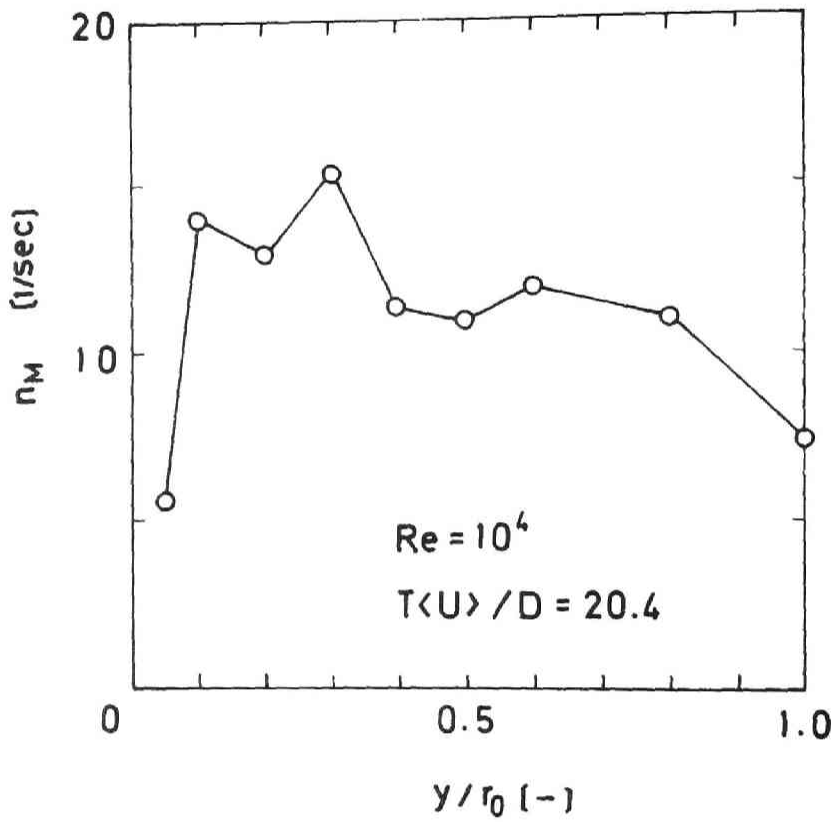


Fig. 5.12. Medium frequency of propagating turbulence.

frequency slowly, it propagates to $y/r_0 = 1.0$. It is apparent that the 'appearance of a relatively low speed region of fluid' occurs in the first stage and the 'lift-up' in the second stage. However, the 'oscillatory growth' and the 'breakup' do not appear in the propagation process. The variation of intensity of turbulence suggests that the breakup subsequent to the oscillatory growth occurs near the wall at $t \simeq 0.35$ sec, when the generated turbulence propagates to $y/r_0 \simeq 0.6$ or $y^+ \simeq 188$. Thus it is clear that the turbulence which propagates is not the one associated with the lifted-up fluid which shows the oscillatory growth and the breakup of turbulence in the wall region ($0 < y^+ < 70$); the propagation is considered to be associated with the large-scale vortex which was observed by Nychas *et al.* [14] and Offen and Kline [15].

5.3.5 Mean propagation time $\overline{\Delta t}$

The radial distributions of mean propagation time for four pulsation periods are shown in Fig. 5. 13. As can be seen, they are independent of pulsation period; that is, they are not affected by the change of axial velocity.

Moreover, it is worth noting that the value of mean propagation time at the centreline of the tube is nearly equal to the mean burst period (0.53 sec at $Re = 10^4$). This was confirmed at other Reynolds numbers. Figure 5. 14 shows the mean propagation time elapsed from the generation instance at $y^+ = 15.7$. They decrease rapidly with increasing Reynolds number, and each value at $y/r_0 = 1$ agrees well with the mean burst period. Accordingly,

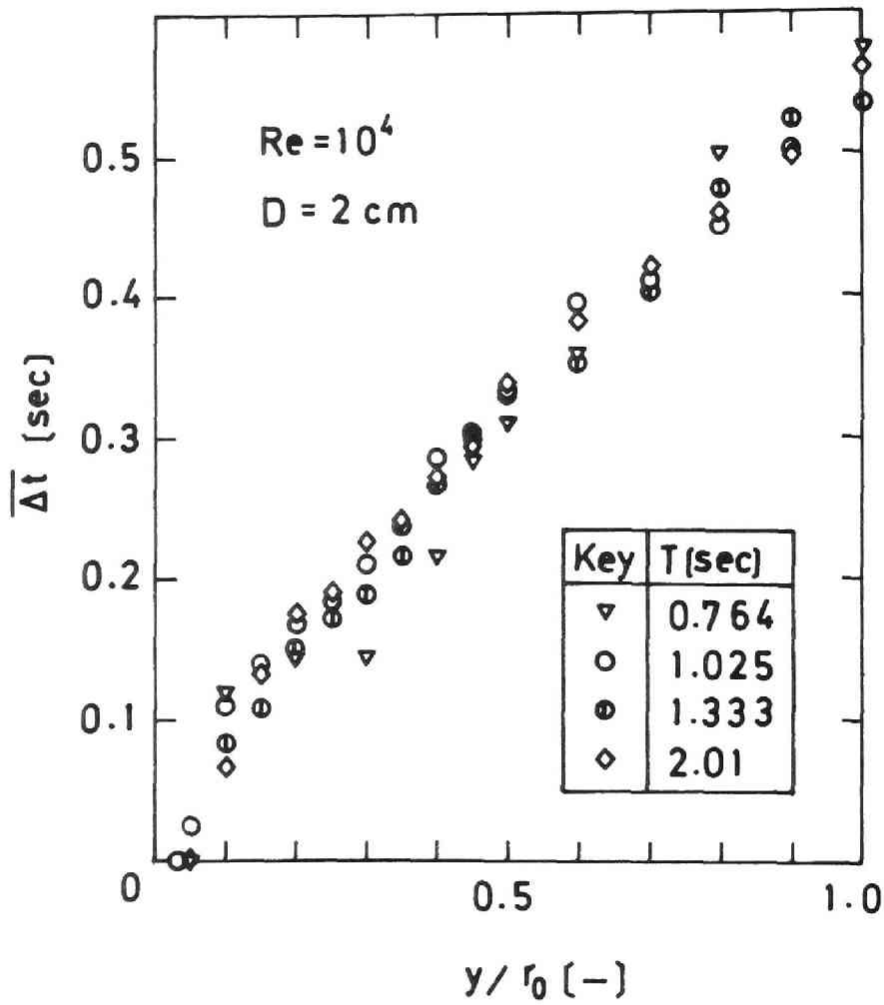


Fig. 5.13. Mean propagation time as a function of y/r_0 and T .

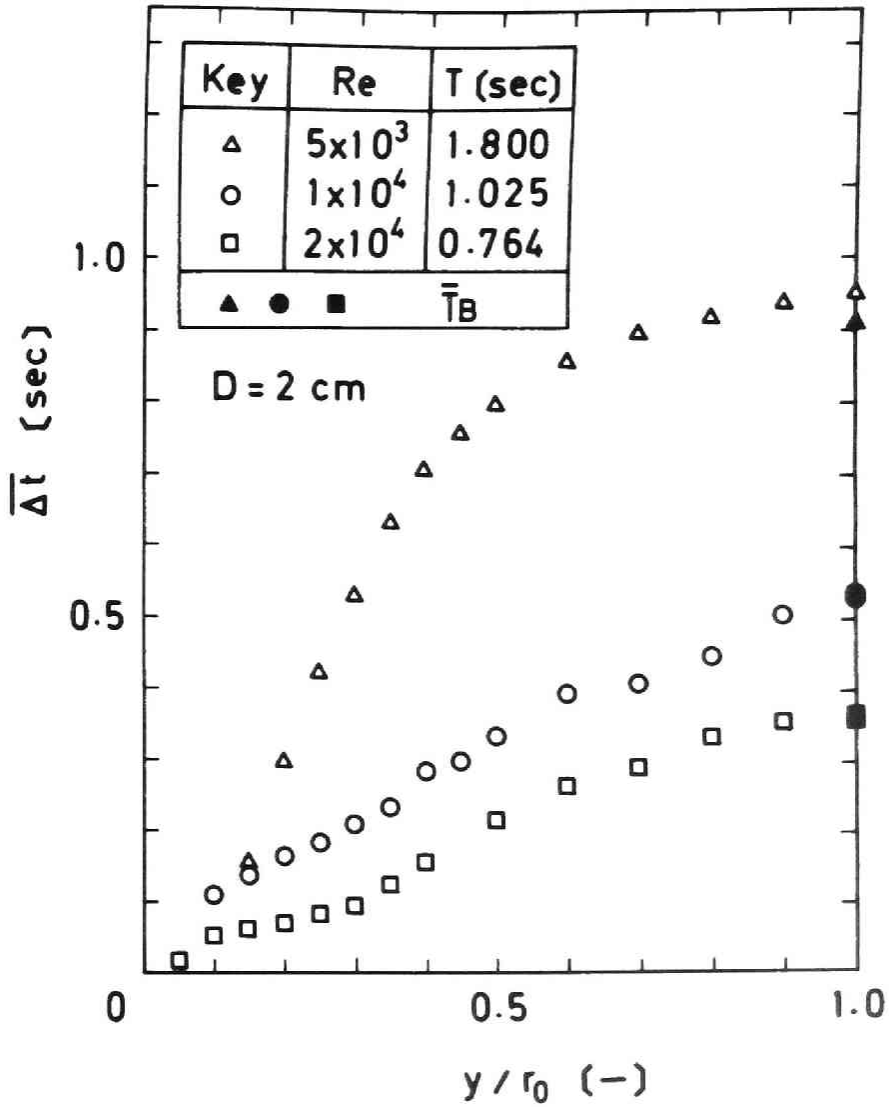


Fig. 5.14. Mean propagation time as a function of y/r_0 and Reynolds number.

if the pulsation period is shorter than the mean burst period, the propagation does not reach the centreline of the tube during one pulsation period, and so the periodical change of intensity of turbulence is presumed to appear only in the limited region near the wall, as mentioned in Section 5.3.2.

Further the facts that the mean propagation time is not affected by the pulsation and that its value at the centreline of the tube is equal to the mean burst period strongly suggest that the propagation process is consistent not only in pulsating flow but also in steady flow.

5.3.6 Mean burst period

Figure 5. 15 shows the mean propagation time normalized by the wall parameters ν and u^* as a function of y^+ . As can be seen, there is an excellent correlation of results for all Reynolds numbers, i.e., a law of the wall is applicable to the propagation time, and the values of $\overline{\Delta t}^+$ are in good agreement with those of $\overline{T_B}^+$ which are plotted against dimensionless radius R^+ .

Accordingly, it can be said that the entire cycle of bursting is characterized by the propagation process and that the bulk parameter dependency of mean burst period is attributed to the propagation distance, which is nearly equal to pipe radius.

Further, the explanation of the periodicity of bursting will be completed, if the last stage of propagation is linked to the first stage or generation of turbulence. To this end, as already mentioned, the rapid change of the selective frequencies to the comple-

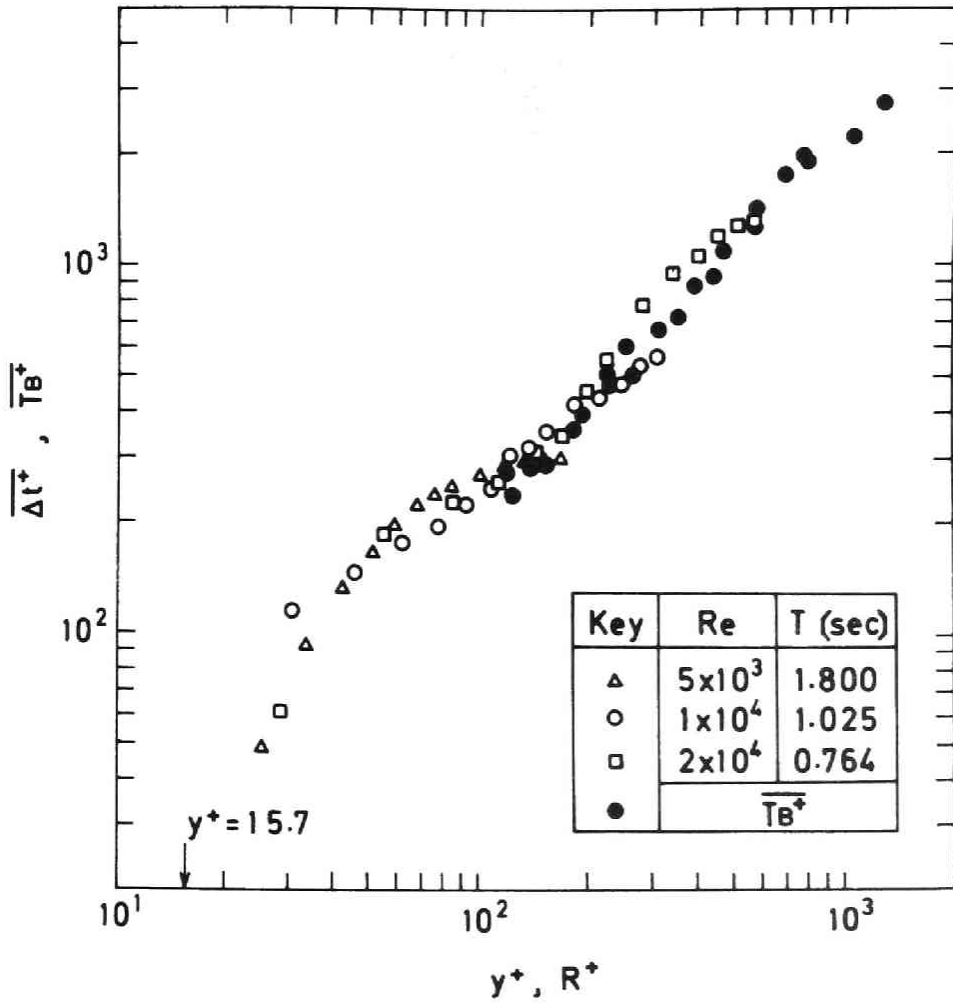


Fig. 5.15. $\overline{\Delta t}$ and $\overline{T_B}$ normalized with wall parameters as functions of y^+ and R^+ .

mentary values at the instance of generation is considered to be one of useful clues. At the same time, however, it must be noted that there may be clear difference between the generation of turbulence in steady flow and that in resonant pulsating flow where the generation is ruled directly by the pulsating velocity.

5.4 Conclusion

1. In the preferred range of burst period, the turbulence is generated near the wall by the flow pulsation and at the instance of generation, the frequencies of turbulence become selective and change to the complementary values.
2. Decreasing its coherency, the generated turbulence propagates radially to the centreline of the tube. The mean propagation time is independent of the pulsation period and scales on the wall parameters.
3. The mean propagation time in which the turbulence propagates from its origin to the centreline of the tube agrees well with the mean burst period of steady turbulent flow. This fact strongly suggests that the entire cycle of bursting is characterized by the propagation of generated turbulence to the radial direction and that the bulk parameter dependency of mean burst period is attributed to the pipe radius.
4. Due to this constant time of propagation, the periodical change of intensity of turbulence becomes to be localized within near the wall with decreasing pulsation period in the region $T_{B_{\min}} < T < \overline{T}_B$.

CHAPTER 6

CONCLUSION

6.1 Frequency Response of Momentum, Heat and Mass Transfer

The dynamic behaviours of flow rate, wall shear stress and heat transfer coefficient were expressed by the frequency response curves over the wide range of frequency.

For momentum transfer in pulsating laminar flow, measurements are well correlated with Sexl's analysis. For flow rate and wall shear stress in pulsating turbulent flow, the amplitude attenuation and phase shift decrease as Reynolds number increases because of the unsteady-state Reynolds stress. This contribution of Reynolds stress to frequency response is estimated by the eddy viscosity model similar to that for steady turbulent flow.

For heat or mass transfer in pulsating laminar flow, the similarity relation between X and Y does not exist but it can be used as a first approximation for the frequency response.

6.2 Resonance Phenomena in Pulsating Flow

Two resonance phenomena were clarified. They are very important for understanding dynamic mechanism of the transport phenomena in pulsating flow.

For heat or mass transfer, the resonance results

from the history of fluid from the inlet section of transfer and the resonance point appears in the frequency response curve of local value. The resonance point in the entrance region of transfer scales with $SnPrX^{2/3}$, and so the characteristic velocity of the resonance is determined by the thermal condition of steady flow.

The resonance in pulsating turbulent flow is related to the periodicity of bursting; when the pulsation period is within the preferred range of burst period of steady flow, the bursting of the same period as the pulsation period dominates, so the turbulent fluctuation pulsates in a manner similar to the bursting in steady flow, while mean burst period does not change, if the pulsation period is longer than the maximum value of burst period.

6.3 Dynamic Process of Bursting

From the measurement in resonant pulsating flow, one clue for the clarification of periodicity of bursting was given.

The resonance in pulsating flow affects only the generation of turbulence. Another important factor, which characterizes the dynamic behaviour of turbulence in pulsating flow, is the coherency of the propagation of generated turbulence: changing its frequency, the generated turbulence propagates to the centreline of the tube with the unique propagation time, which scales on the wall parameters, and the propagation time in which the turbulence propagates from the position of origin to the centreline agrees well with the mean burst period. This fact strongly suggests that the entire cycle of bursting

is characterized by the propagation of generated turbulence to the radial direction and that the bulk parameter dependency of burst period is attributed to the pipe radius.

6.4 Recommendation of Future Work

An important avenue for continuing research would seem to be more detailed investigation of bursting process in resonant pulsating flow. For example, the variation of spatial correlation coefficient in the transverse direction will give many additional informations to the generation and propagation of turbulence, and so the implication of the spatial coherence of structure in the sublayer of steady flow will be interpreted properly.

NOMENCLATURE

a_p	= amplitude of pressure drop	[-]
a_τ	= amplitude of wall shear stress	[-]
C	= constant in Eq.(3.9)	[-]
C_p	= Heat capacity at constant pressure	[cal/g·°C]
D	= pipe diameter	[cm]
D	= molecular diffusivity	[cm ² /sec]
$E(n)$	= one-dimensional energy spectrum	[cm ² /sec]
F	= dimensionless temperature, Eqs.(3.7)-(3.9)	[-]
\bar{F}	= average of dimensionless temperature, given by Eq.(3.15)	[-]
f	= friction factor	[-]
h	= heat transfer coefficient	[cal/cm ² ·sec·°C]
I	= electric current	[A]
$Im(Z)$	= imaginary part of complex quantity Z	[-]
k	= mass transfer coefficient	[cm/sec]
$\langle k \rangle$	= space-averaged mass-transfer coefficient	[cm/sec]
L	= dimensionless length ($=\ell/D Re Pr,$ $\ell/D Re Sc$)	[-]
ℓ	= length of transfer section	[cm]
ℓ_m	= mixing length	[cm]
M	= number of data per cycle evaluated for each value of $u'(t)$	[-]
N	= number of cycles evaluated for each value of $U(t)$ and $u'(t)$	[-]
$N(T_B)$	= Number of occurrence of bursting at burst period T_B	[-]
Nu	= Nusselt number ($=Dh/\lambda$)	[-]
n	= Frequency	[1/sec]

n_M	= medium frequency	[1/sec]
P	= static pressure	[g/cm \cdot sec 2]
Pr	= Prandtl number (= $C_p \mu / \lambda$)	[-]
R	= dimensionless radial distance (r/r_0)	[-]
R^+	= dimensionless radius ($= r_0 u^* / \nu$)	[-]
Re	= Reynolds number ($= D \langle U \rangle_s / \nu$)	[-]
$Re(Z)$	= Real part of complex quantity Z	[-]
$R_{uu}(T)$	= maximum of time delayed autocorrelation coefficient	[-]
$R_{uu}(t')$	= autocorrelation function	[-]
$R_{uu}(t, t')$	= phase-averaged autocorrelation function, Eqs. (5.2) and (5.3)	[-]
r	= radial distance from tube axis	[cm]
r_0	= radius of circular tube	[cm]
Sc	= Schmidt number ($= \nu / D$)	[-]
Sh	= Sherwood number ($= D k / D$)	[-]
$\langle Sh \rangle$	= Sherwood number averaged over the transfer section ($= D \langle k \rangle / D$)	[-]
Sn	= Stokes number ($= r_0^2 \omega / \nu$)	[-]
T	= period of pulsation	[sec]
T_B	= burst period	[sec]
$\overline{T_B}$	= mean value of T_B	[sec]
$\overline{T_B}^+$	= dimensionless period ($= \overline{T_B} (u^*)^2 / \nu$)	[-]
$T_{B_{min}}$	= minimum value of T_B	[sec]
T_c	= critical period of pulsation	[sec]
T_q	= approximate upper limit of period for the region of Profiles I	[sec]
t	= time	[sec]
t'	= delay time	[sec]
Δt	= time interval of propagation of generated turbulence	[sec]
$\overline{\Delta t}$	= mean value of Δt	[sec]

$\overline{\Delta t^*}$	= dimensionless time ($=\overline{\Delta t}(u^*)^2/\nu$)	[-]
U	= local velocity in axial direction	[cm/sec]
$\langle U \rangle$	= velocity obtained by averaging the value U over the cross-section	[cm/sec]
U_i	= instantaneous value of U	[cm/sec]
U	= dimensionless velocity ($=-2U_p\nu/a_p r_0^2$)	[-]
u	= fluctuating component of velocity in axial direction	[cm/sec]
u'	= root-mean square of u	[cm/sec]
u^*	= friction velocity in steady flow ($=\sqrt{\tau_w/\rho}$)	[cm/sec]
v	= fluctuating component of velocity in radial direction	[cm/sec]
X	= dimensionless distance ($=x/D \text{ Re Pr, } x/D \text{ Re Sc}$)	[-]
x	= distance in axial direction	[cm]
Y	= dimensionless distance ($=y/r_0$)	[-]
y	= normal distance from wall	[cm]
y^+	= dimensionless distance ($=y u^*/\nu$)	[-]
Z	= transfer function, Eq.(3.19)	[-]

<Greek letters>

α	= experimental constant	[-]
β	= experimental constant	[-]
Γ	= dimensionless temperature	[-]
Γ'	= temperature	[°C]
Γ_b'	= temperature of bulk fluid	[°C]
Γ_w'	= temperature at wall	[°C]
$\Gamma(x)$	= gamma function of x	[-]
ϵ, ϵ_M	= eddy viscosity	[cm ² /sec]

ϵ_c	= eddy viscosity for core region	[cm ² /sec]
η	= similarity variable, Eq.(3.6)	[-]
θ	= dimensionless time ($=\lambda t/c_p \rho r_0^2$)	[-]
λ	= thermal conductivity	[cal/cm·sec·°C]
μ	= viscosity	[g/cm·sec]
ν	= kinematic viscosity	[cm ² /sec]
ρ	= density	[g/cm ³]
τ	= shear stress	[g/cm·sec ²]
τ_w	= shear stress at wall in steady flow	[g/cm·sec ²]
ω	= angular frequency	[1/sec]

<Subscripts>

p	= pulsating component
s	= steady component

REFERENCES

- [1] Alabastro, E. B. F. and J. D. Hellums: *A. I. Ch. E. Journal*, 15, 164 (1969)
- [2] Bird, R. B.: *Chemie-Ing. Techn.*, 31, 569 (1959)
- [3] Corino, E. R. and R. S. Brodkey: *J. Fluid Mech.*, 37, 1 (1969)
- [4] Fortuna, G. and T. J. Hanratty: *Int. J. Heat Mass Transfer*, 14, 1499 (1971)
- [5] Gerrard, J. H.: *J. Fluid Mech.*, 46, 43 (1971)
- [6] Hinze, J. O. "Turbulence", McGraw-Hill, New York (1959)
- [7] Karman, T. von: *Trans. ASME*, 61, 705 (1939)
- [8] Kim, H. T., S. J. Kline and W. C. Reynolds: *J. Fluid Mech.*, 50, 133 (1971)
- [9] Lebouche, M.: *C. R. Acad. Sc. Paris*, Ser. A-B 271, 9, A438 (1970)
- [10] Lèvêque, M. A.: *Ann. mines*, (ser. 12) 13, 201, 305, 381 (1928)
- [11] Lighthill, M. J.: *Proc. Roy. Soc. (London)*, Ser A, 224, 1 (1954)
- [12] Mizushima, T.: "Advances in Heat Transfer" Vol. 7, Edt. by F. Irvine and J. Hartnett, Academic Press, New York (1971)
- [13] Mochizuki, S. and K. Hatta: *Aeronautical Research Institute University of Tokyo Reports*, 6, 928 (1970)
- [14] Nychas, S. G., H. C. Hershey and R. S. Brodkey: *J. Fluid Mech.*, 61, 513 (1973)
- [15] Offen, G. R. and S. J. Kline: *J. Fluid Mech.*, 62, 223 (1974)
- [16] Pennell, W. T., E. M. Sparrow and E. R. G. Eckert:

- Int. J. Heat Mass Transfer*, 15, 1067
(1972)
- [17] Rao, K. N., R. Narasimha and M. A. Badri
Narayanan: *J. Fluid Mech.*, 48, 339 (1971)
- [18] Schultz-Grunov, F.: *Forsch. Gebiete Ing.-Wes.*,
11, 170 (1940)
- [19] Sexl, T: *Z. Phys.*, 61, 349 (1930)
- [20] Shiotsuka, T., N. Honda and Y. Shima: *Kagaku
Kogaku (Chem. Eng., Japan)*, 21, 638 (1957)
- [21] Siegel, R. and M. Perlmutter: *Trans. ASME*,
Ser. C. 84, 111 (1962)
- [22] Stermole, F. J. and M. A. Larson: *Ind. Eng. Chem.,
Fund.*, 2, 62 (1963)
- [23] Uchida, S.: *ZAMP* 7, 403 (1956)
- [24] West, F. B. and A. T. Taylor : *C. E. P.*, 48, 39
(1952)

ACKNOWLEDGEMENT

The author would like to express his appreciation to all present and former members of Laboratory of Transport Phenomena, Department of Chemical Engineering, Kyoto University, who have helped him in one way or another in the preparation; in particular to Professor Tokuro Mizushina, who provided him many helpful suggestions and criticisms throughout this study; to Lecturer Hiromasa Ueda, who gave him many valuable advices on the experimental techniques; to Messrs Rokuro Mishina, Koji Okane, Susumu Ide, Yoshihisa Mizukami, Yasumi Shiozaki and Hideo Hirasawa, who assisted him in conducting the experiments; and to Miss Kumiko Yoshinari, who, by patient and skilful typing, transformed an almost illegible manuscript into a very clear typescript.

